Supplementary Information

The Synthesis and Characterization of, and Dynamic Processes Occurring in Pd(II) Chelate Complexes of 2-pyridyldiphenylphosphine

Jianke Liu, Chacko Jacob, Kelly J. Sheridan, Firas Al-Mosule, Brian T. Heaton, Jonathan A. Iggo, Mark Matthews, Jeremie Pelletier, Robin Whyman, Jamie F. Bickley, and Alexander Steiner.*

Department of Chemistry, Donnan and Robert Robinson Laboratories, University of
Liverpool, P. O. Box. 147, Liverpool, U. K. L69 7ZD.

AUTHOR EMAIL ADDRESS iggo@liv.ac.uk

Contents

Supplementary Figure 1. The $^{31}P\{^1H\}$ NMR spectrum recorded at 293 K of isolated product from the reaction of $[Pd(PhCN)_2Cl_2]$ with 1 equivalent of Ph_2Ppy in CH_2Cl_2.

Supplementary Figure 2. (a) $^{31}P\{^1H\}$ NMR spectrum of **3**[X], (X = Cl, BF_4, OTf, $MeSO_3$) in CH_2Cl_2 /MeOH recorded at 233 K (top)and **3**(Cl) at 293 K (bottom).

(b) ^1H NMR spectra of **3**[X], (X = Cl, BF_4, OTf, $MeSO_3$)in CH_2Cl_2/MeOH recorded at 233 K.

Supplementary Figure 3. Aromatic region of the ^1H NMR spectra of **4**[OTf] in CD_2Cl_2 recorded at 233 K (top) and 293 K (bottom).

Supplementary Figure 4. $^{31}P\{^1H\}$ NMR spectrum of "$[Pd(\kappa^2\text{-}Ph_2Ppy)(\kappa^1\text{-}Ph_2Ppy)(CH_3CN)](BF_4)_2$" (**5**) in CH_2Cl_2:CH_3CN (20:1) solution recorded at 193 K.

Supplementary Figure 5. (a) $^{31}P\{^1H\}$ NMR spectrum of **8**[X], (X = OTf, CF_3CO_2, $MeSO_3$) in CH_2Cl_2 recorded at 193 K.

(b) Aromatic region of the ^1H NMR spectra of **8**[X], (X = OTf, CF_3CO_2, $MeSO_3$) in CH_2Cl_2 recorded at 193 K.

Supplementary Figure 6. (a) $^{31}P\{^1H\}$ NMR spectrum of **8′[**X], (X = OTf, $MeSO_3$, BF_4) in CH_2Cl_2 recorded at 193 K.

(b) Aromatic region of the ^{1}H NMR spectra of **8**$'$[X], (X = OTf, $MeSO_3$, BF_4) in CH_2Cl_2 recorded at 193 K.

Supplementary Figure 7. $^{31}P\{^1H\}$ NMR spectrum of [Pd(κ^2-Ph_2Ppy)(κ^1-Ph_2PpyH)($MeSO_3$)][$MeSO_3$]$_2$ recorded at 183 K in CH_2Cl_2 in the presence of excess $MeSO_3H$. The sharp resonance at ca. δ(P) = -10 ppm is due to [Ph_2Ppy][$MeSO_3$].

Supplementary Figure 8. (a) The ^{15}N and (b) $^{15}N\{^1H\}$ NMR spectra of Ph_2Ppy recorded at 293K in CH_2Cl_2; (c) the ^{15}N and (d) $^{15}N\{^1H\}$ NMR spectra of [Ph_2PpyH][$MeSO_3$] recorded at 203K in CH_2Cl_2

VT NMR spectra, and simulations, Eyring and Arrhenius plots.

Supplementary Figure 9. Experimental and simulated variable temperature $^{31}P\{^1H\}$ NMR spectra of **10** in MeOH Pd:PPh_2py:CH_3SO_3H = 1:3.4:10. (sample 3)

Supplementary Figure 10. Eyring and Arrhenius plots for **10** in MeOH Pd:PPh_2py:CH_3SO_3H = 1:3.4:10. (sample 3)

Supplementary Figure 11. Experimental and simulated variable temperature $^{31}P\{^1H\}$ NMR spectra of **10** in MeOH Pd:PPh_2py:CH_3SO_3H = 1:3.4:25. (sample 4)

Supplementary Figure 12. Eyring and Arrhenius plots for **10** in MeOH Pd:PPh_2py:CH_3SO_3H = 1:3.4:25. (sample 4)

Supplementary Figure 13. Experimental and simulated variable temperature $^{31}P\{^1H\}$ NMR spectra **10** in MeOH Pd:PPh_2py:CH_3SO_3H = 1:3.2:15. (sample 5)

Supplementary Figure 14. Eyring and Arrhenius plots for **10** in MeOH Pd:PPh_2py:CH_3SO_3H = 1:3.2:15. (sample 5)

Supplementary Figure 15. Experimental and simulated variable temperature $^{31}P\{^1H\}$ NMR spectra of **10** in MeOH Pd:PPh_2py:CH_3SO_3H = 1:2.9:25. (sample 6)

Supplementary Figure 16. Eyring and Arrhenius plots for **10** in MeOH Pd:PPh_2py:CH_3SO_3H = 1:2.9:25. (sample 6)

Supplementary Figure 17. Experimental and simulated variable temperature $^{31}P\{^1H\}$ NMR spectra of **10** in MeOH:CD_2Cl_2 4:3; Pd:PPh_2py:CH_3SO_3H = 1:3.1:5. (sample 8)

Supplementary Figure 18. Eyring and Arrhenius plots for **10** in MeOH:CD_2Cl_2 4:3; Pd:PPh_2py:CH_3SO_3H = 1:3.1:5. (sample 8)

Supplementary Figure 19. Experimental and simulated variable temperature $^{31}P\{^1H\}$ NMR spectra of **10** in MeOH Pd:PPh_2py:CH_3SO_3H = 1:3.1:10. (sample 1)

Supplementary Figure 20. Eyring and Arrhenius plots for **10** in MeOH Pd:PPh_2py:CH_3SO_3H = 1:3.1:10. (sample 1)

Supplementary Figure 21. Experimental and simulated variable temperature $^{31}P\{^1H\}$ NMR spectra of **10** in MeOH Pd:PPh_2py:CH_3SO_3H = 1:3.1:10. (sample 2).

Supplementary Figure 22. Eyring and Arrhenius plots for **10** in MeOH Pd:PPh_2py:CH_3SO_3H = 1:3.1:10. (sample 2).

Supplementary Figure 23. Experimental and simulated variable temperature $^{31}P\{^1H\}$ NMR spectra of **10** in MeOH:CD_2Cl_2 (2:9) Pd:PPh_2py:CH_3SO_3H = 1:3.1:25. (sample 7)

Supplementary Figure 24. Eyring and Arrhenius plots for **10** in MeOH:CD_2Cl_2 (2:9) Pd:PPh_2py:CH_3SO_3H = 1:3.1:25. (sample 7)

Supplementary Figure 25. Experimental and simulated variable temperature $^{31}P\{^1H\}$ NMR spectra of **10** in CD_2Cl_2 Pd:PPh_2py:CH_3SO_3H = 1:2.9:2. (sample 9). Impurities included to aid simulation, but not optimized.

Supplementary Figure 26. Eyring and Arrhenius plots for **10** in CD_2Cl_2 Pd:PPh_2py:CH_3SO_3H = 1:2.9:2. (sample 9).

Supplementary Figure 27. Equilibrium saturation transfer difference measurements on impure **10**. The resonance of the chelating PPh_2py ligand at *ca.* δ(P) -48 was irradiated throughout the recovery delay (3 s). Top set sample of Supp Fig 13.- **10** in MeOH

Pd:PPh$_2$py:CH$_3$SO$_3$H = 1:3.2:15); bottom set sample of Supp. Fig 15.- Pd:PPh$_2$py:CH$_3$SO$_3$H = 1:2.9:10). (sample 2)

Significant saturation transfer is seen to the other PPh$_2$py ligands in **10** but not to those of other complexes.

Supplementary Figure 28. Experimental and simulated variable temperature $^{31}P\{^1H\}$ NMR spectra of **3**(Cl) in CD$_2$Cl$_2$ plus 0.1 mL MeOH. Note changes in ppm scale at 233, 253, 283 and 293 K.

Supplementary Figure 29. Experimental and simulated variable temperature $^{31}P\{^1H\}$ NMR spectra of **3**[OTf] in CD$_2$Cl$_2$ plus 0.1 mL MeOH. Note changes in ppm scale at 223, 263, and 283 K

Supplementary Figure 30. Experimental and simulated variable temperature $^{31}P\{^1H\}$ NMR spectra of **3**(Cl) in CD$_2$Cl$_2$:MeOH (1:1). Note changes in ppm scale at 243, and 273 K.

Supplementary Figure 31. Experimental and simulated variable temperature $^{31}P\{^1H\}$ NMR spectra of **3**[OTf] in CD$_2$Cl$_2$:MeOH (1:1).

Supplementary Figure 32. Variable temperature $^{31}P\{^1H\}$ NMR spectra of **4**(Cl) in CD$_2$Cl$_2$:MeOH (1:1).

Supplementary Figure 33. $^{31}P\{^1H\}$ NMR spectra of **4** in CD$_2$Cl$_2$:MeOH (1:1), Pd:P = 1:2.8 to 1:4.6 as chloride or triflate salts, T = 193 K.

Supplementary Figure 34. $^{31}P\{^1H\}$ NMR spectra of **4** in CD$_2$Cl$_2$:MeOH (1:1) , Pd:P = 1:2.8 to 1:4.6 as chloride or triflate salts, T = 213 K.

Supplementary Figure 35. $^{31}P\{^1H\}$ NMR spectra of **4** in CD_2Cl_2:MeOH (1:1) , Pd:P = 1:2.8 to 1:4.6 as chloride or triflate salts, T = 233 K.

Supplementary Figure 36. $^{31}P\{^1H\}$ NMR spectra of **4** in CD_2Cl_2:MeOH (1:1) , Pd:P = 1:2.8 to 1:4.6 as chloride or triflate salts, T = 243 K.

Supplementary Figure 37. $^{31}P\{^1H\}$ NMR spectra of **4** in CD_2Cl_2:MeOH (1:1) , Pd:P = 1:2.8 to 1:4.6 as chloride or triflate salts, T = 263 K.

Supplementary Figure 38. $^{31}P\{^1H\}$ NMR spectra of **4** in CD_2Cl_2:MeOH (1:1) , Pd:P = 1:2.8 to 1:4.6 as chloride or triflate salts, T = 273 K.

Supplementary Figure 39. $^{31}P\{^1H\}$ NMR spectra of **4** in CD_2Cl_2:MeOH (1:1) , Pd:P = 1:2.8 to 1:4.6 as chloride or triflate salts, T = 283 K.

Supplementary Figure 40. $^{31}P\{^1H\}$ NMR spectra of **4** in CD_2Cl_2:MeOH (1:1) , Pd:P = 1:2.8 to 1:4.6 as chloride or triflate salts, T = 293 K.

Supplementary Figure 41. Simulations of the variable temperature $^{31}P\{^1H\}$ NMR spectra of **4**(Cl) in CD_2Cl_2:MeOH (1:1), Pd:P = 1: 4.6, together with the Eyring and Arrhenius plots.

Supplementary Figure 42. Simulations of the variable temperature $^{31}P\{^1H\}$ NMR spectra of **4**(Cl)in CD_2Cl_2:MeOH (1:1), Pd:P = 1: 3.4, together with the Eyring and Arrhenius plots..

Supplementary Figure 43. Simulations of the variable temperature $^{31}P\{^1H\}$ NMR spectra of **4**(Cl)in CD_2Cl_2:MeOH (1:1), Pd:P = 1: 3.03, together with the Eyring and Arrhenius plots..

Supplementary Table 1 Kinetic and thermodynamic parameters for the dynamic processes in **4**(Cl)in CD_2Cl_2:MeOH (1:1).

X-ray crystal structures

Supplementary Table 2 Crystal data for **2b**.$2CH_2Cl_2$**,** **2b'**$[MeSO_3]_2.2CH_2Cl_2$, **3**BF_4, **4**.$2H_2O$ and **7**.CH_2Cl_2

Crystal Structure of *trans*-[Pd(κ^1-$Ph_2Ppy)_2Cl_2$] (2b)

Supplementary Figure 44. Molecular structure of *trans*-[Pd(κ^1-$Ph_2Ppy)_2Cl_2$] **2b** with key atoms labelled and H atoms removed for clarity

Supplementary Table 3 Selected bond lengths (Å) and angles (°) for *trans*-[Pd(κ^1-$Ph_2Ppy)_2Cl_2$] **2b**

Crystal structure of [Pd(κ^1-$Ph_2Ppy)_3Cl$](Cl) (4(Cl))

Supplementary Figure 45. Molecular structure of [Pd(κ^1-$Ph_2Ppy)_3Cl$](Cl) **(4**(Cl)**)** highlighting the CH...N (blue) and π-stacking interactions (red) between the phosphine ligands.

Supplementary Table 4 Selected bond lengths (Å) and angles (°) for [Pd(κ^1-$Ph_2Ppy)_3Cl$](Cl) **(4**(Cl)**)**

Supplementary Figure 1. The $^{31}P\{^1H\}$ NMR spectrum recorded at 293 K of isolated product from the reaction of $[Pd(PhCN)_2Cl_2]$ with 1 equivalent of Ph_2Ppy in CH_2Cl_2.

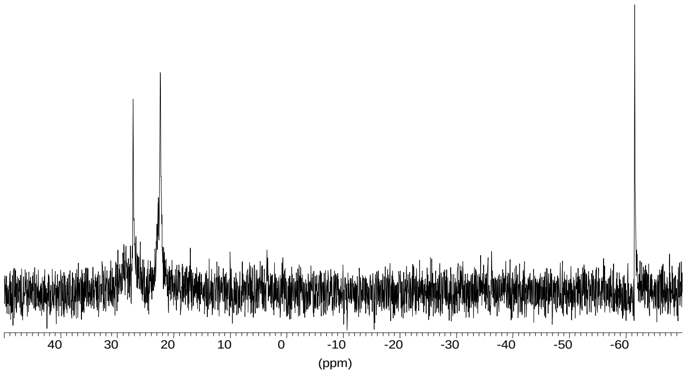

Supplementary Figure 2. **(a)** $^{31}P\{^{1}H\}$ NMR spectrum of **3**[X], (X = Cl, BF_4, OTf, $MeSO_3$) in CH_2Cl_2/MeOH recorded at (top) 233 K and **3**(Cl) at 293 K (bottom).

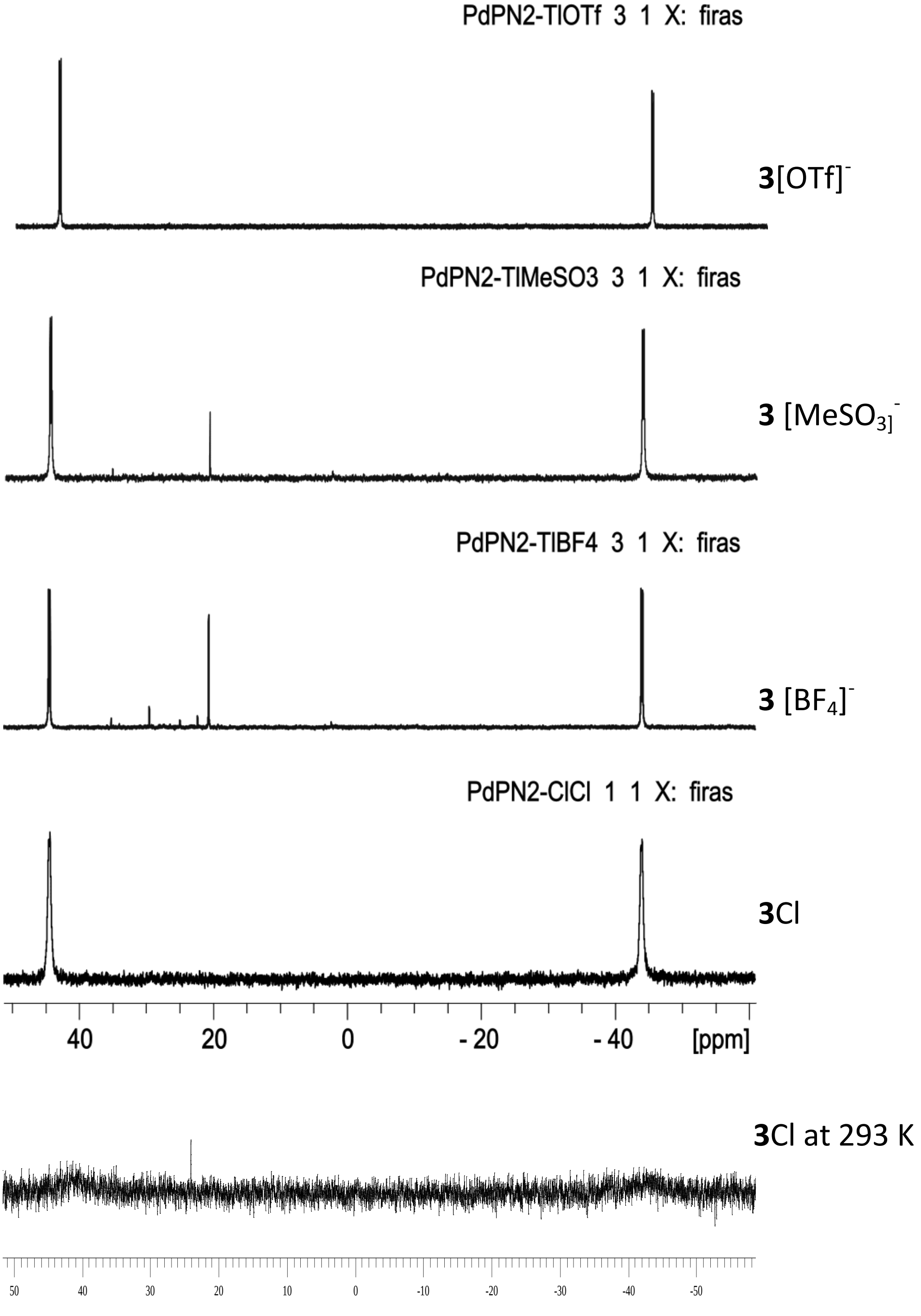

Supplementary Figure 2 Aromatic region of the ^{1}H NMR spectra of **3**(X), (X = Cl, BF_4, OTf, $MeSO_3$) in CH_2Cl_2/MeOH recorded at 233 K.

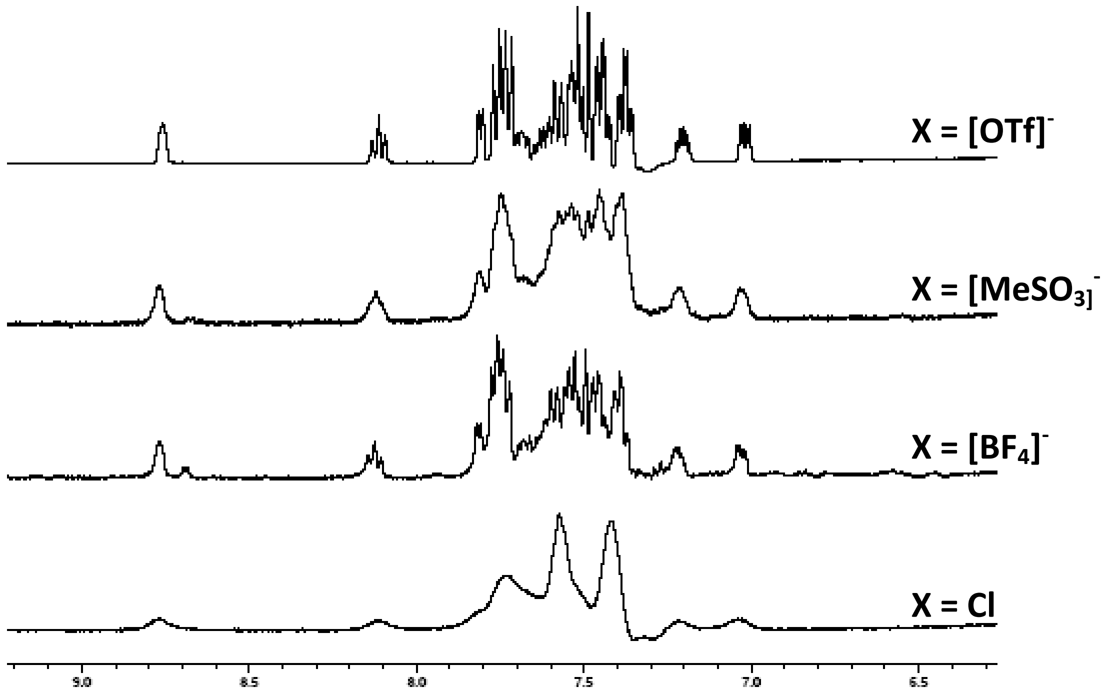

Supplementary Figure 3. Aromatic region of the ^{1}H NMR spectra of **4**[OTf] in CD_2Cl_2 recorded at 233 K (top) and 293 K (bottom).

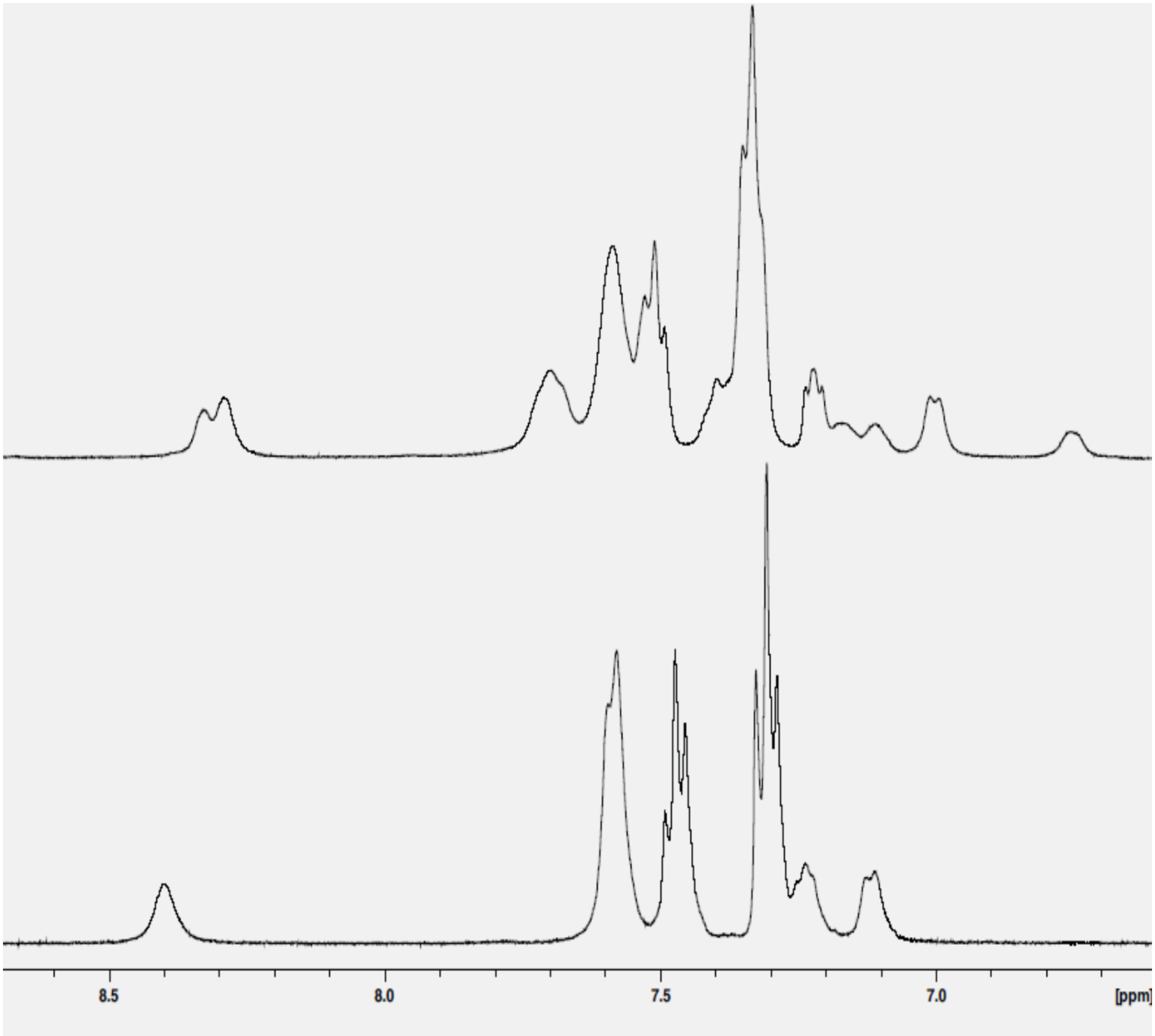

Supplementary Figure 4. $^{31}P\{^{1}H\}$ NMR spectrum of "[Pd(κ^2-Ph_2Ppy)(κ^1-Ph_2Ppy)(CH_3CN)](BF_4)$_2$" (**5**) in CH_2Cl_2:CH_3CN (20:1) solution recorded at 193 K.

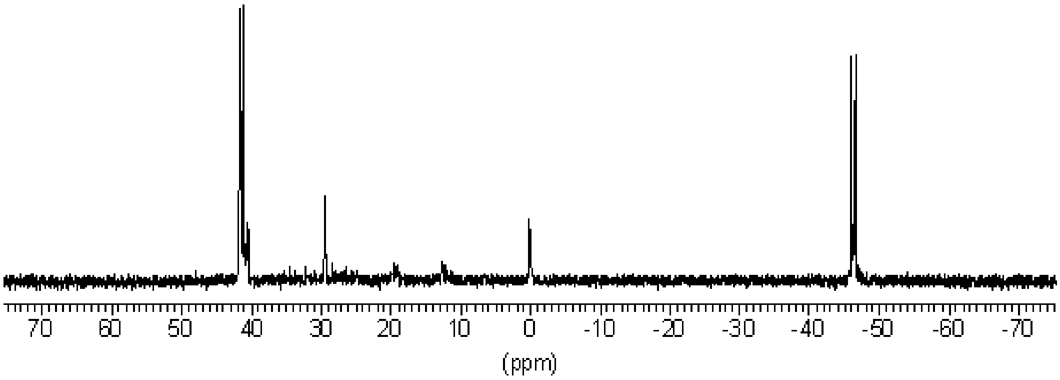

Supplementary Figure 5. **(a)** $^{31}P\{^1H\}$ NMR spectrum of **8**[X], (X = OTf, CF_3CO_2, $MeSO_3$) in CH_2Cl_2 recorded at 193 K.

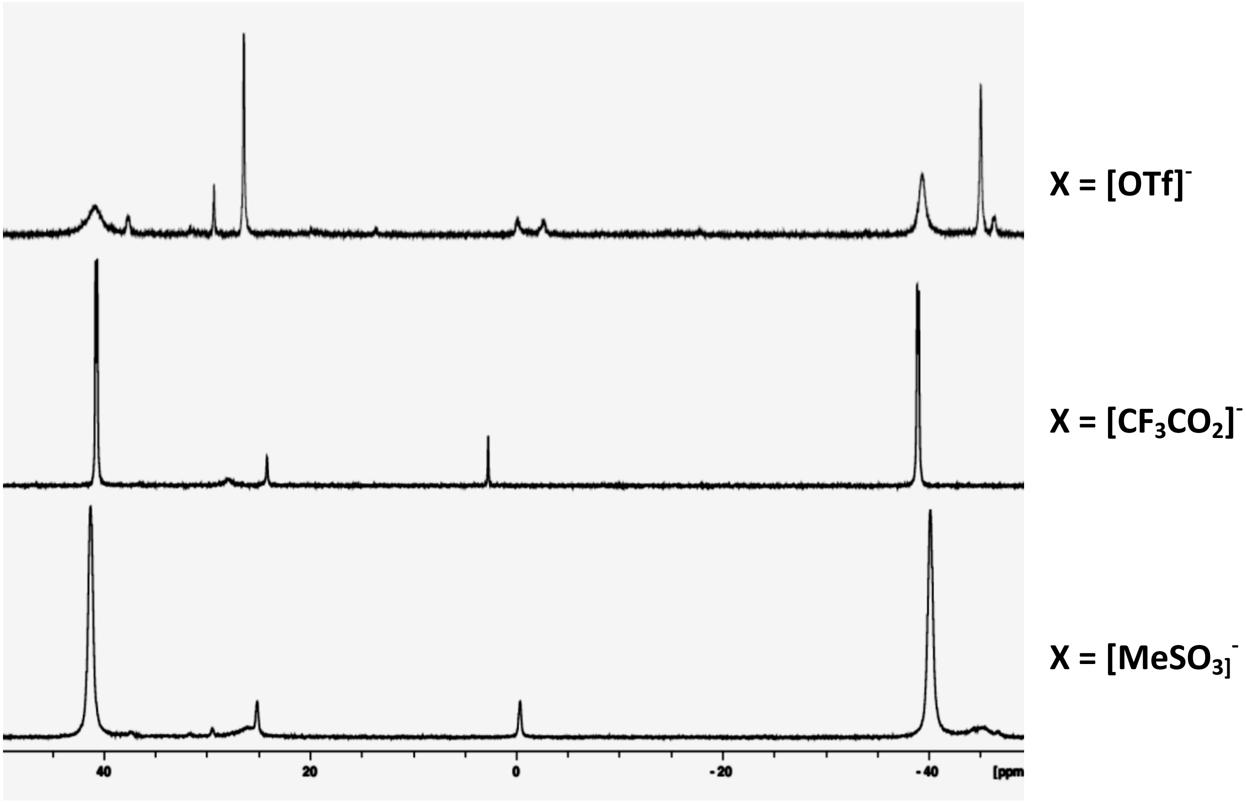

Supplementary Figure 5. **(b)** Aromatic region of the ^{1}H NMR spectra of **8**[X], (X = OTf, CF_3CO_2, $MeSO_3$) in CH_2Cl_2 recorded at 193 K.

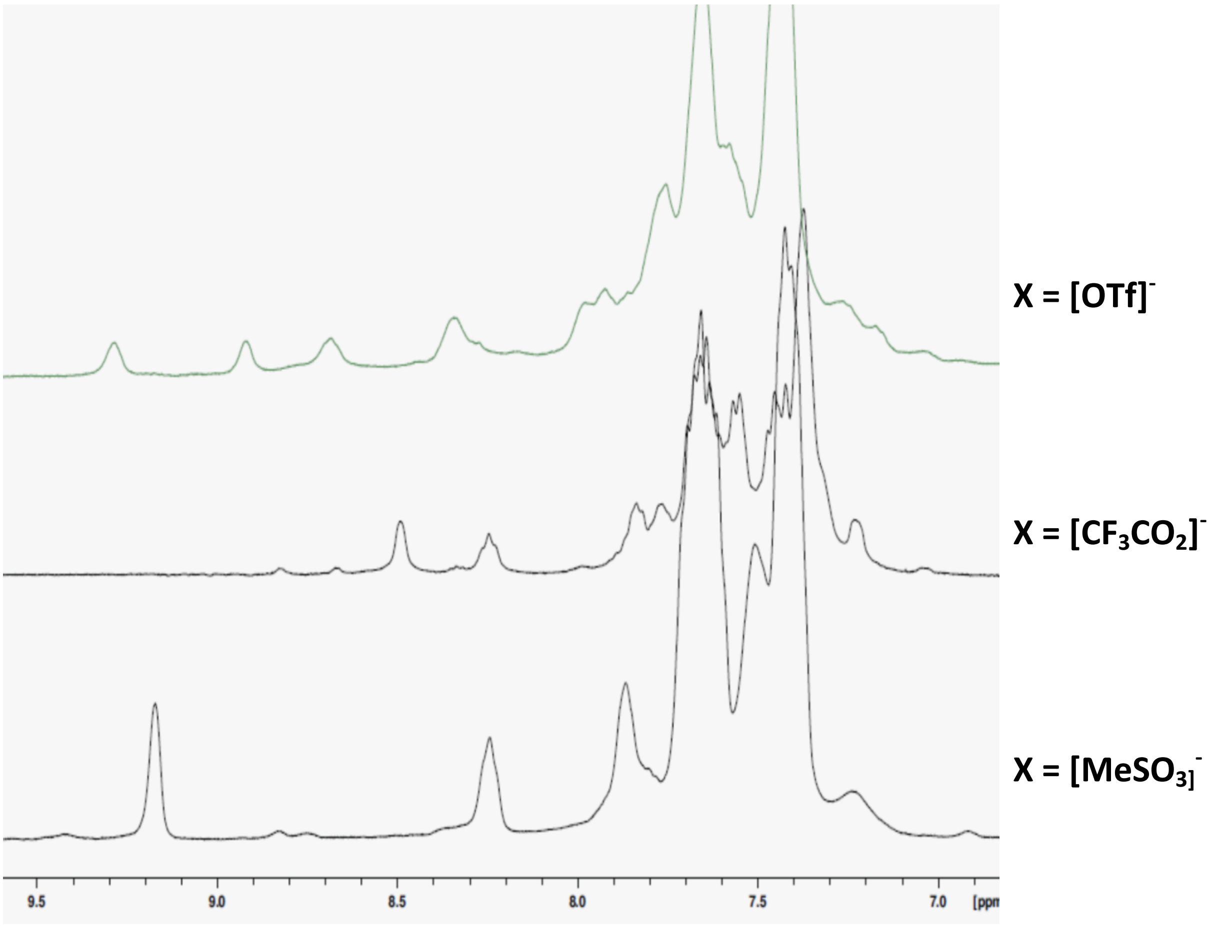

Supplementary Figure 6. **(a)** $^{31}P\{^{1}H\}$ NMR spectrum of **8'**[X], (X = OTf, $MeSO_3$, BF_4) in CH_2Cl_2 recorded at 193 K.

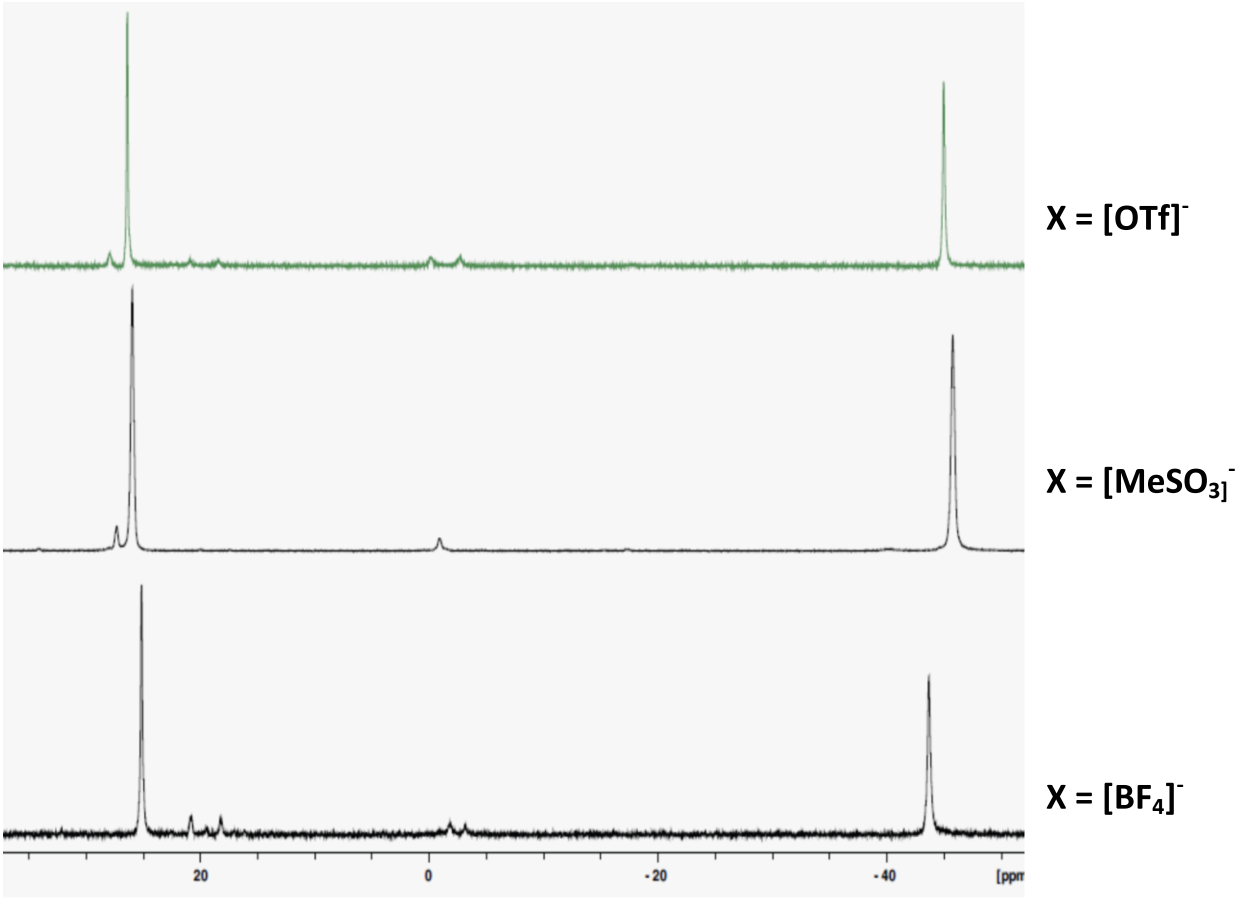

Supplementary Figure 6. **(b)** Aromatic region of the ^{1}H NMR spectra of **8'**[X], (X = OTf, MeSO$_3$, BF$_4$) in CH$_2$Cl$_2$ recorded at 193 K.

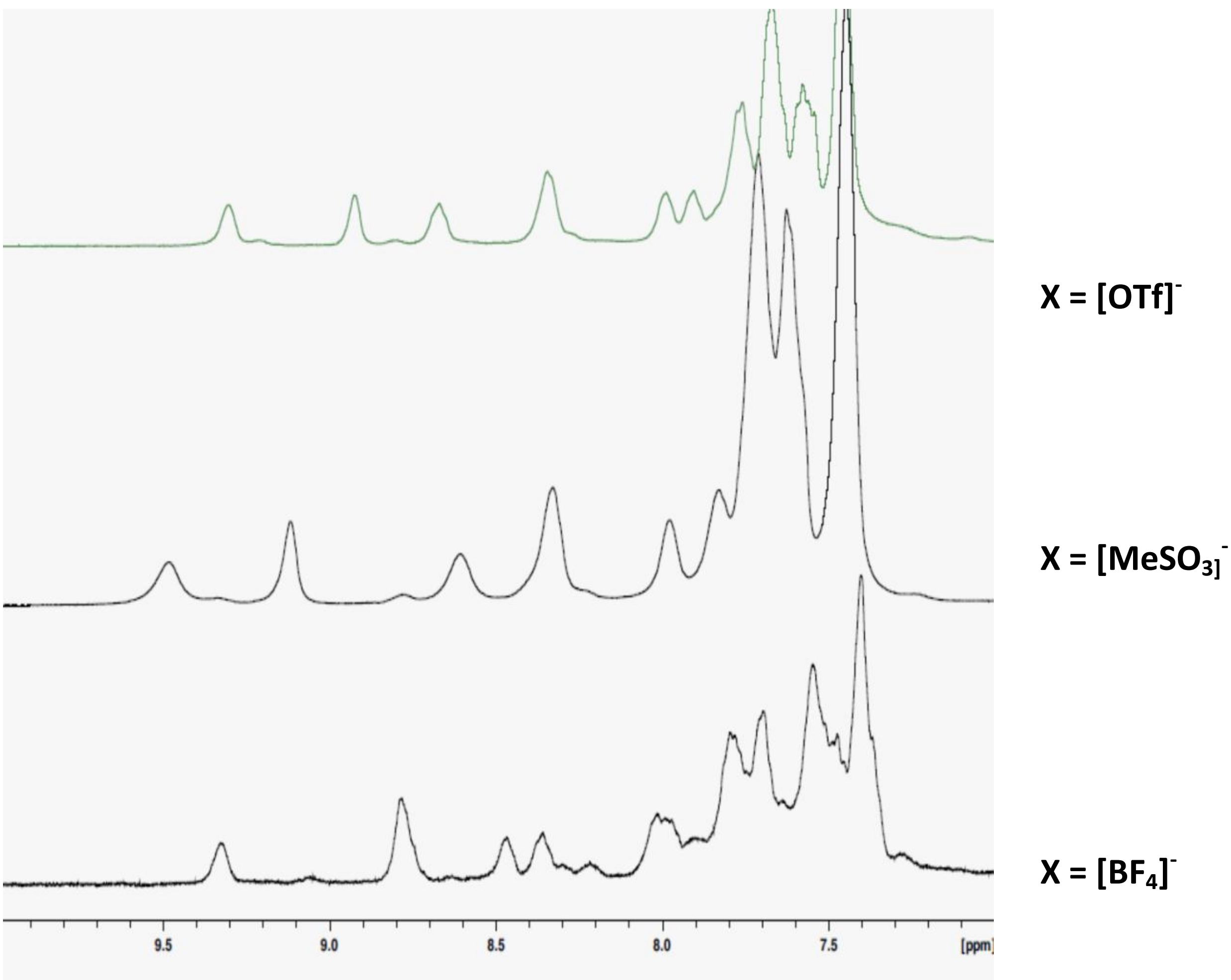

Supplementary Figure 7. $^{31}P\{^{1}H\}$ NMR spectrum of $[Pd(\kappa^2-Ph_2Ppy)(\kappa^1-Ph_2PpyH)(MeSO_3)][MeSO_3]_2$ (**8'**$[MeSO_3]$) recorded at 183 K in CH_2Cl_2 in the presence of excess $MeSO_3H$. The sharp resonance at ca. $\delta(P)$ = -10 ppm is due to $[Ph_2PpyH][MeSO_3]$.

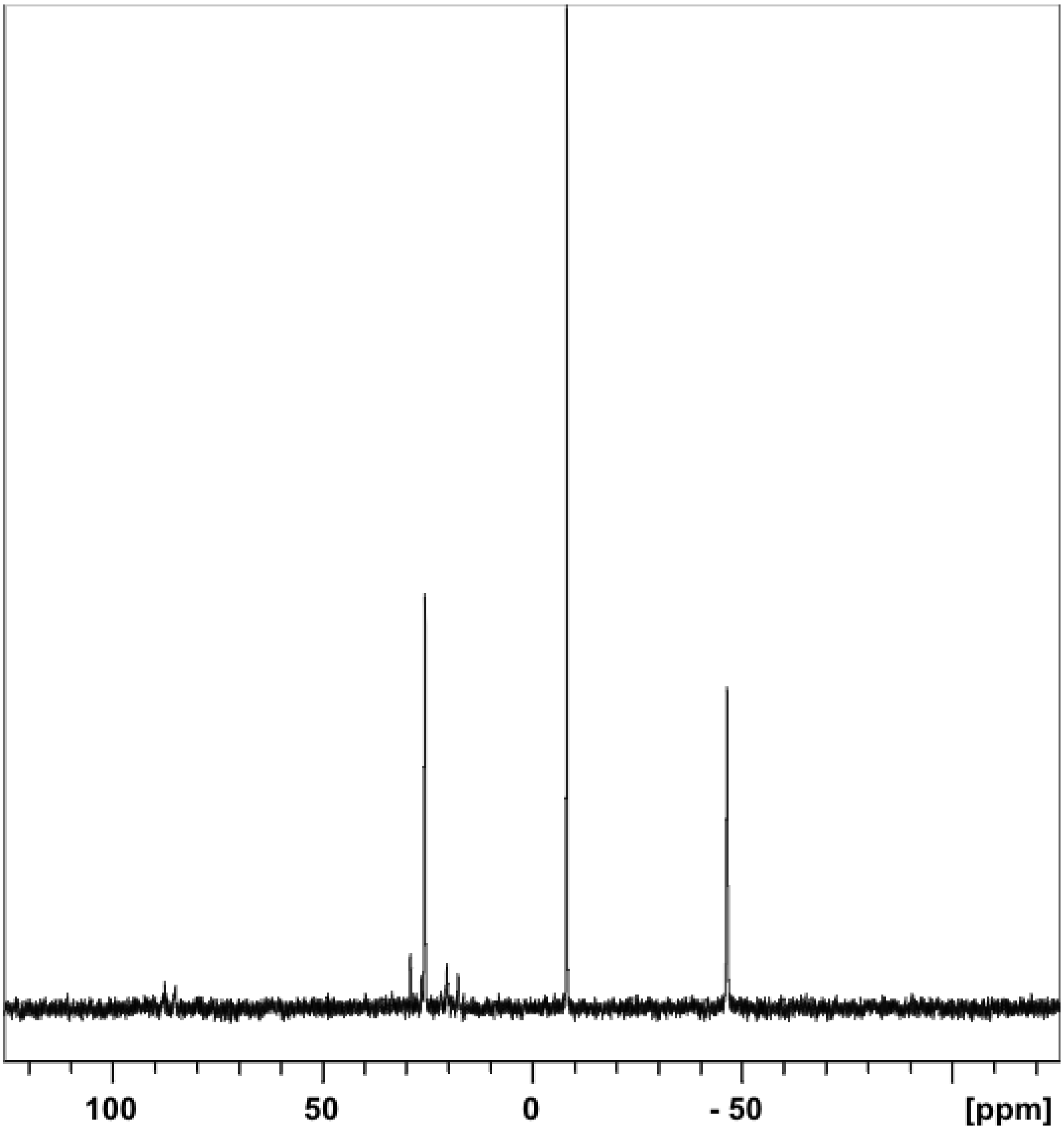

Supplementary Figure 8. (a) The ^{15}N and (b) $^{15}N\{^1H\}$ NMR spectra of Ph_2Ppy recorded at 293K in CH_2Cl_2; (c) the ^{15}N and (d) $^{15}N\{^1H\}$ NMR spectra of $[Ph_2PpyH](CH_3SO_3H)$ recorded at 203K in CH_2Cl_2

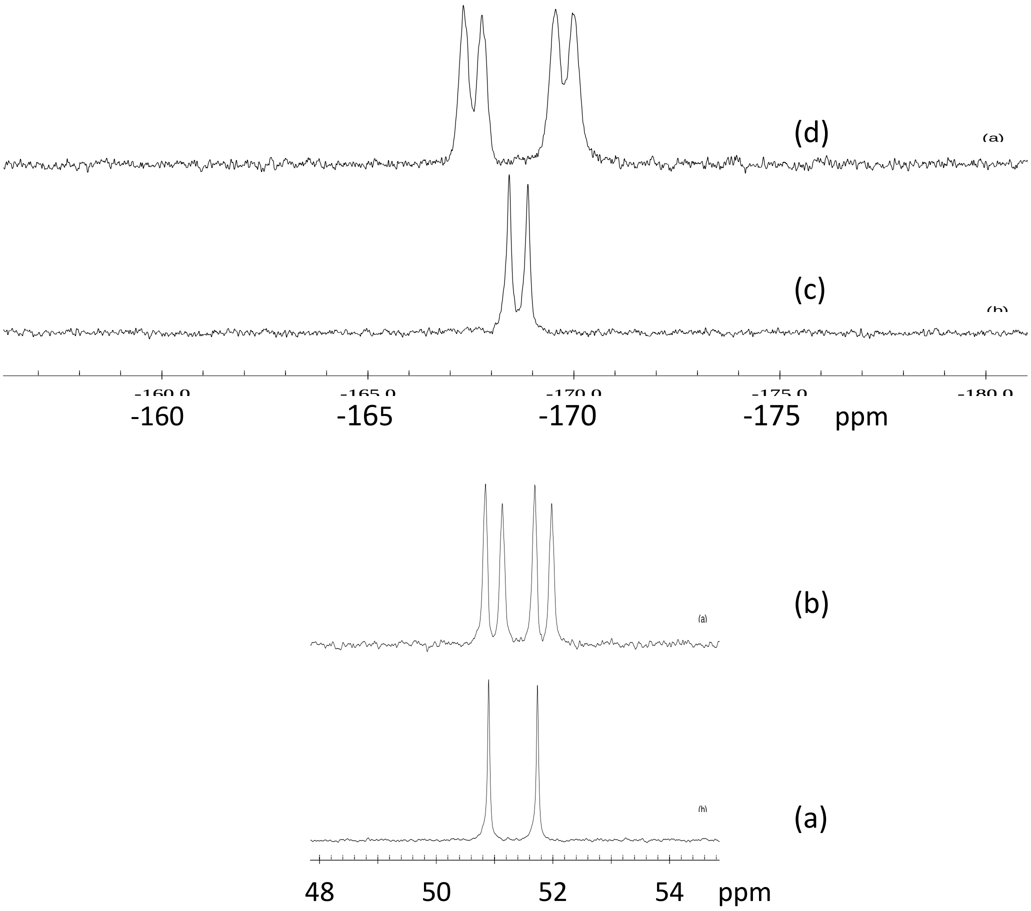

Supplementary Figure 9. Experimental and simulated variable temperature ^{31}P{^{1}H} NMR spectra of **10** in MeOH Pd:PPh$_2$py:CH$_3$SO$_3$H = 1:3.4:10. (sample 3). The sharp resonance at *ca.* -10 ppm is due to [PPh$_2$pyH]$^+$[MeSO$_3$]. (sample 3).

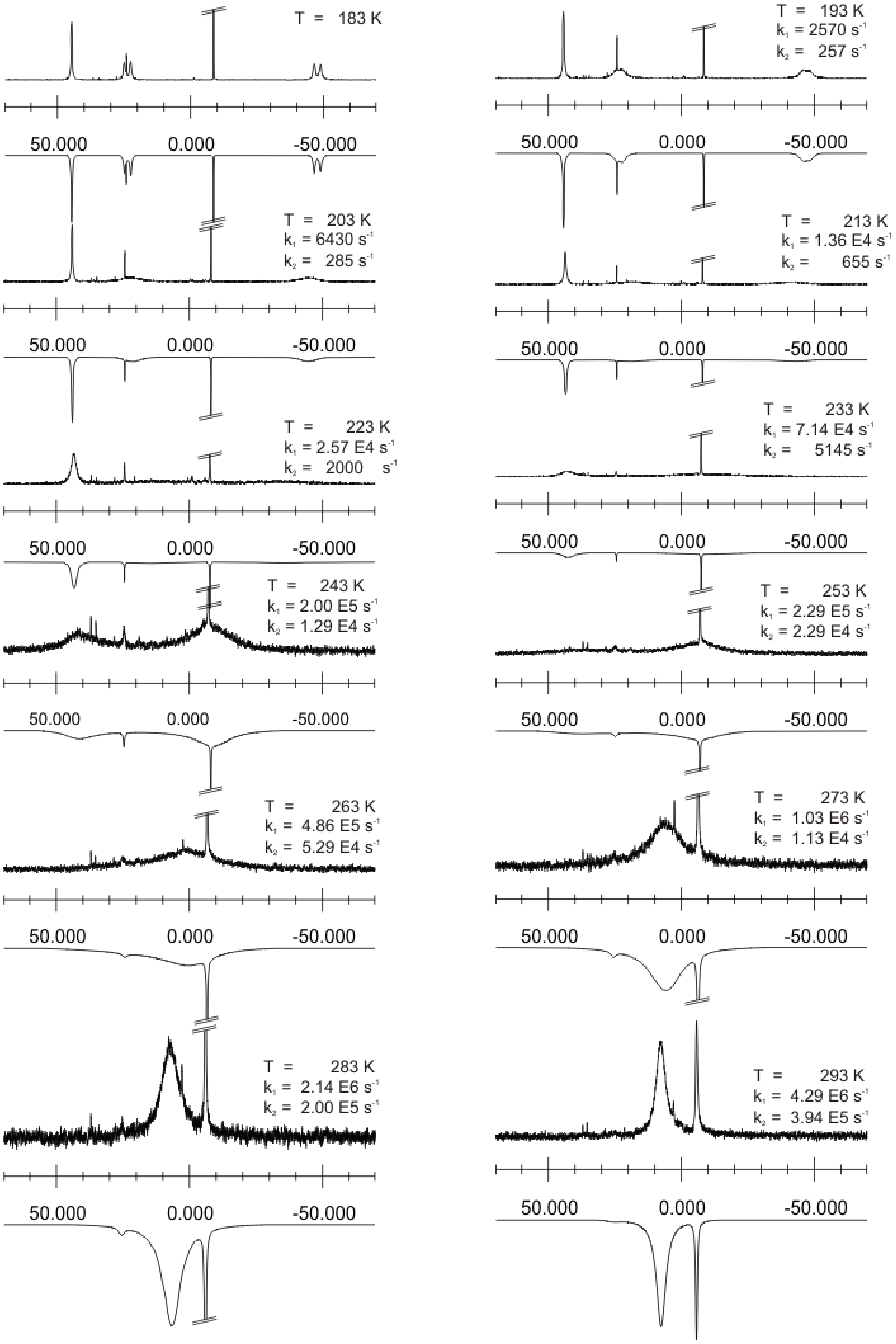

Supplementary Figure 10. Eyring and Arrhenius plots for **10** in MeOH. Pd:PPh$_3$:py:CH$_3$SO$_3$H = 1:3.4:10. (sample 3)

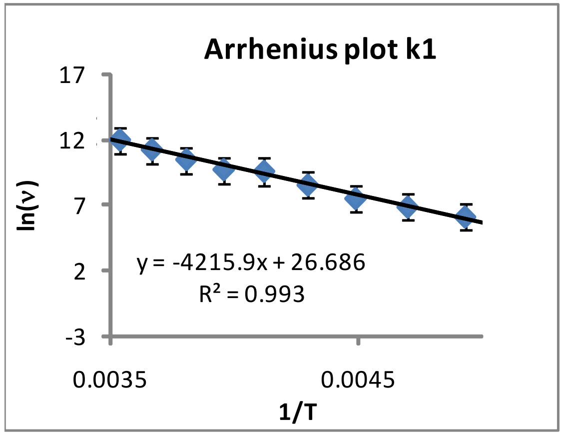
Arrhenius plot k1

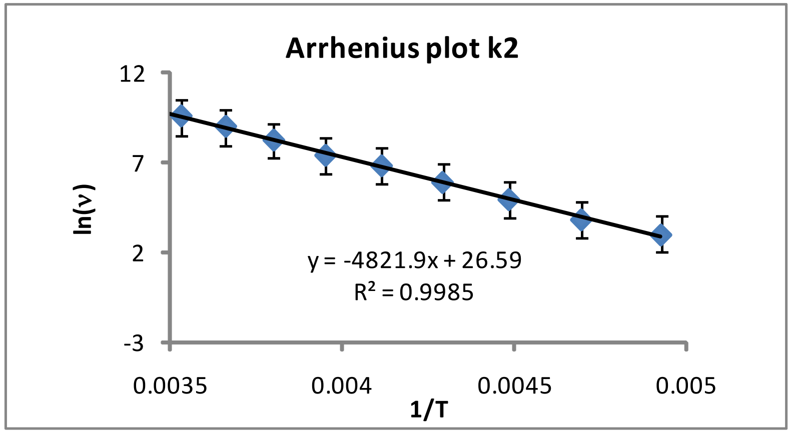
Arrhenius plot k2

h	6.63E-34	J s^{-1}
kB	1.38E-23	J K^{-1}
R	8.314	J mol^{-1} K^{-1}

Eyring	**k1**	**k2**	
intercept	22.6	22.75	
gradEy	-3911	-4579	
ΔH	33	38	kJ mol^{-1}
ΔS	-10	-8	J K^{-1} mol^{-1}
Arrhenius			
Eact	35	40	kJ mol^{-1}
gradAhr	-4216	-4822	

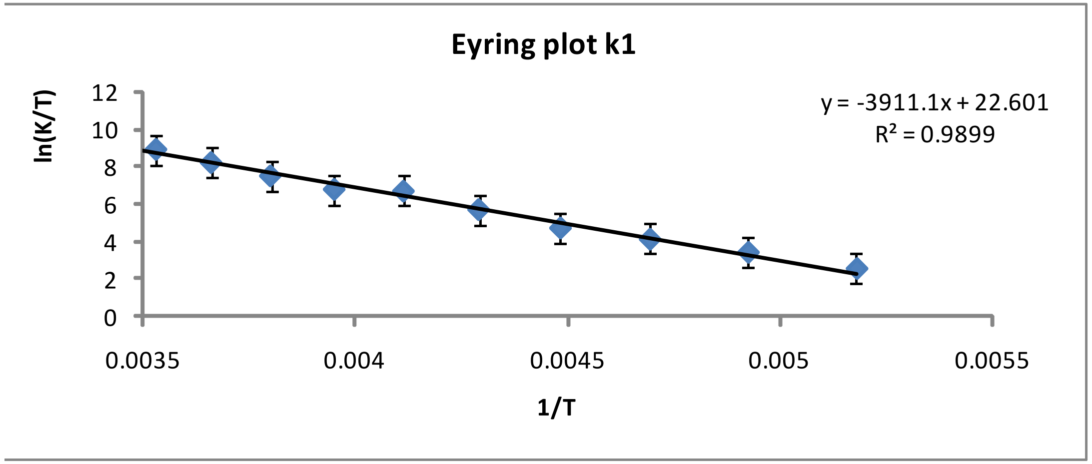
Eyring plot k1

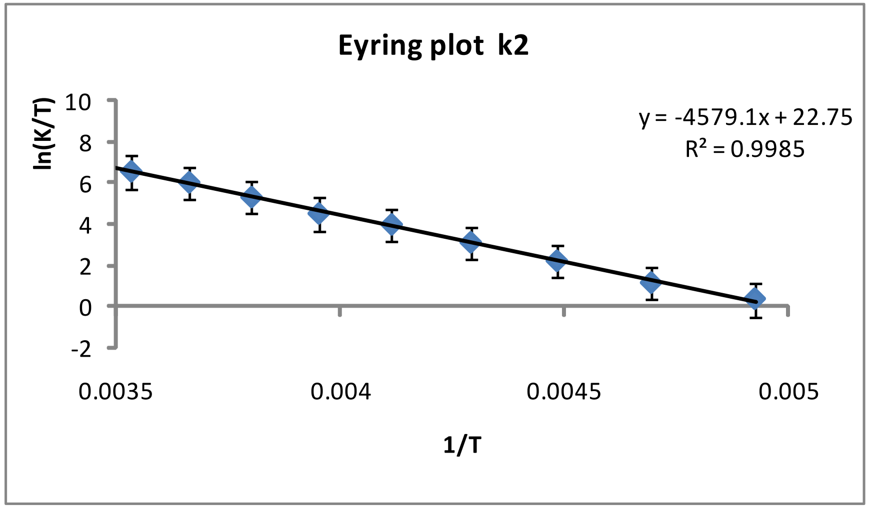
Eyring plot k2

Supplementary Figure 11. Experimental and simulated variable temperature $^{31}P\{^{1}H\}$ NMR spectra of **10** in MeOH Pd:PPh$_2$py:CH$_3$SO$_3$H = 1:3.4:25. The resonance at *ca.* -10 ppm is due to [PPh$_2$pyH]$^+$[MeSO$_3$]. (sample 4)

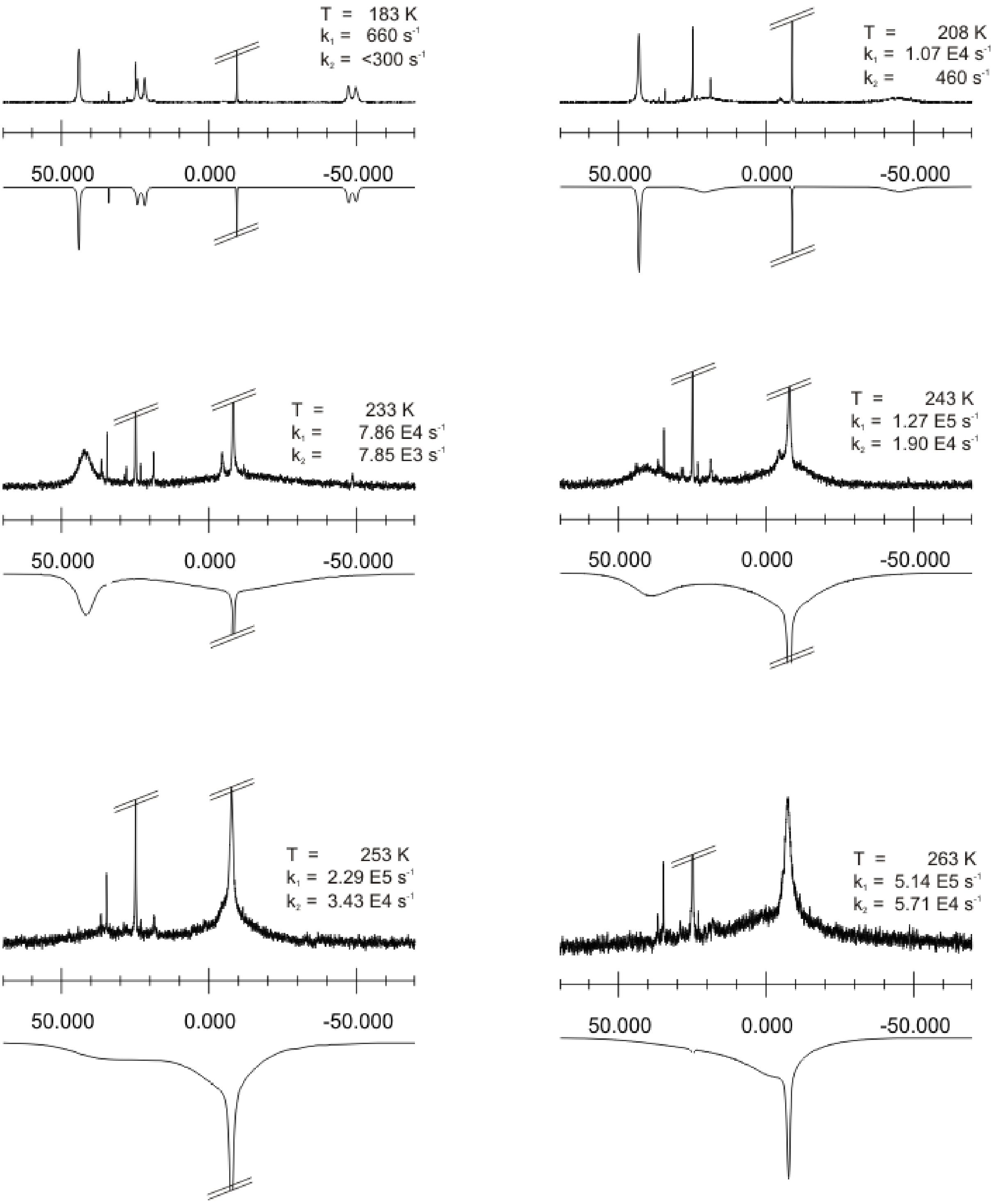

Supplementary Figure 12. Eyring and Arrhenius plots for **10** in MeOH. Pd:PPh$_3$:py:CH$_3$SO$_3$H = 1:3:4:25. (sample 4)

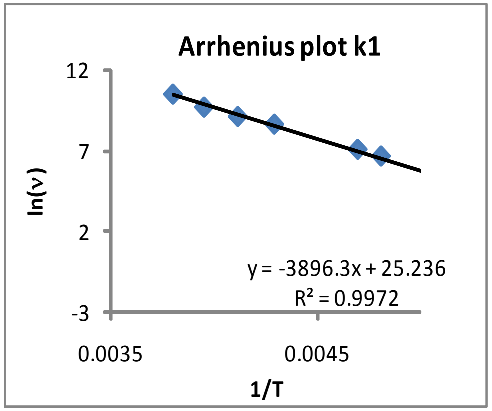

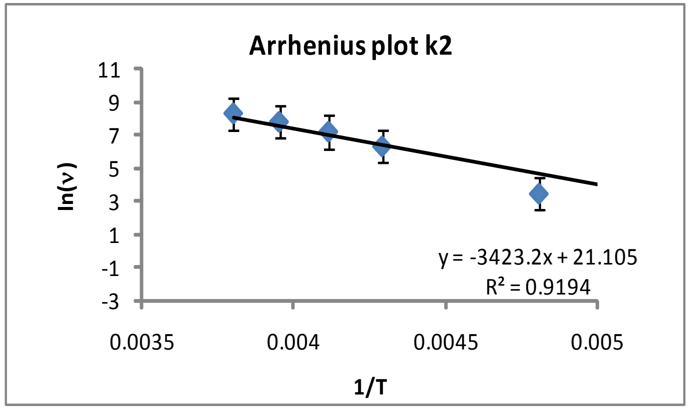

h	6.63E-34	J s^{-1}
kB	1.38E-23	J K^{-1}
R	8.314	J mol^{-1} K^{-1}

Eyring	**k1**	**k2**
intercept	20.756	19.798
gradEy	-3515	-4654
ΔH	29	39 kJ mol^{-1}
ΔS	-25	-33 J K^{-1} mol^{-1}
Arrhenius		
Eact	31	41 kJ mol^{-1}
gradAhr	-3747	-4886

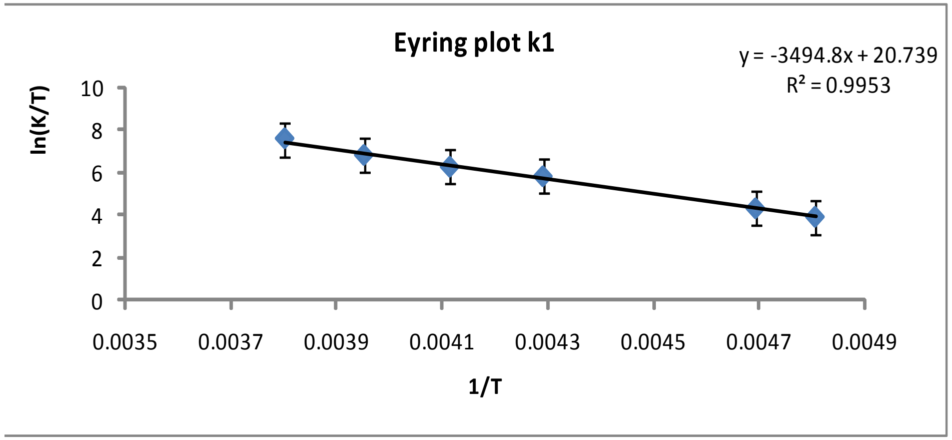

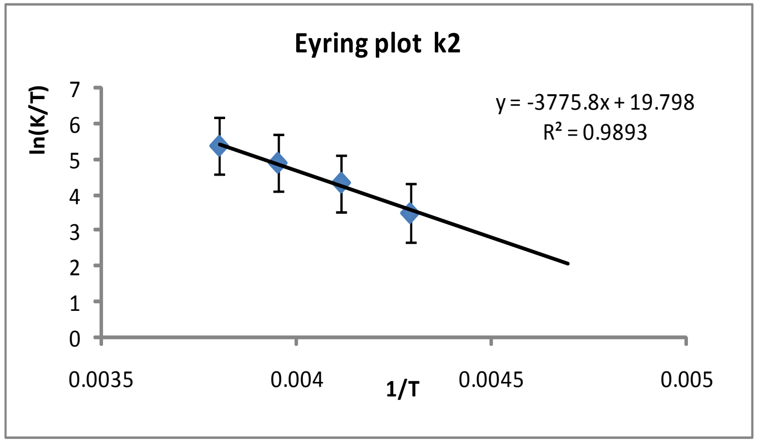

Supplementary Figure 13. Experimental and simulated variable temperature $^{31}P\{^{1}H\}$ NMR spectra of **10** in MeOH Pd:PPh$_2$py:CH$_3$SO$_3$H = 1:3.2:15.

(sample 5)

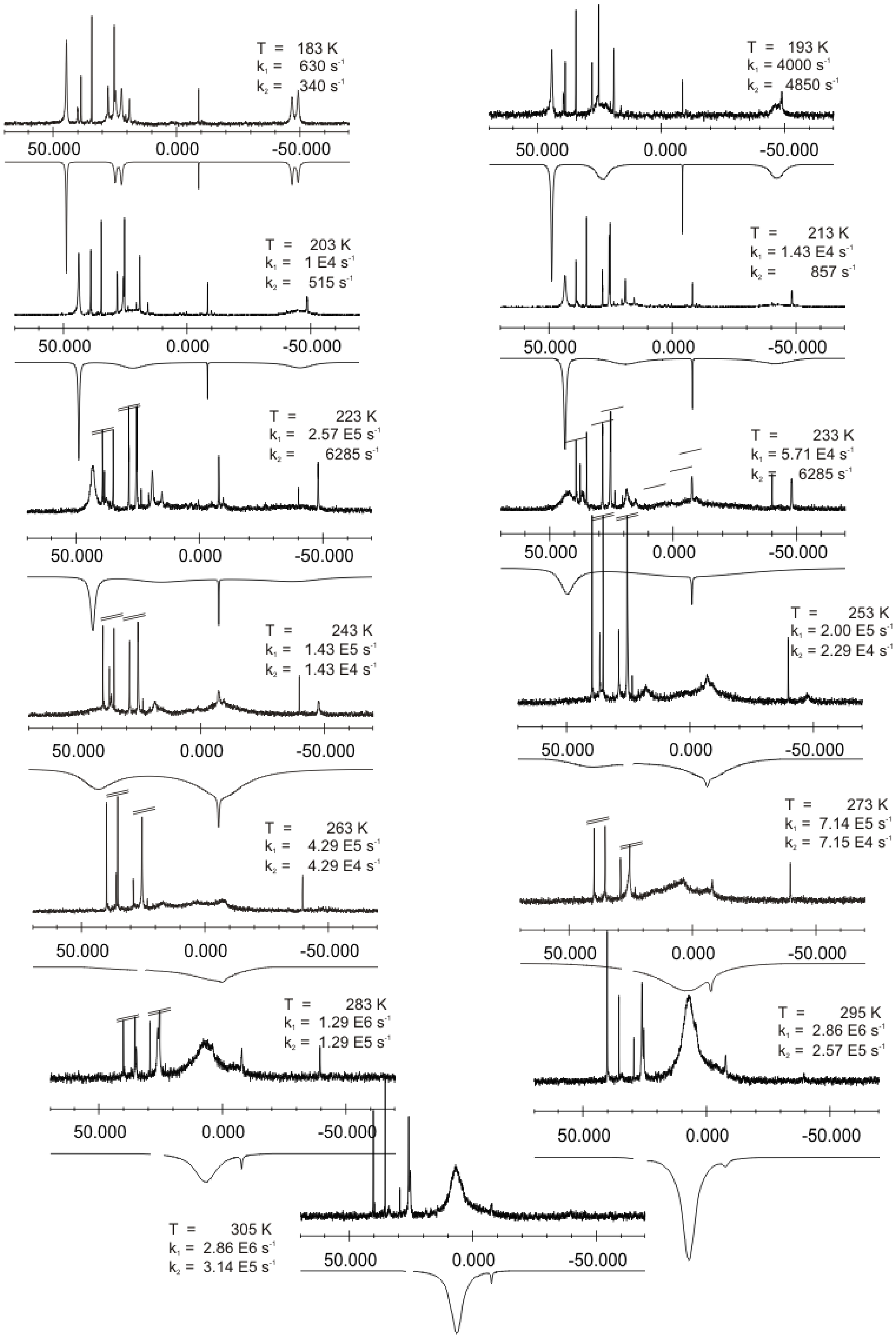

Supplementary Figure 14. Eyring and Arrhenius plots for Eyring and Arrhenius plots for **10** in MeOH Pd:PPh$_2$py:CH$_3$SO$_3$H = 1:3.2:15. (sample 5).

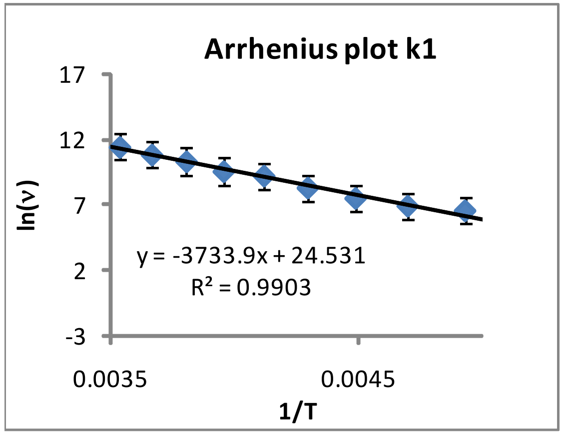

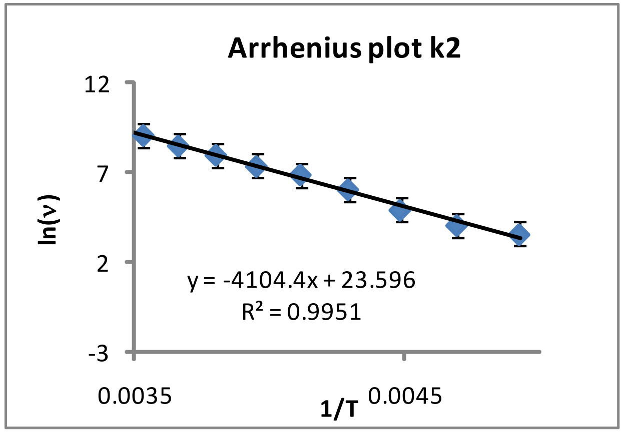

h	6.63E-34		J s^{-1}
kB	1.38E-23		J K^{-1}
R	8.314		J mol^{-1} K^{-1}
Eyring	**k1**	**k2**	
intercept	20.72	19.74	
gradEy	-3500	-3857	
ΔH	29	32	kJ mol^{-1}
ΔS	-25	-33	J K^{-1} mol^{-1}
Arrhenius			
Eact	31	34	kJ mol^{-1}
gradAhr	-3734	-4104	

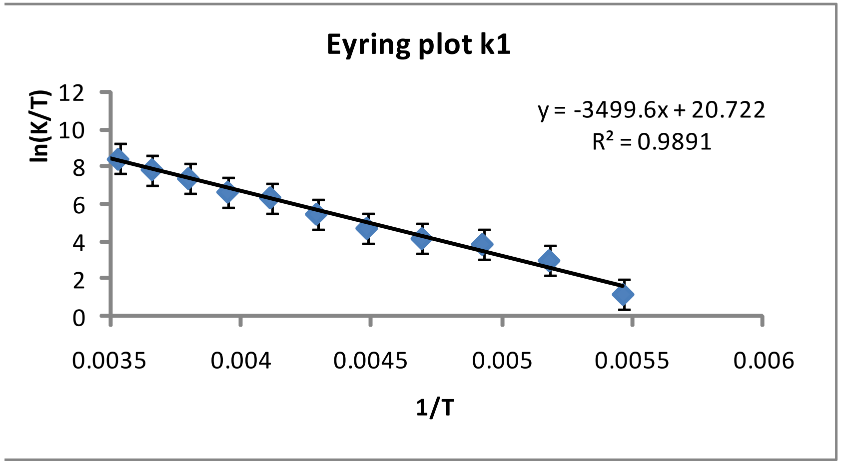

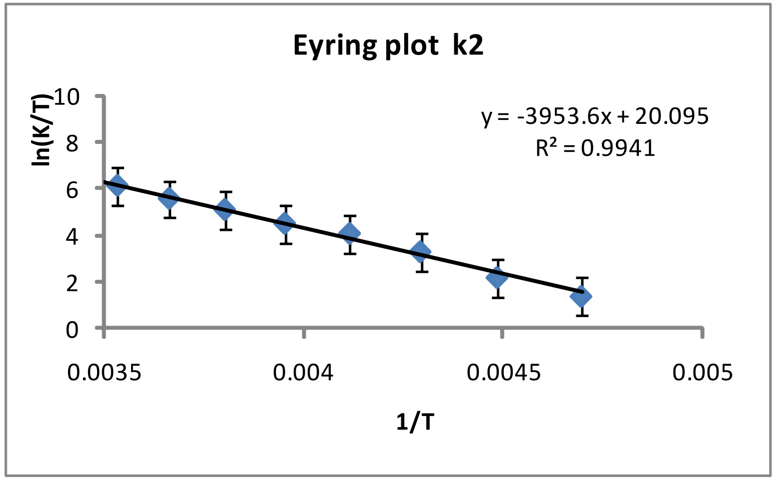

Supplementary Figure 15. Experimental and simulated variable temperature ^{31}P{^{1}H} NMR spectra of **10** in MeOH Pd:PPh$_2$py:CH$_3$SO$_3$H = 1:2.9:25. (sample 6).

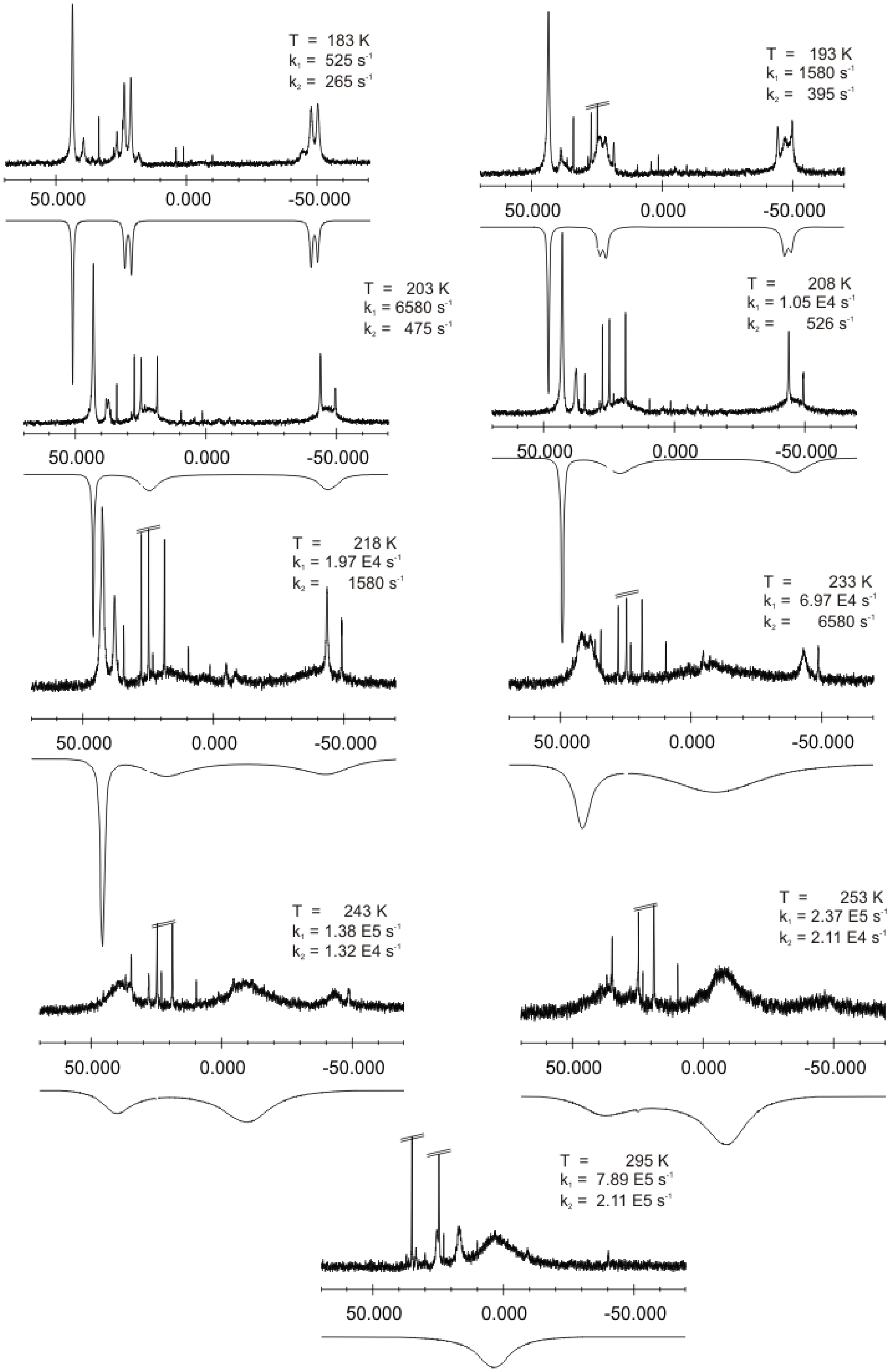

Supplementary Figure 16. Eyring and Arrhenius plots for **10** in MeOH Pd:PPh_3:py:CH_3SO_3H = 1:2:9:25. (sample 6).

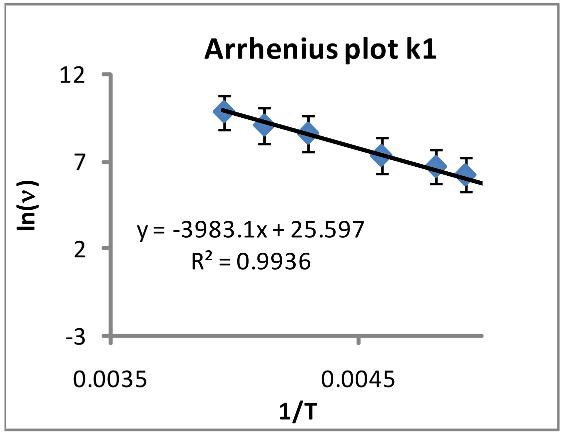

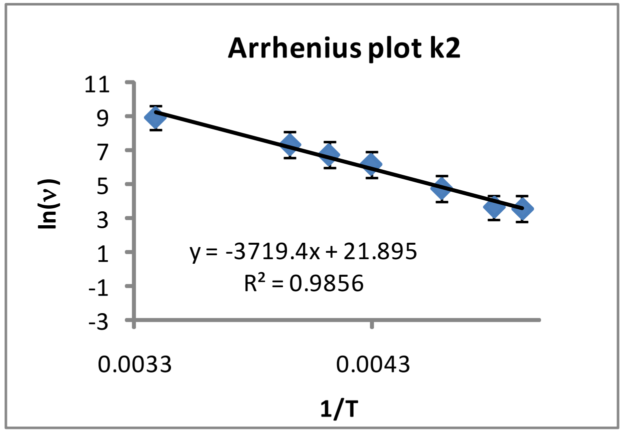

h	6.63E-34		J s^{-1}
kB	1.38E-23		J K^{-1}
R	8.314		J mol^{-1} K^{-1}
Eyring	**k1**	**k2**	
intercept	21.7	20.75	
gradEy	-3736	-4101	
ΔH	31	34	kJ mol^{-1}
ΔS	-17	-25	J K^{-1} mol^{-1}
Arrhenius			
Eact	34	31	kJ mol^{-1}
gradAhr	-4046	-3719	

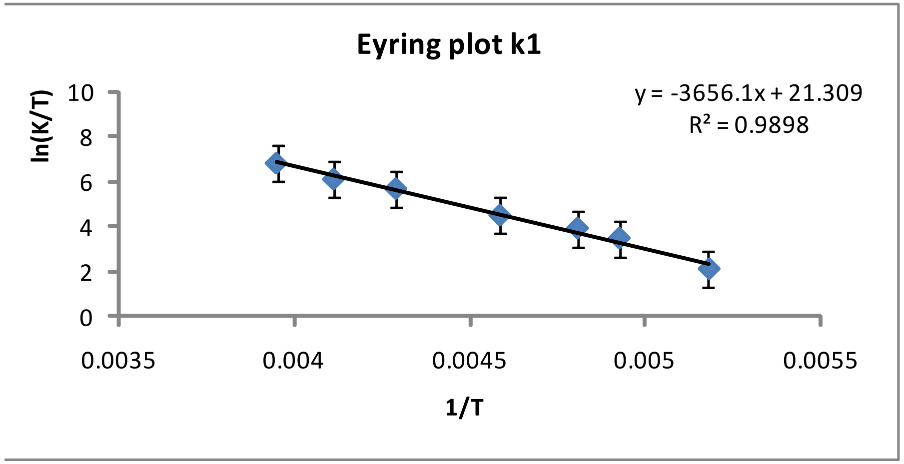

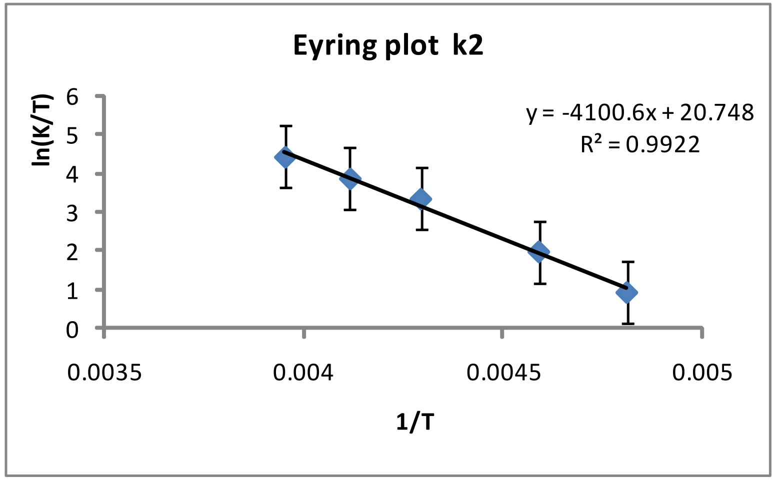

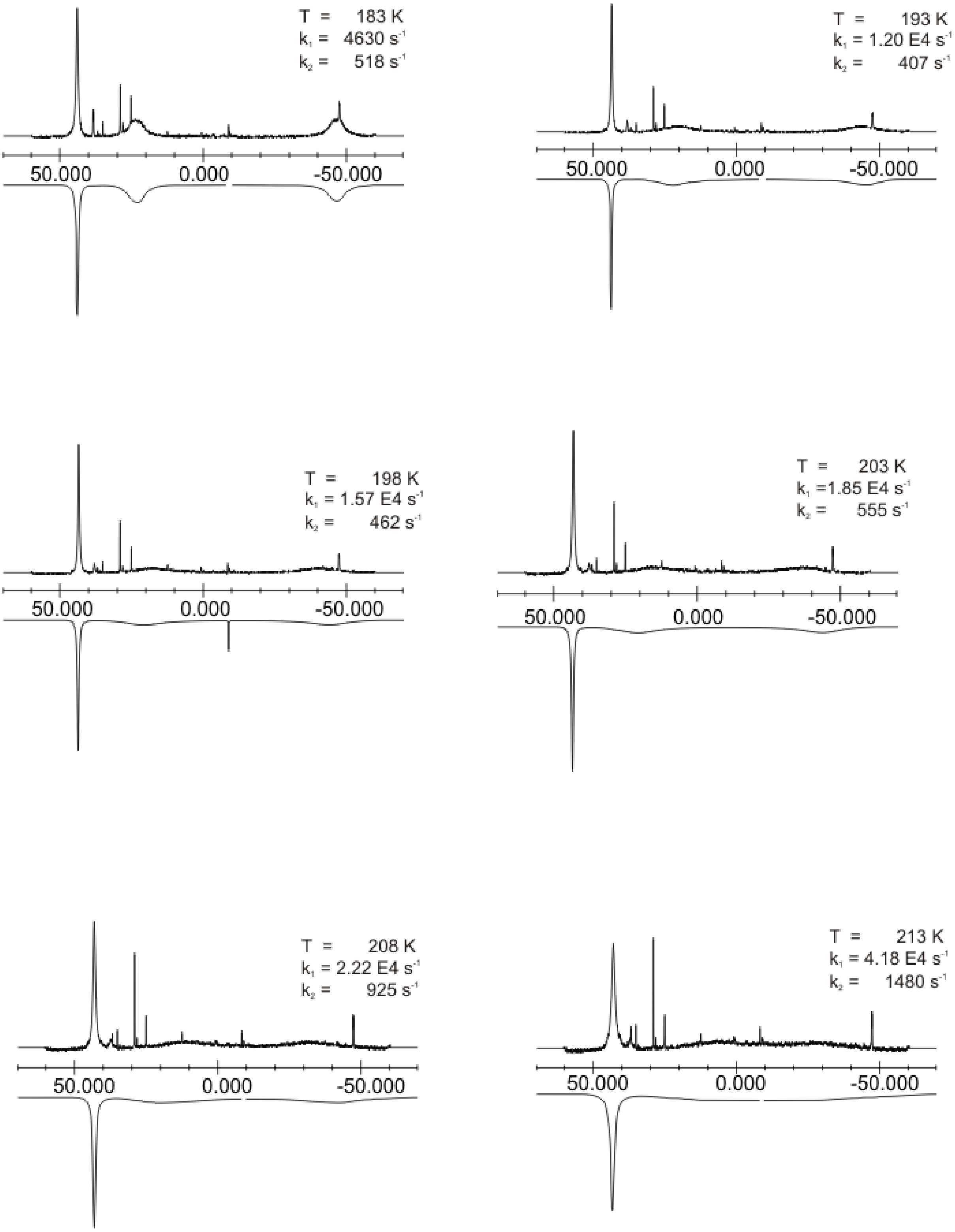

Supplementary Figure 17. Experimental and simulated variable temperature $^{31}P\{^1H\}$ NMR spectra of **10** MeOH:CD$_2$Cl$_2$ 4:3; Pd:PPh$_2$py:CH$_3$SO$_3$H = 1:3.1:5. (sample 8)

Supplementary Fig 17 continued

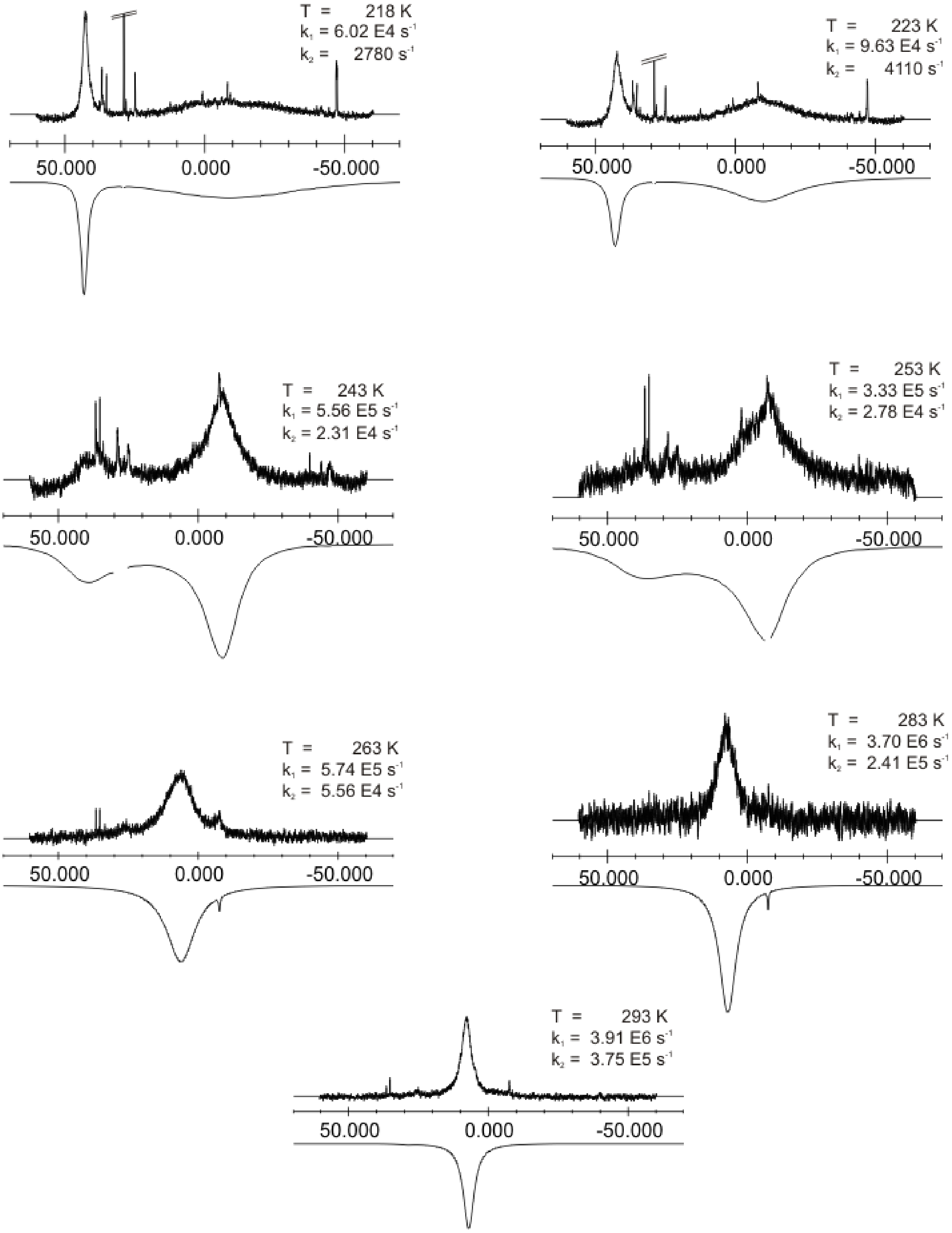

Supplementary Figure 18. Eyring and Arrhenius plots for **10** MeOH:CD$_2$Cl$_2$ 4:3; Pd:PPh$_3$:py:CH$_3$SO$_3$H = 1:3.1:5. (sample 8)

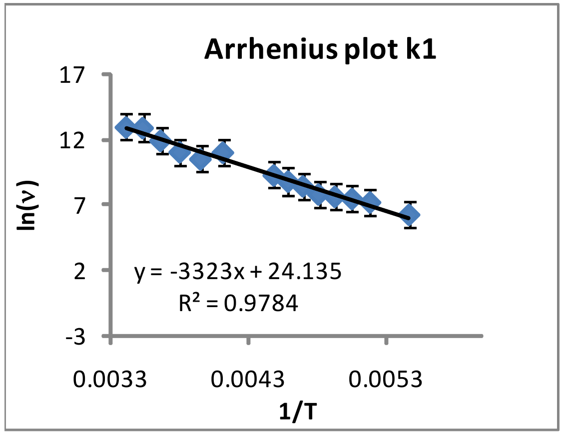

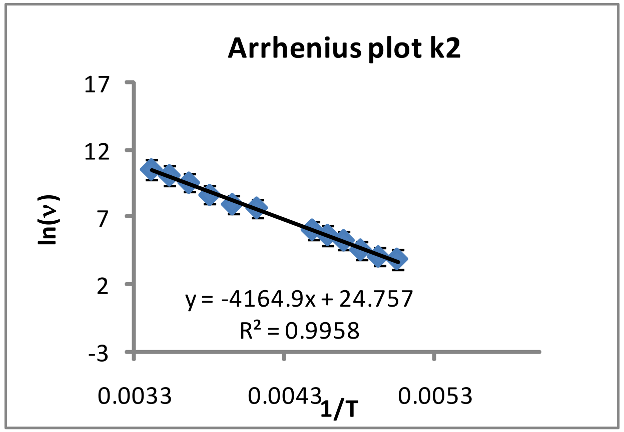

h	6.63E-34	J s^{-1}
kB	1.38E-23	J K^{-1}
R	8.314	J mol^{-1} K^{-1}

Eyring	**k1**	**k2**
intercept	21.38	20.71
gradEy	-2905	-3684
ΔH	24	31 kJ mol^{-1}
ΔS	-20	-25 J K^{-1} mol^{-1}
Arrhenius		
Eact	28	33 kJ mol^{-1}
gradAhr	-3323	-3978

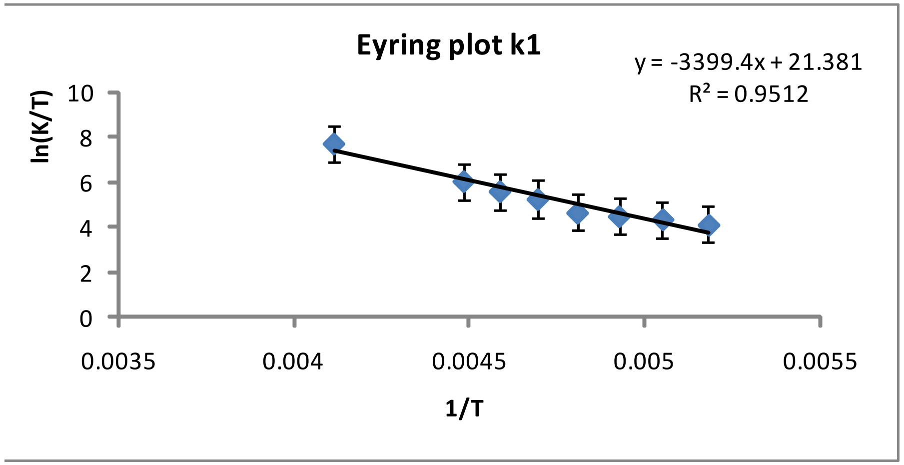

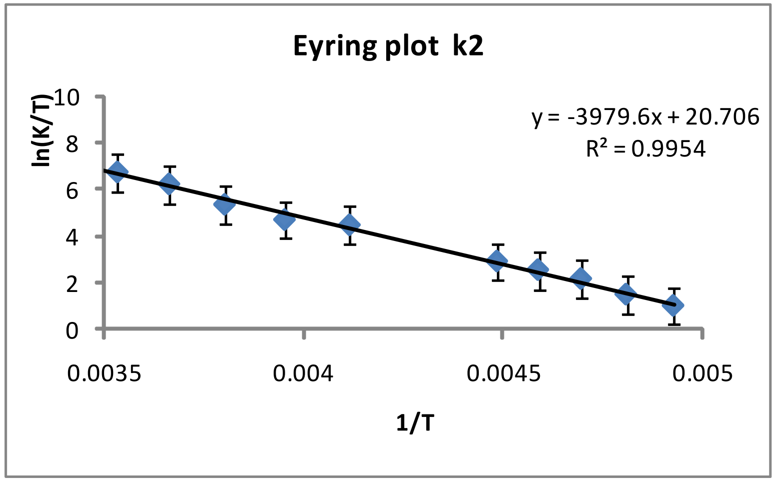

Supplementary Figure 19. Experimental and simulated variable temperature ^{31}P{^{1}H} NMR spectra of **10** in MeOH. Pd:PPh$_2$py:CH$_3$SO$_3$H = 1:3.1:10. (sample 1)

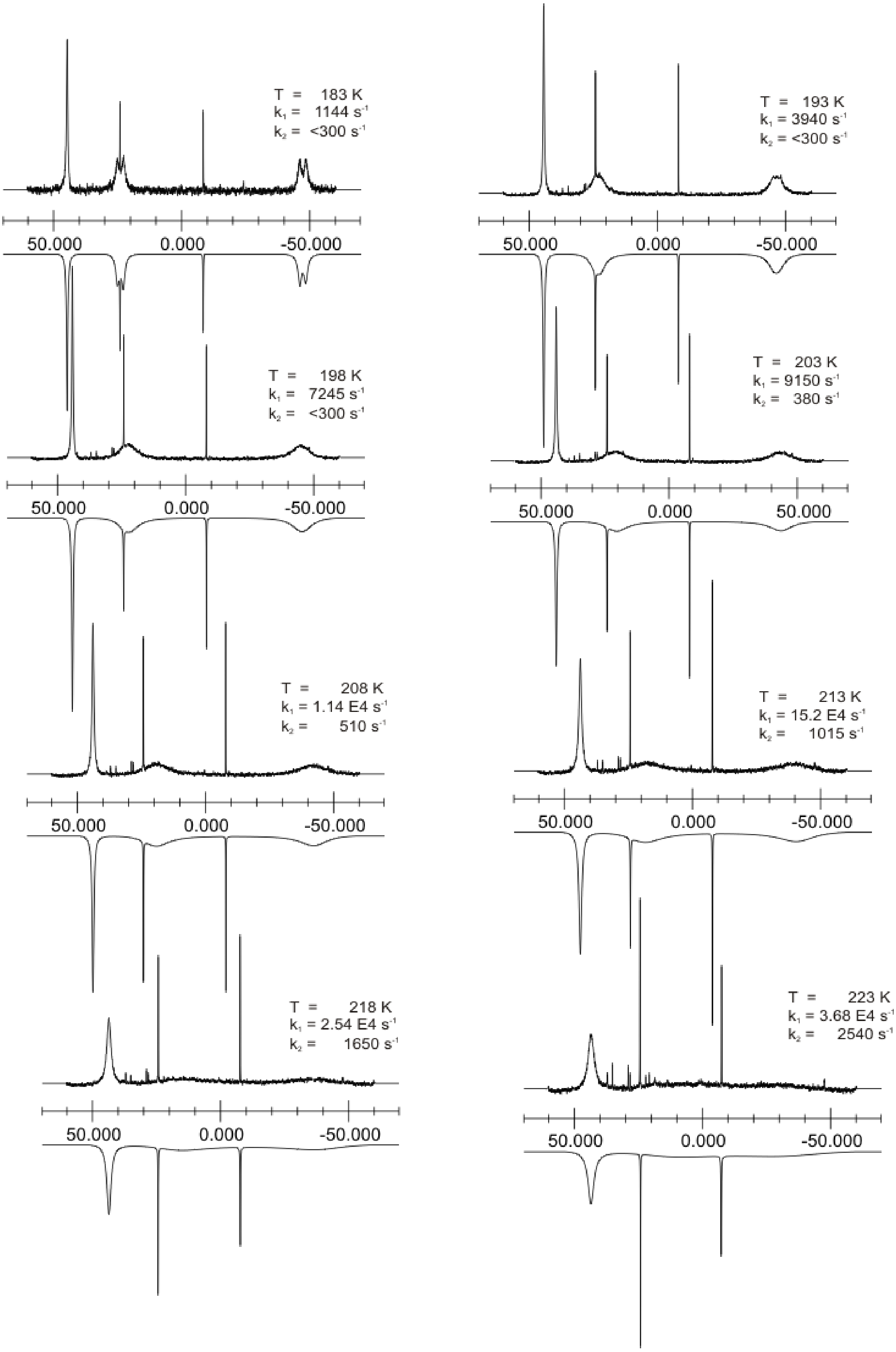

Supplementary Fig 19 continued

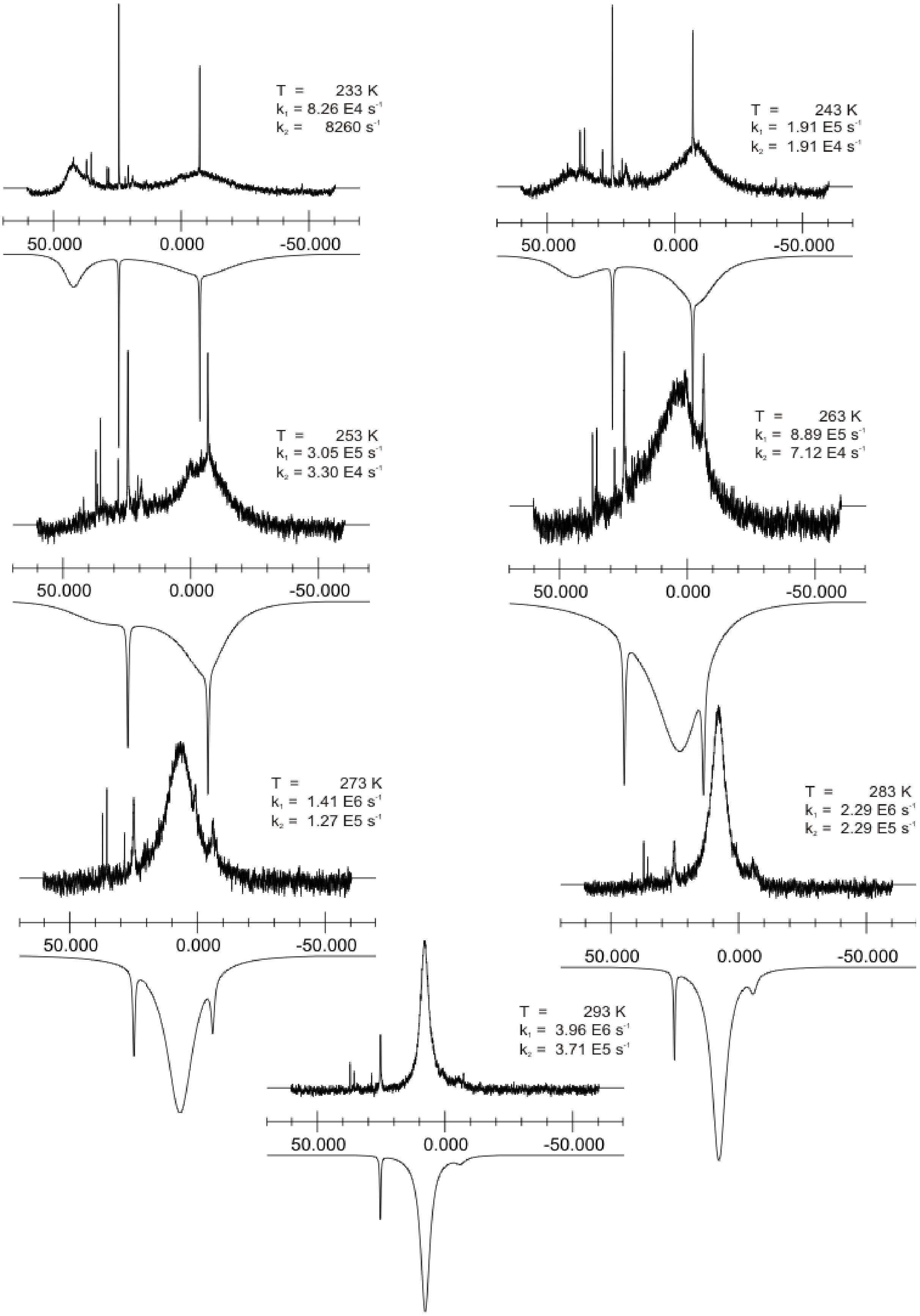

Supplementary Figure 20. Eyring and Arrhenius plots for **10** in MeOH. Pd:PPh$_2$py:CH$_3$SO$_3$H = 1:3.1:10. (sample 1)

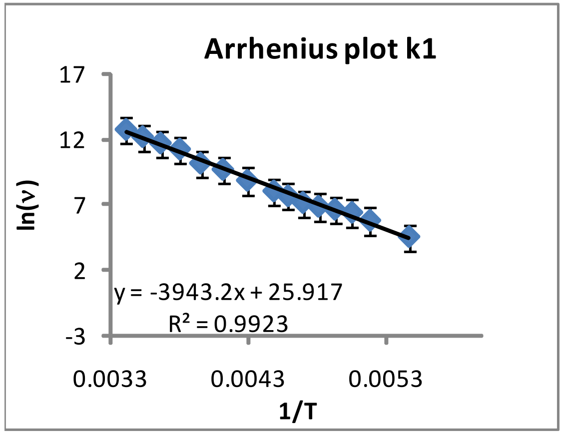

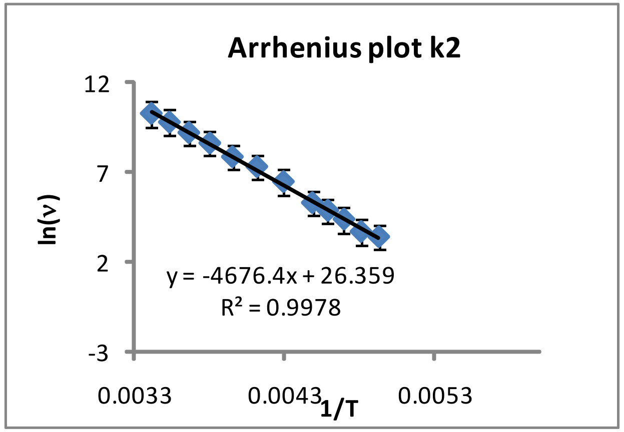

h	6.63E-34	J s^{-1}
kB	1.38E-23	J K^{-1}
R	8.314	J mol^{-1} K^{-1}

Eyring	**k1**	**k2**	
intercept	22.01	22.41	
gradEy	-3713	-4435	
ΔH	31	37	kJ mol^{-1}
ΔS	-15	-11	J K^{-1} mol^{-1}
Arrhenius			
Eact	33	39	kJ mol^{-1}
gradAhr	-3943	-4676	

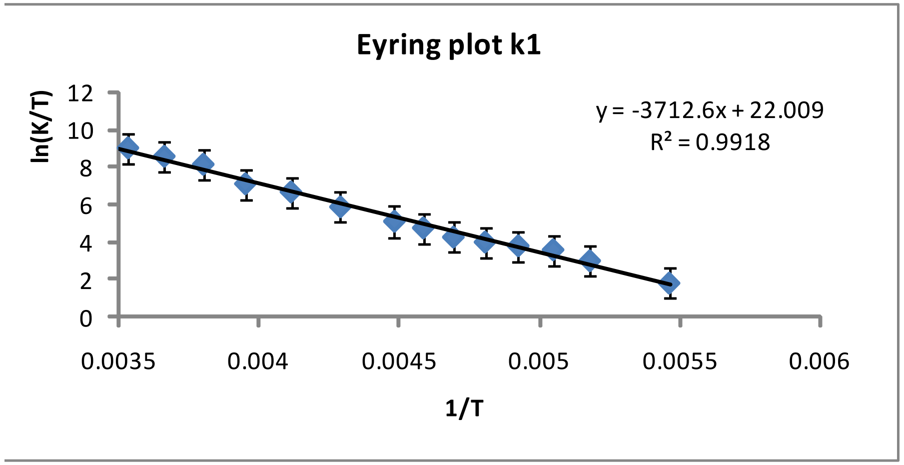

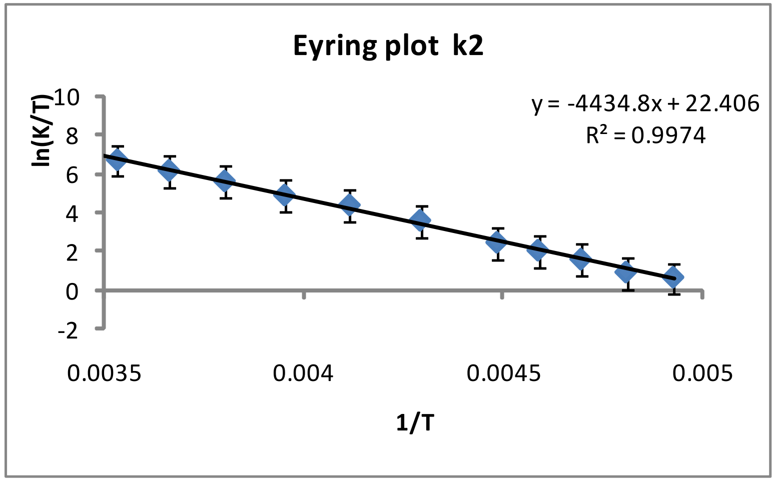

Supplementary Figure 21. Experimental and simulated variable temperature $^{31}P\{^1H\}$ NMR spectra of **10** in MeOH Pd:PPh$_2$py:CH_3SO_3H = 1:3.1:10. (sample 2).

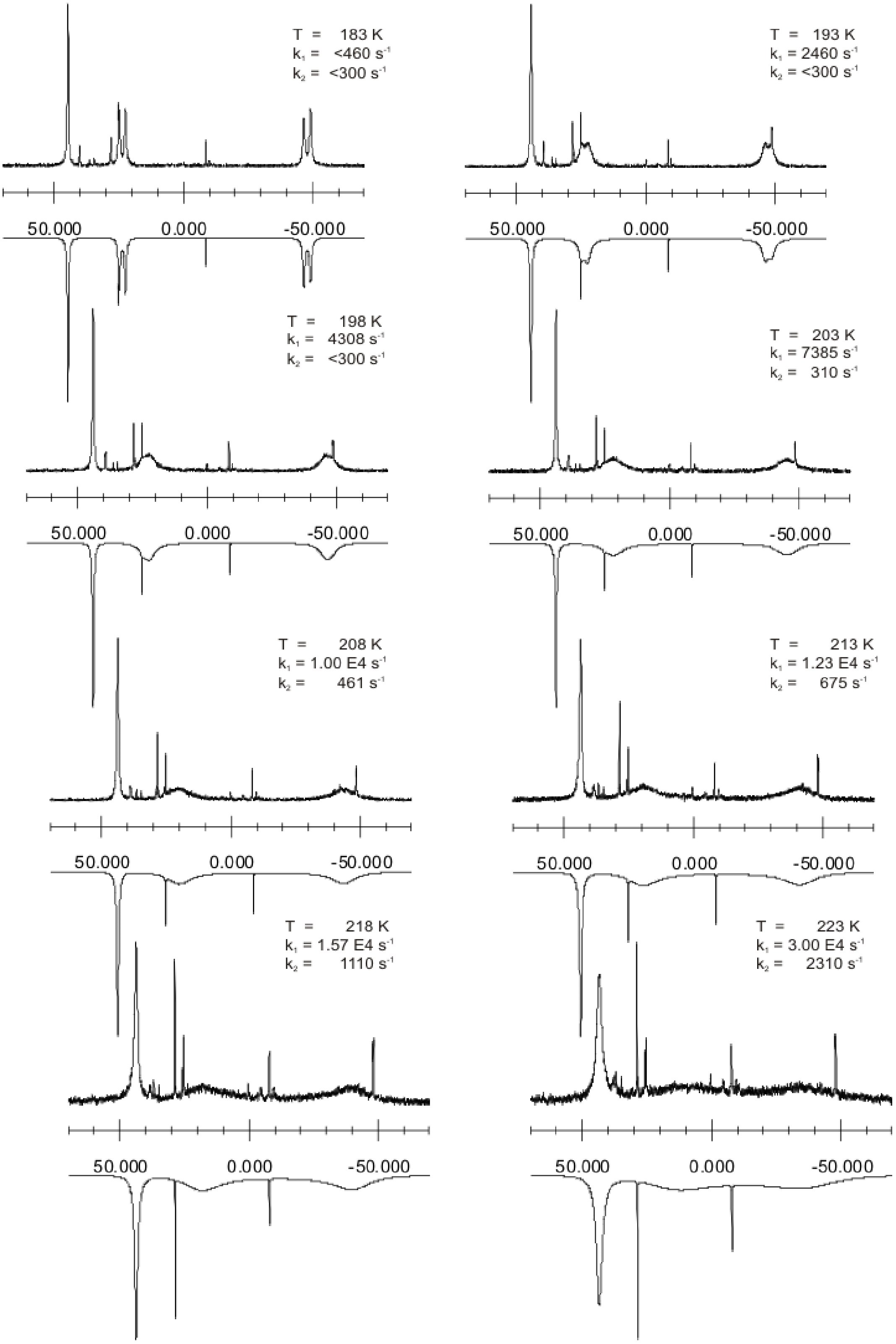

Supplementary Fig 21 continued

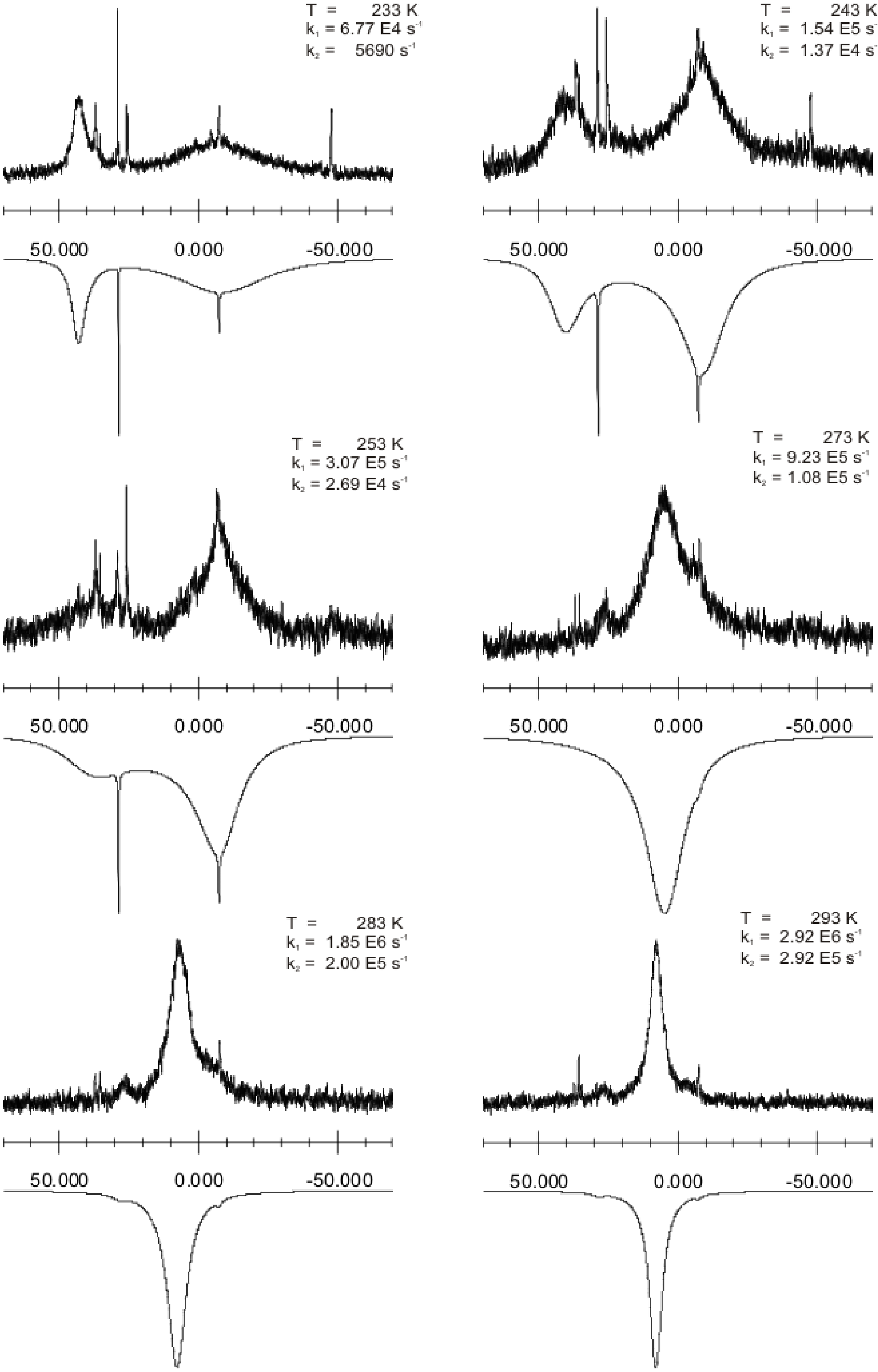

Supplementary Figure 22. Eyring and Arrhenius plots for **10** in MeOH. Pd:PPh_3:py:CH_3SO_3H = 1:3.1:10. (sample 2).

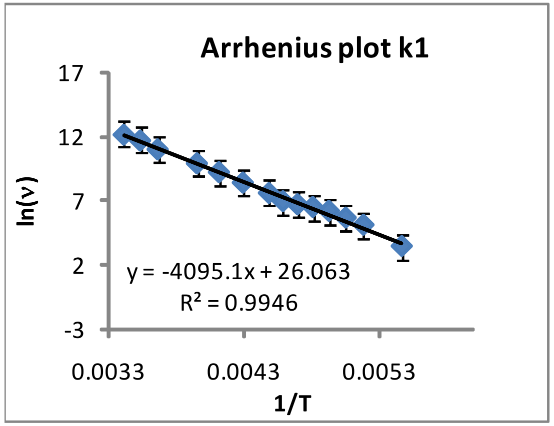

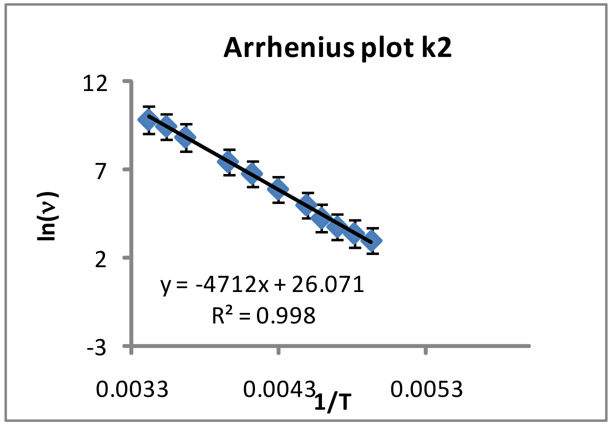

h	6.63E-34	J s^{-1}
kB	1.38E-23	J K^{-1}
R	8.314	J mol^{-1} K^{-1}

Eyring	**k1**	**k2**
intercept	22.277	22.301
gradEy	-3850	-4470
ΔH	32	37 kJ mol^{-1}
ΔS	-12	-12 J K^{-1} mol^{-1}
Arrhenius		
Eact	34	39 kJ mol^{-1}
gradAhr	-4095	-4712

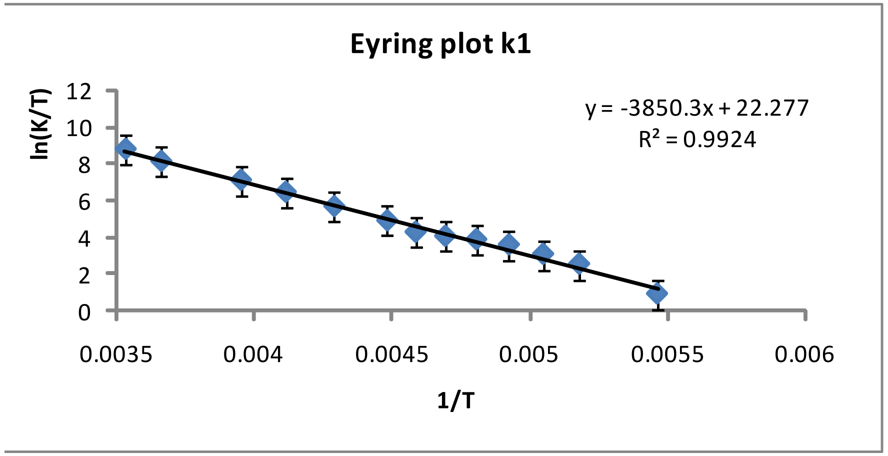

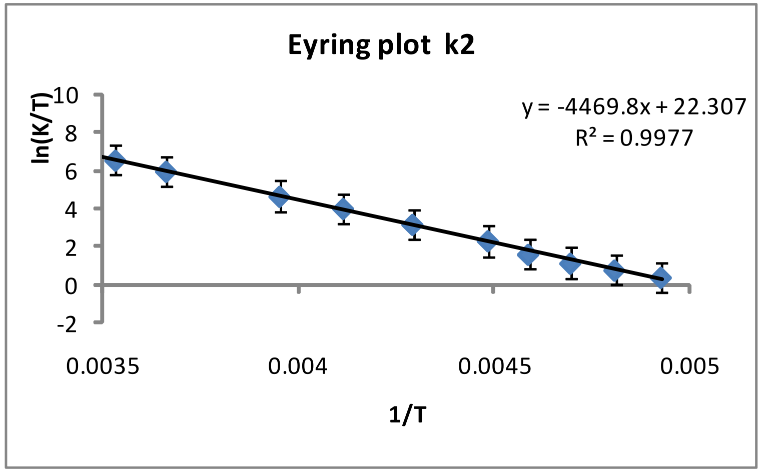

Supplementary Figure 23. Experimental and simulated variable temperature $^{31}P\{^1H\}$ NMR spectra of **10** in MeOH:CD_2Cl_2 (2:9) Pd:PPh_2py:CH_3SO_3H = 1:3.1:25. (sample 7).

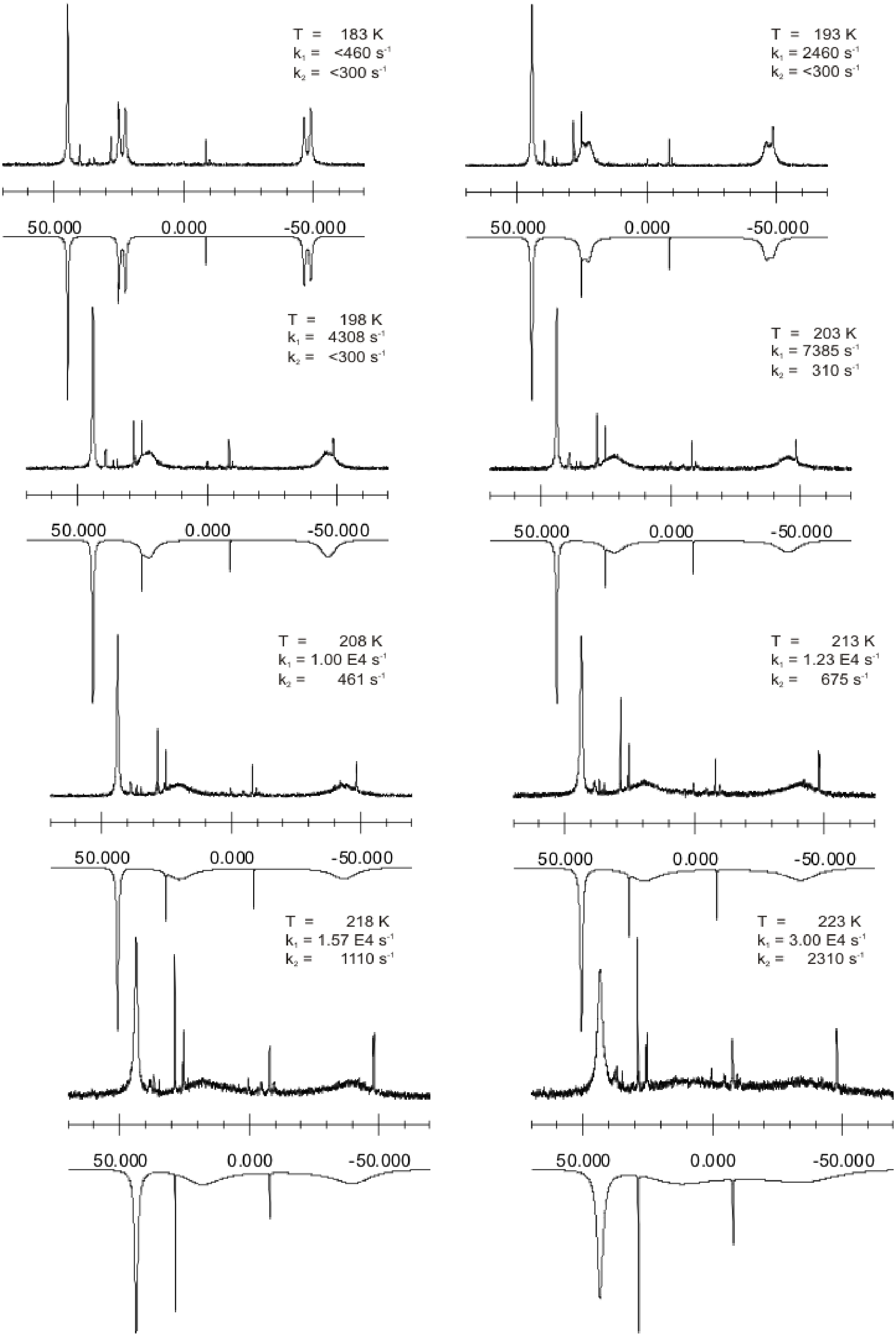

Supplementary Fig 23 continued

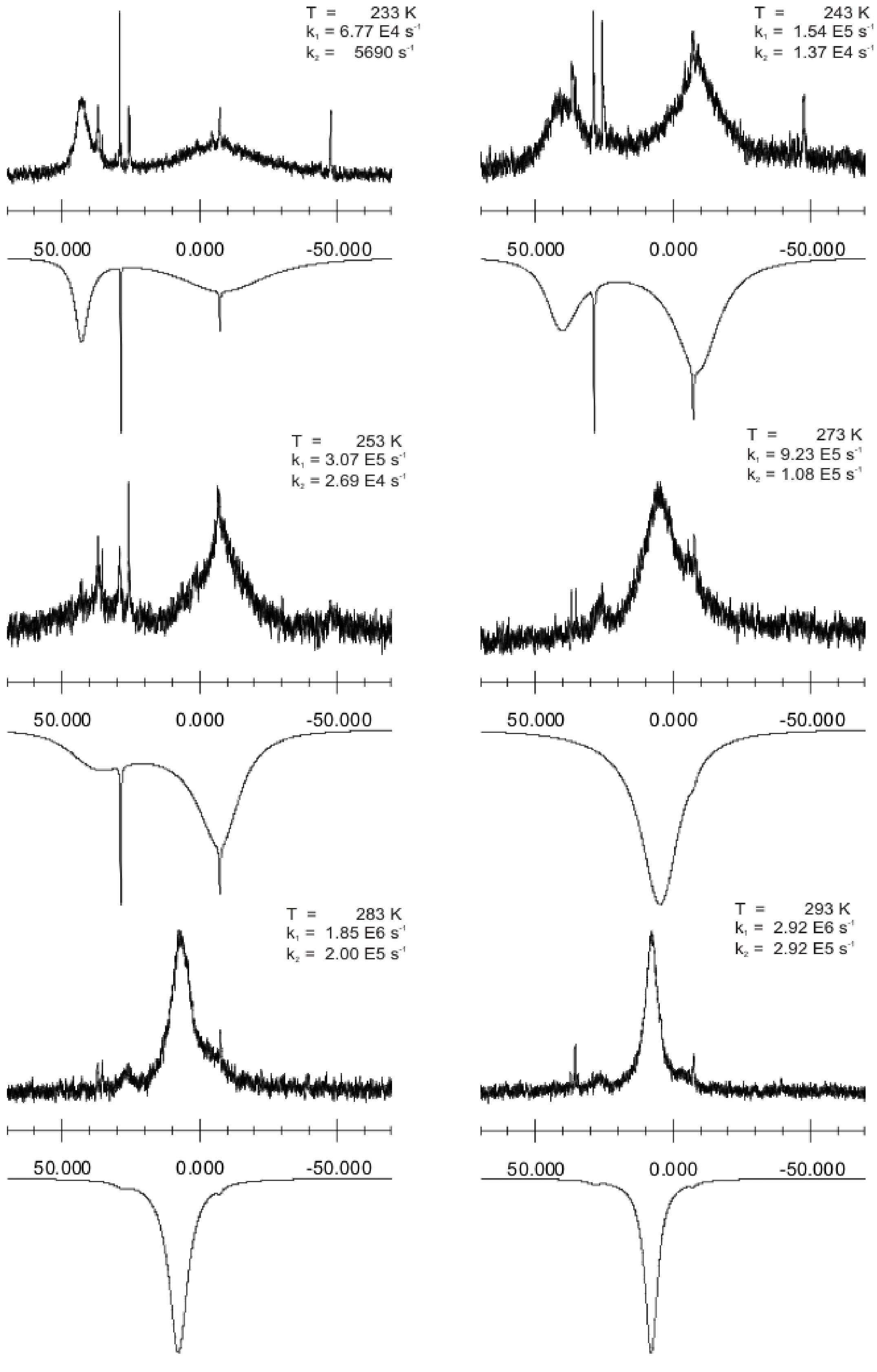

Supplementary Figure 24. Eyring and Arrhenius plots for **10** in MeOH:CD_2Cl_2 (2:9) Pd:PPh_3:py:CH_3SO_3H = 1:3.1:25. (sample 7).

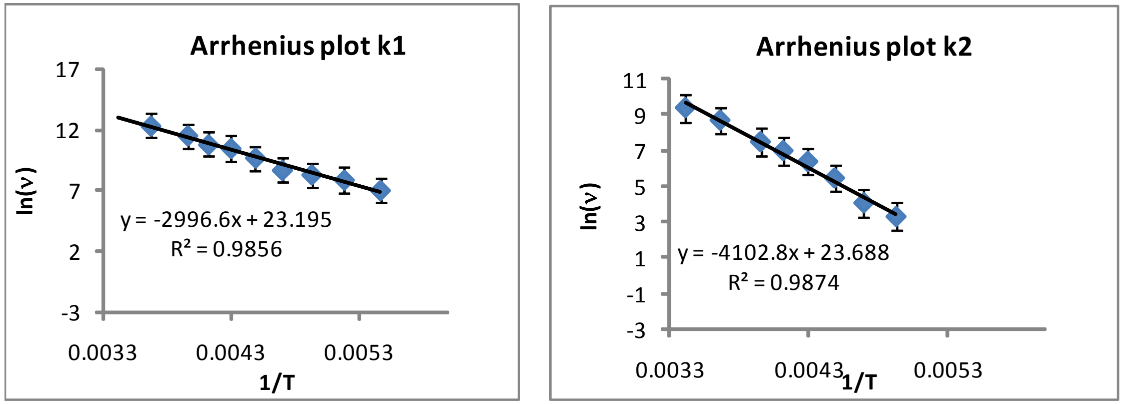

h	6.63E-34	J s^{-1}
kB	1.38E-23	J K^{-1}
R	8.314	J mol^{-1} K^{-1}

Eyring	**k1**	**k2**	
intercept	18.78	19.93	
gradEy	-2626	-3861	
ΔH	22	32	kJ mol^{-1}
ΔS	-41	-32	J K^{-1} mol^{-1}
Arrhenius			
Eact	25	34	kJ mol^{-1}
gradAhr	-2997	-4103	

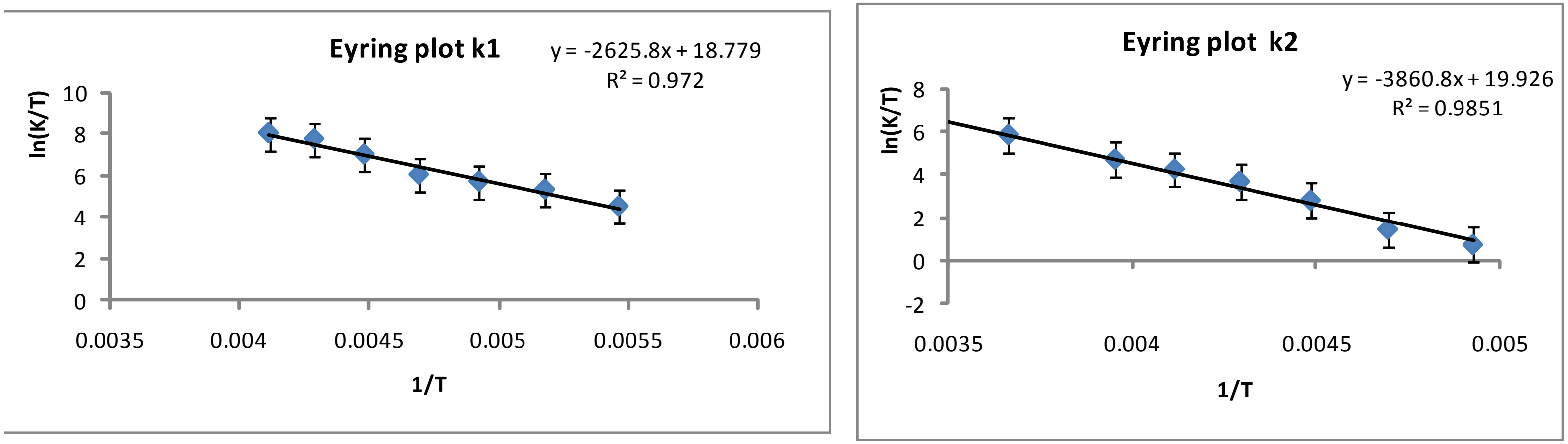

Supplementary Figure 25. Experimental and simulated variable temperature $^{31}P\{^1H\}$ NMR spectra of **10** in CD_2Cl_2 Pd:PPh_2py:CH_3SO_3H = 1:2.9:2. (sample 9). Impurities included to aid simulation, but not optimized.

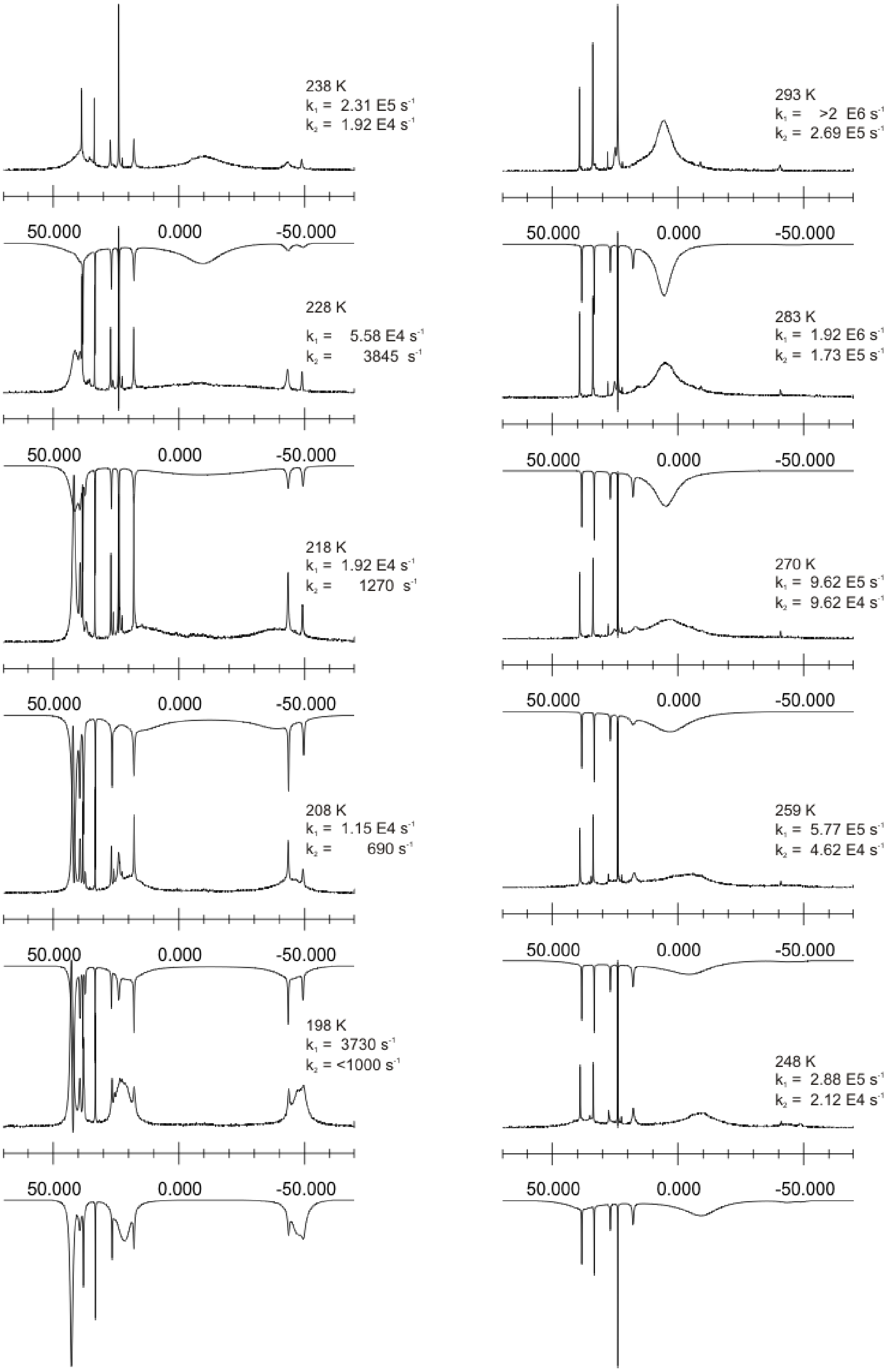

Supplementary Figure 26. Eyring and Arrhenius plots for **10** in CD_2Cl_2 Pd:PPh$_2$py:CH_3SO_3H = 1:2.9:2. (sample 9).

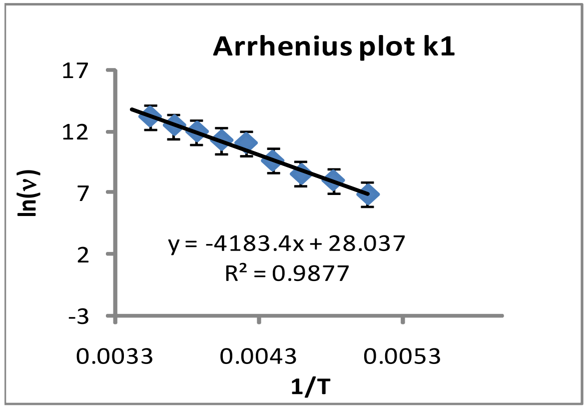

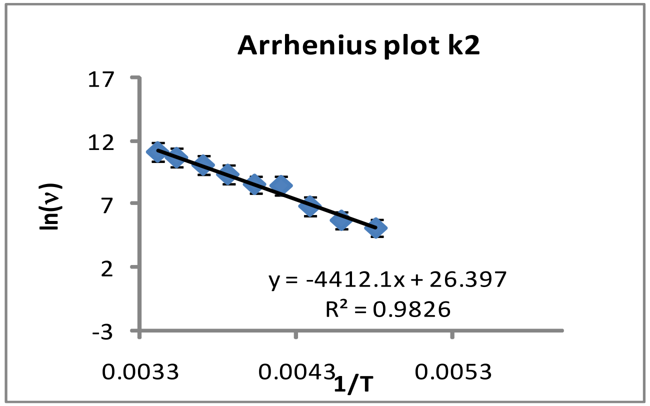

h	6.63E-34		J s^{-1}
kB	1.38E-23		J K^{-1}
R	8.314		J mol^{-1} K^{-1}
Eyring	**k1**	**k2**	
intercept	23.25	21.23	
gradEy	-4022	-4166	
ΔH	33	35	kJ mol^{-1}
ΔS	-4	-21	J K^{-1} mol^{-1}
Arrhenius			
Eact	35	37	kJ mol^{-1}
gradAhr	-4183	-4412	

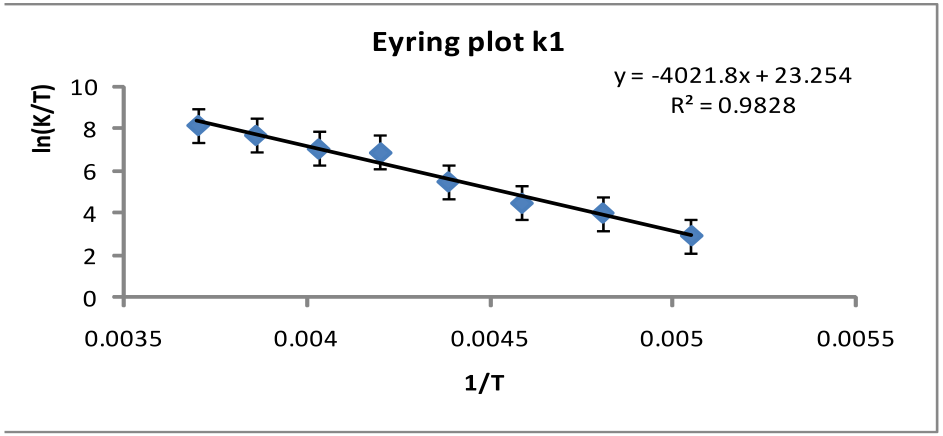

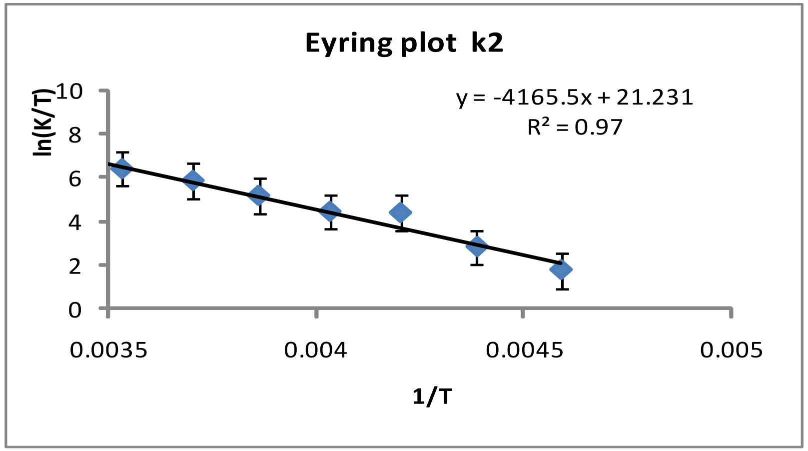

Supplementary Figure 27. Equilibrium saturation transfer difference measurements on impure **10**. The resonance of the chelating PPh_2py ligand at ca δ(P) -48 was irradiated throughout the recovery delay (3 s). Top set sample 5 - **10** in MeOH Pd:PPh_2py:CH_3SO_3H = 1:3.2:15; bottom set sample 6.- Pd:PPh_2py:CH_3SO_3H = 1:2.9:10.

Significant saturation transfer is seen to the other PPh_2py ligands in **10** but not to those of other complexes.

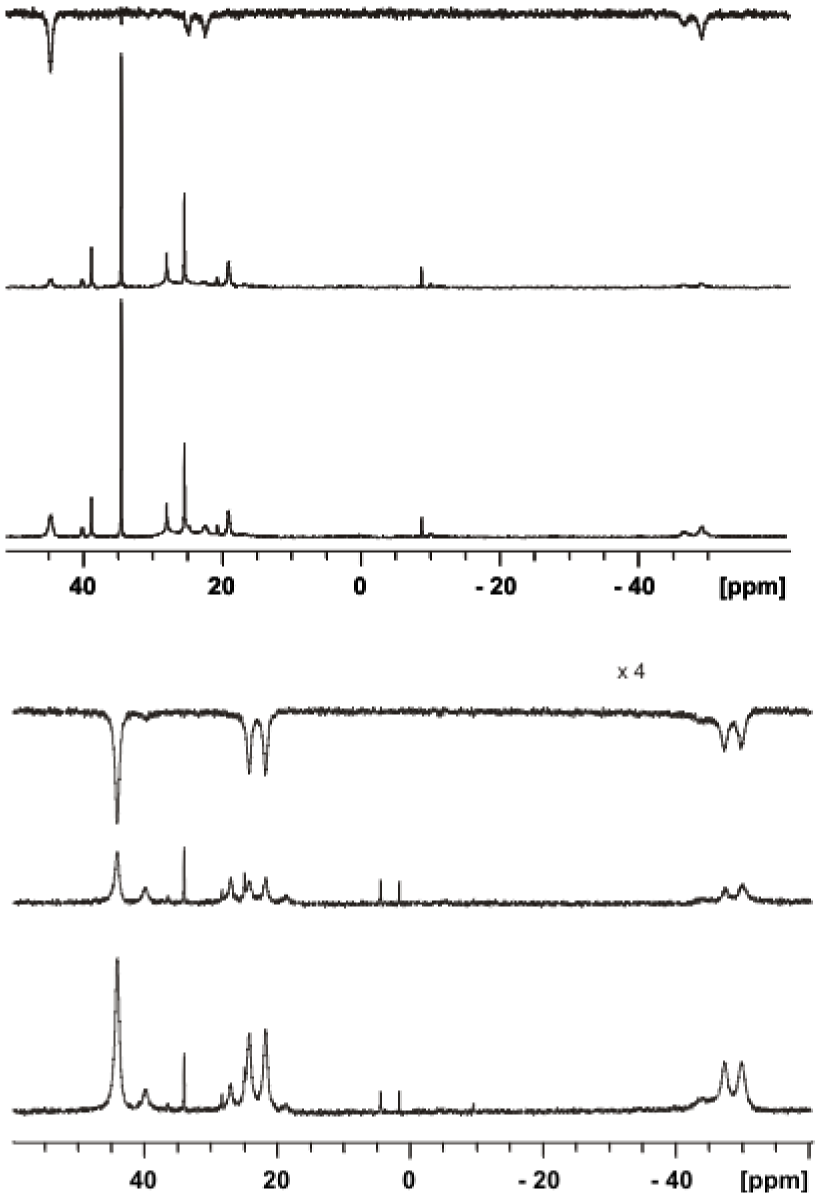

Supplementary Figure 28. Experimental and simulated variable temperature $^{31}P\{^1H\}$ NMR spectra of **3**(Cl) in CD_2Cl_2:MeOH (8:1). Note changes in ppm scale at 233, 253, 283 and 293 K

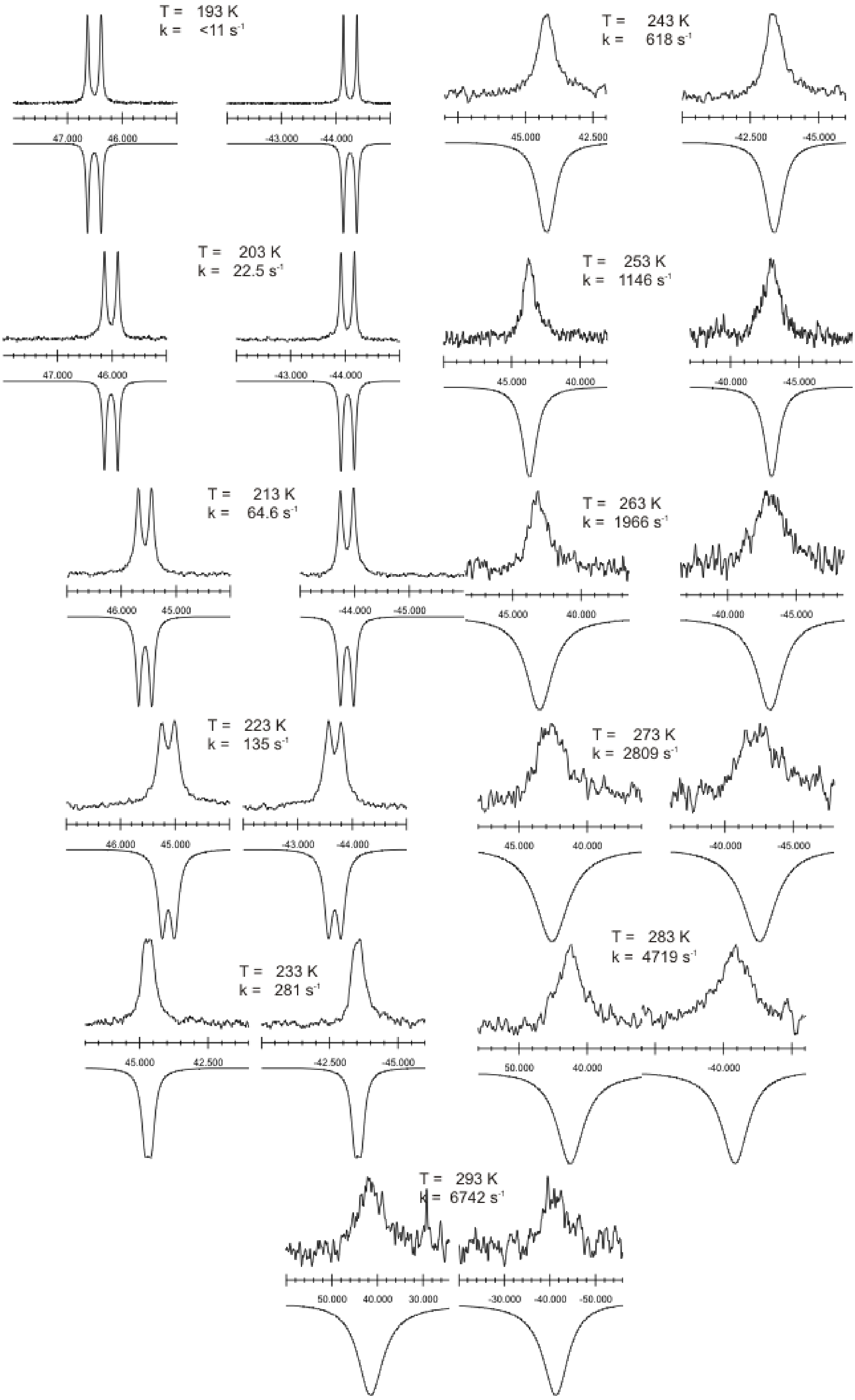

Supplementary Figure 29. Experimental and simulated variable temperature $^{31}P\{^1H\}$ NMR spectra of **3**[OTf] in CD_2Cl_2:MeOH (8:1). Note changes in ppm scale at 223, 263, and 283 K

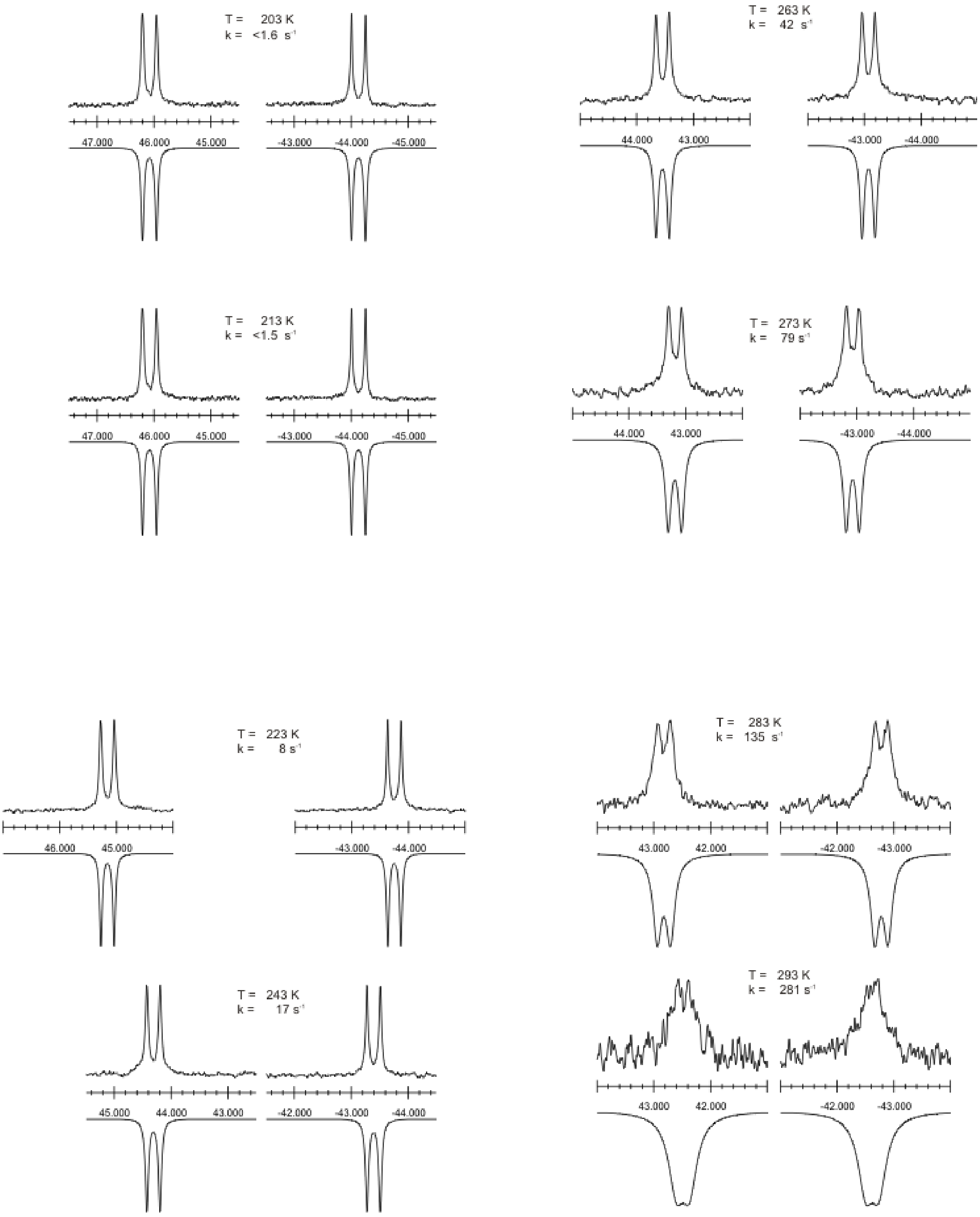

Supplementary Figure 30. Experimental and simulated variable temperature $^{31}P\{^{1}H\}$ NMR spectra of **3**(Cl) in CD_2Cl_2:MeOH (1:1). Note changes in ppm scale at 243, and 273 K

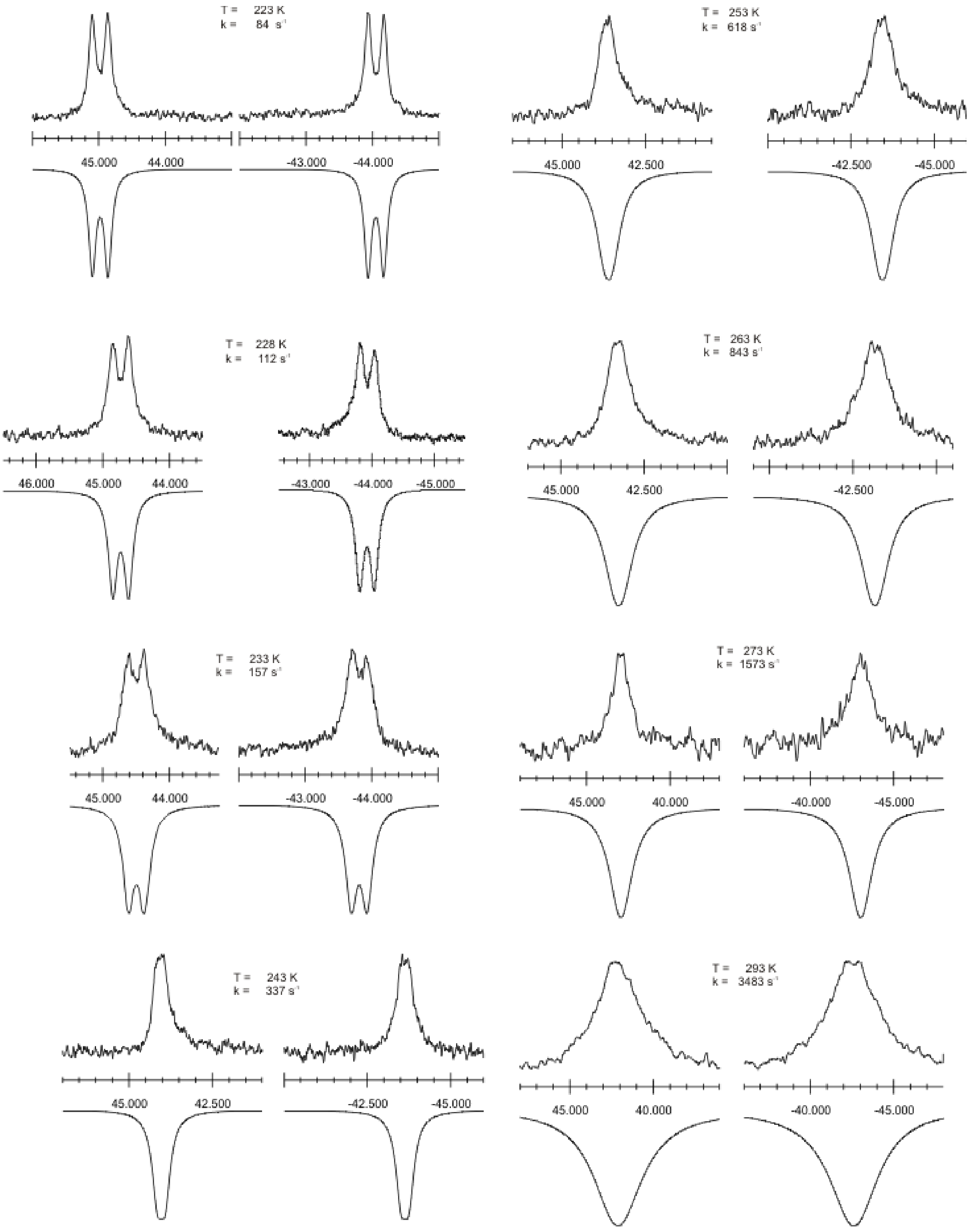

Supplementary Figure 31. Experimental and simulated variable temperature $^{31}P\{^1H\}$ NMR spectra of **3**[OTf]in CD_2Cl_2:MeOH (1:1).

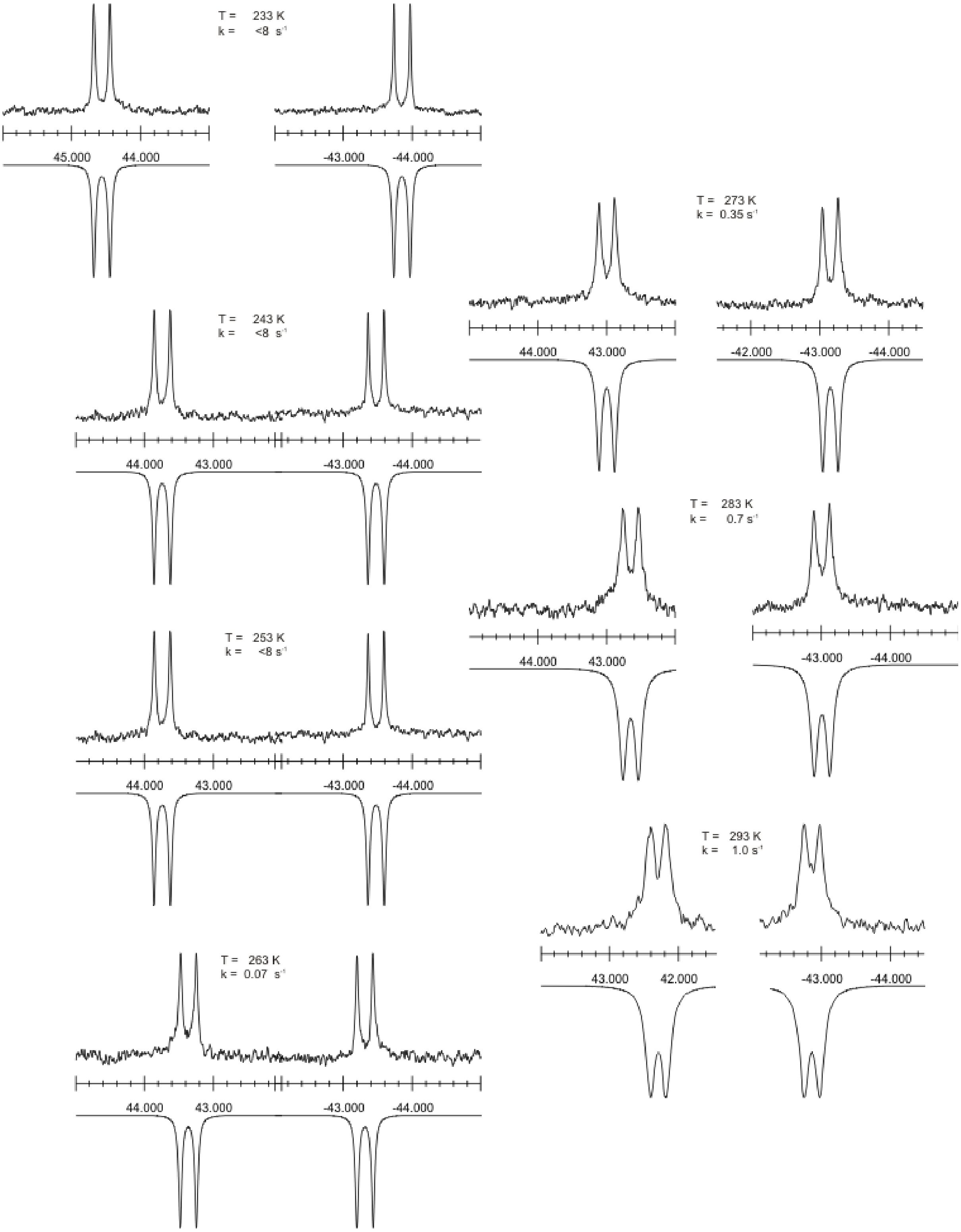

Supplementary Figure 32. Variable temperature $^{31}P\{^{1}H\}$ NMR spectra of **4**(Cl) in CD_2Cl_2:MeOH (1:1).

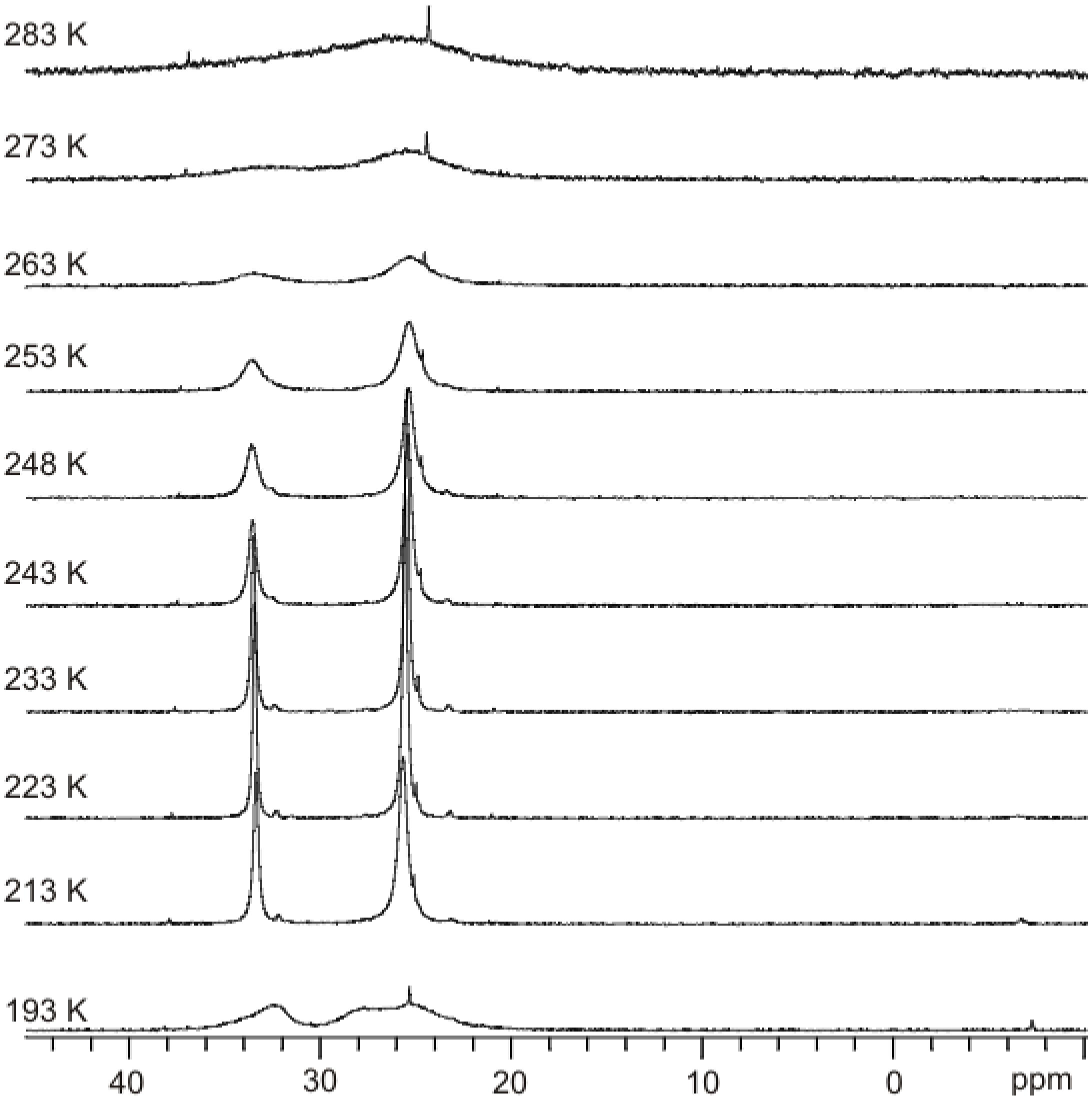

Supplementary Figure 33. $^{31}P\{^{1}H\}$ NMR spectra of **4** in CD_2Cl_2:MeOH (1:1); T = 193 K.

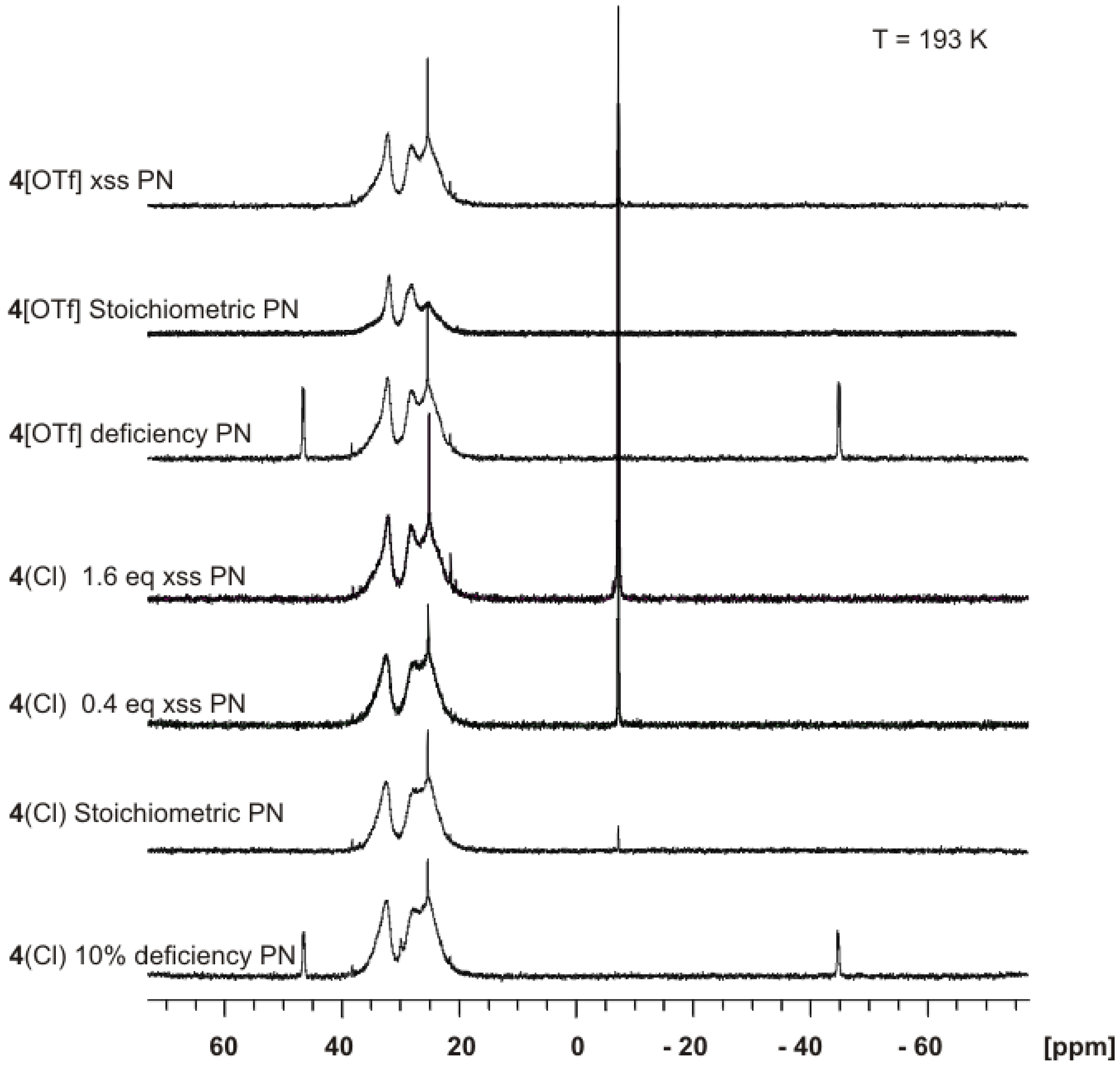

Supplementary Figure 34. $^{31}P\{^{1}H\}$ NMR spectra of **4** in CD_2Cl_2:MeOH (1:1); T = 213 K.

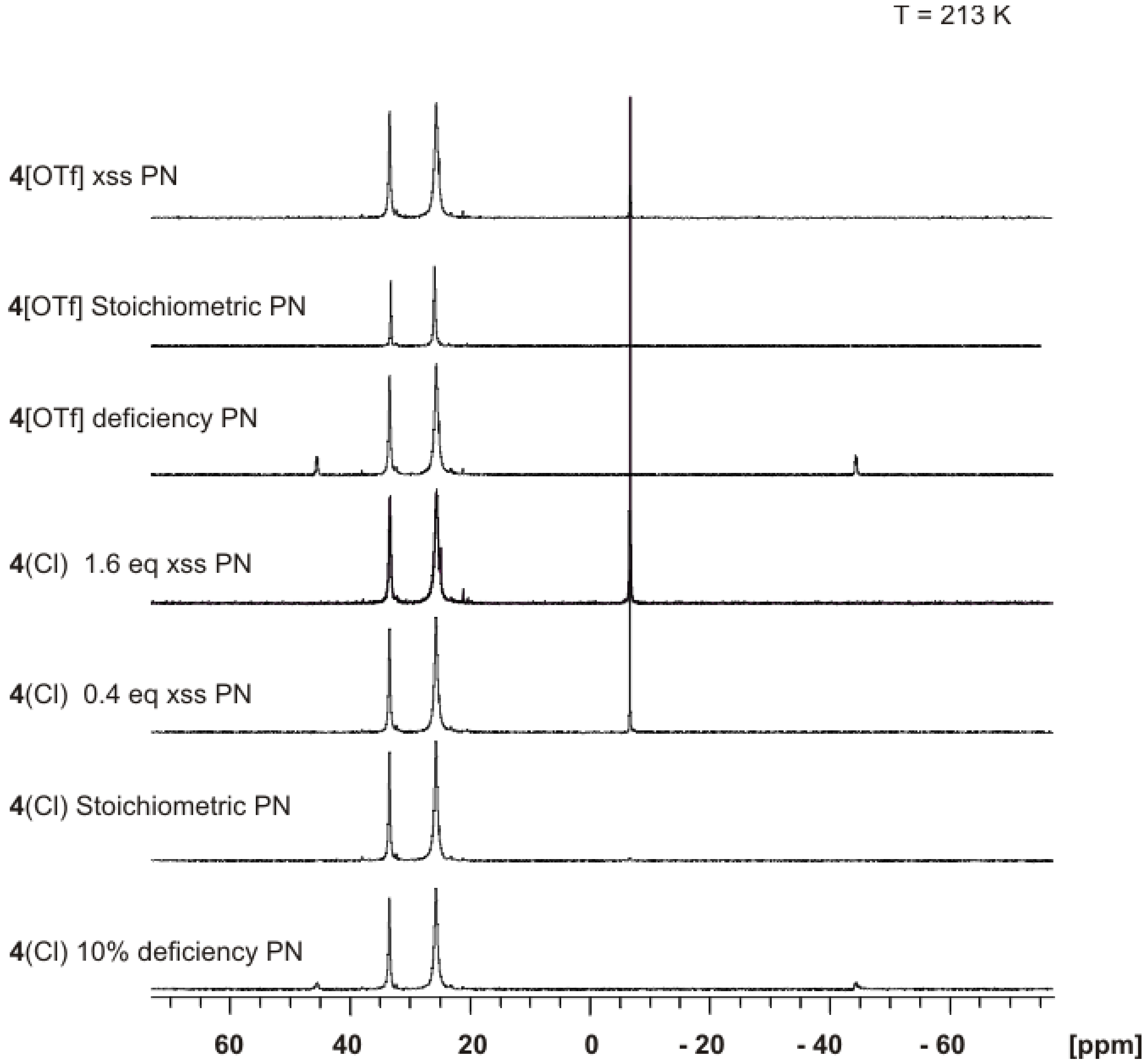

Supplementary Figure 35. $^{31}P\{^1H\}$ NMR spectra of **4** in CD_2Cl_2:MeOH (1:1); T = 233 K.

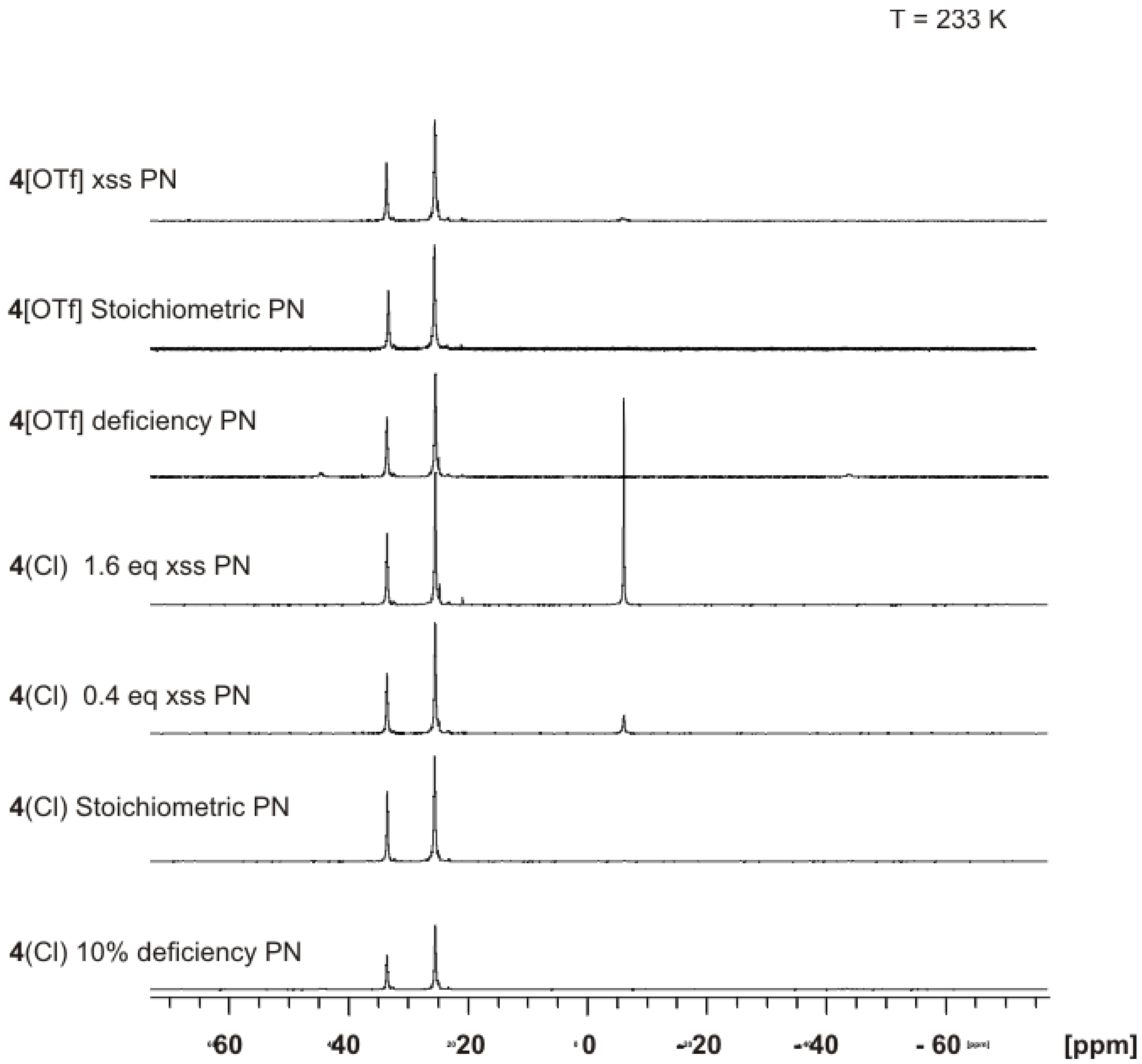

Supplementary Figure 36. $^{31}P\{^1H\}$ NMR spectra of **4** in CD_2Cl_2:MeOH (1:1); T = 243 K.

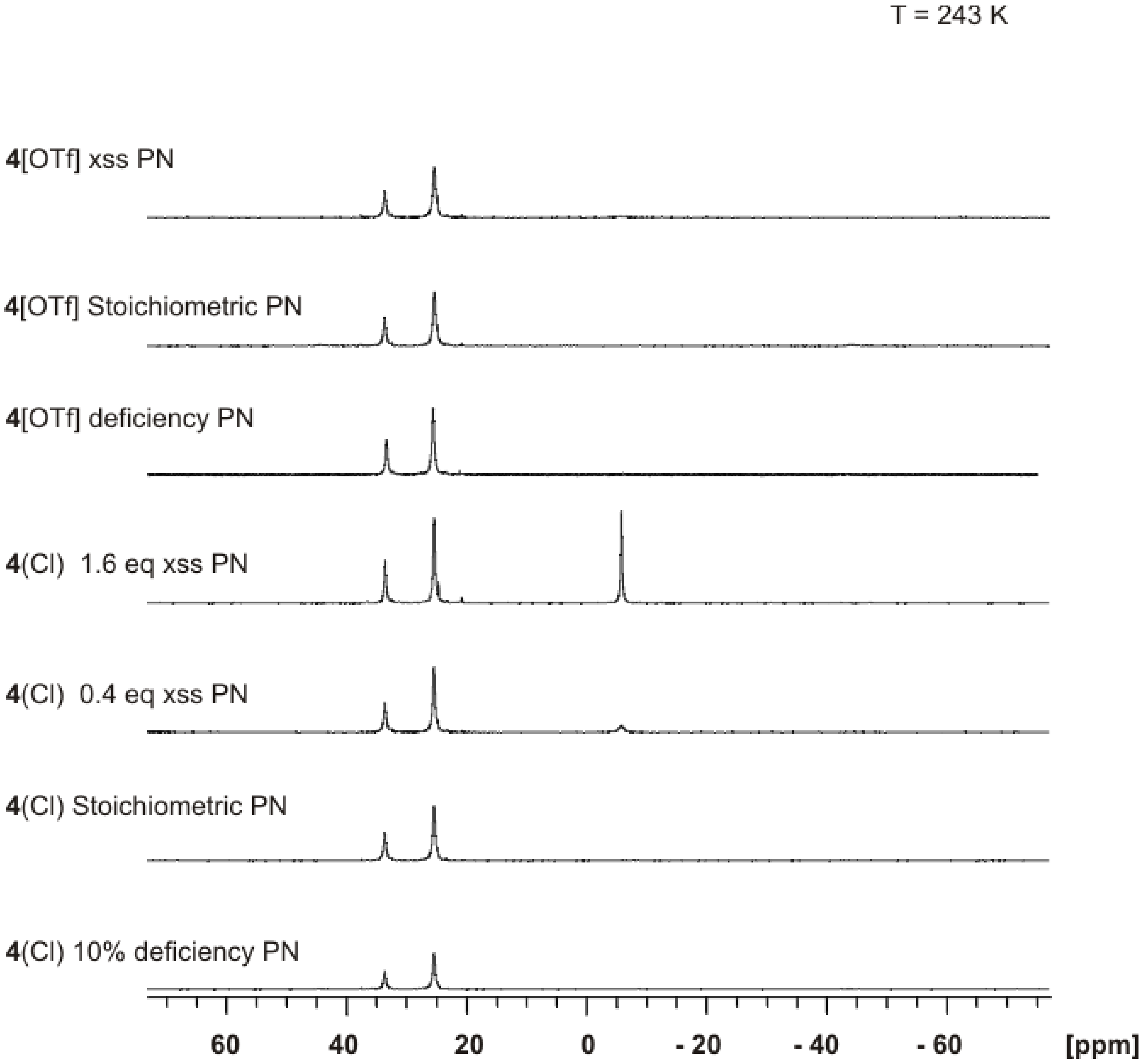

Supplementary Figure 37. $^{31}P\{^1H\}$ NMR spectra of **4** in CD_2Cl_2:MeOH (1:1); T = 263 K.

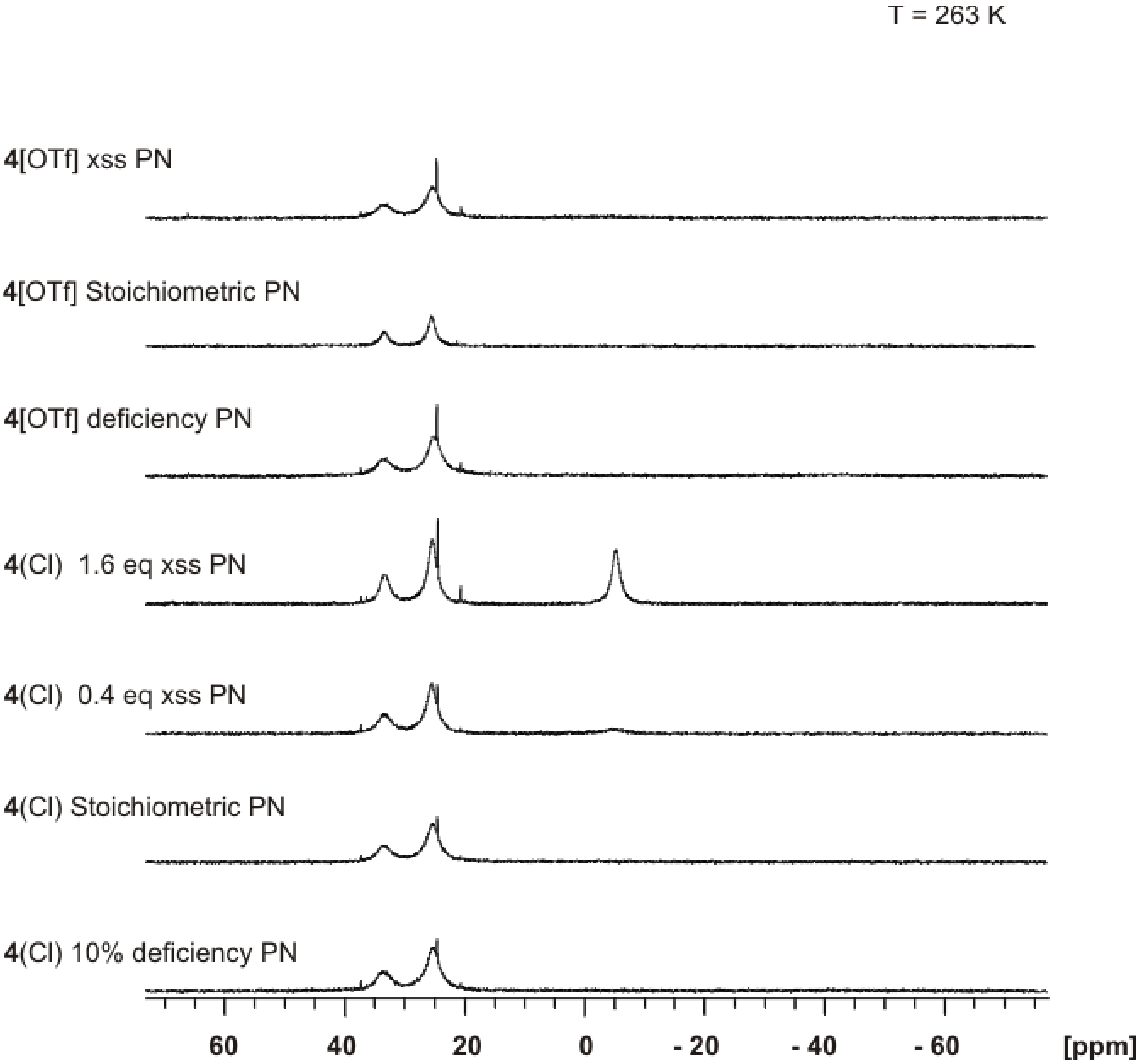

Supplementary Figure 38. $^{31}P\{^1H\}$ NMR spectra of **4** in CD_2Cl_2:MeOH (1:1); T = 273 K.

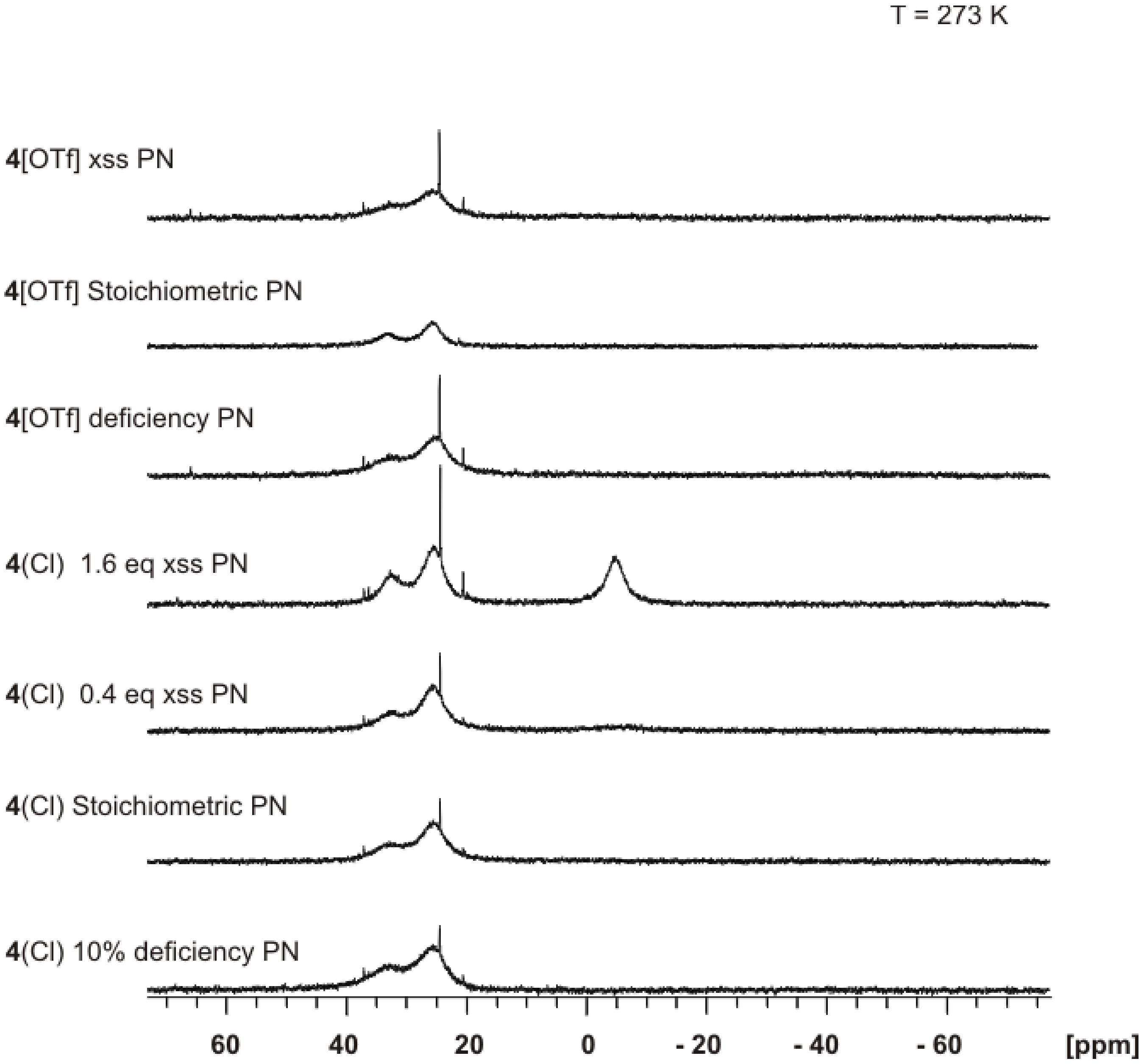

Supplementary Figure 39. $^{31}P\{^1H\}$ NMR spectra of **4** in CD_2Cl_2:MeOH (1:1); T = 283 K.

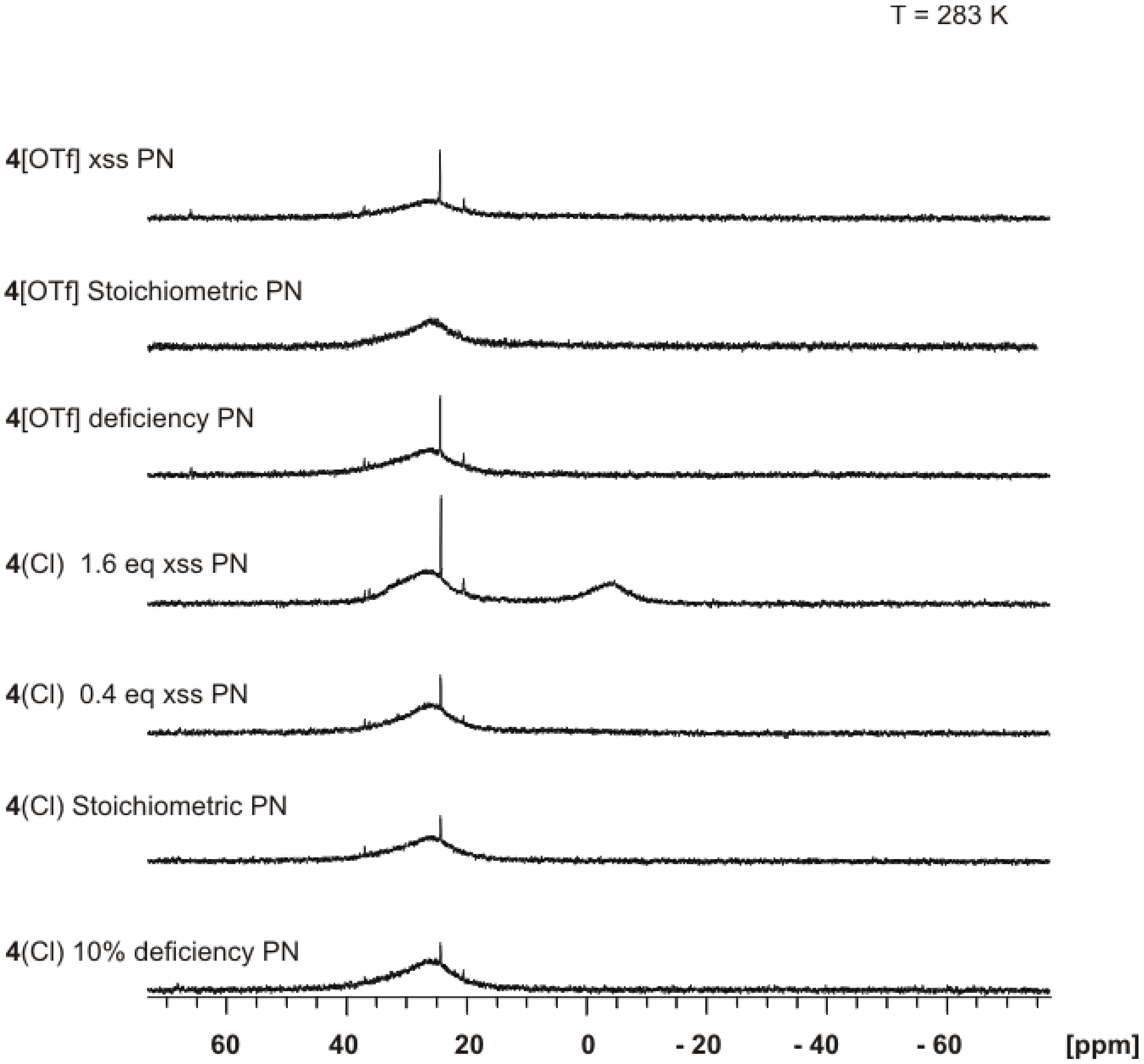

Supplementary Figure 40. $^{31}P\{^1H\}$ NMR spectra of **4** in CD_2Cl_2:MeOH (1:1); T = 293 K.

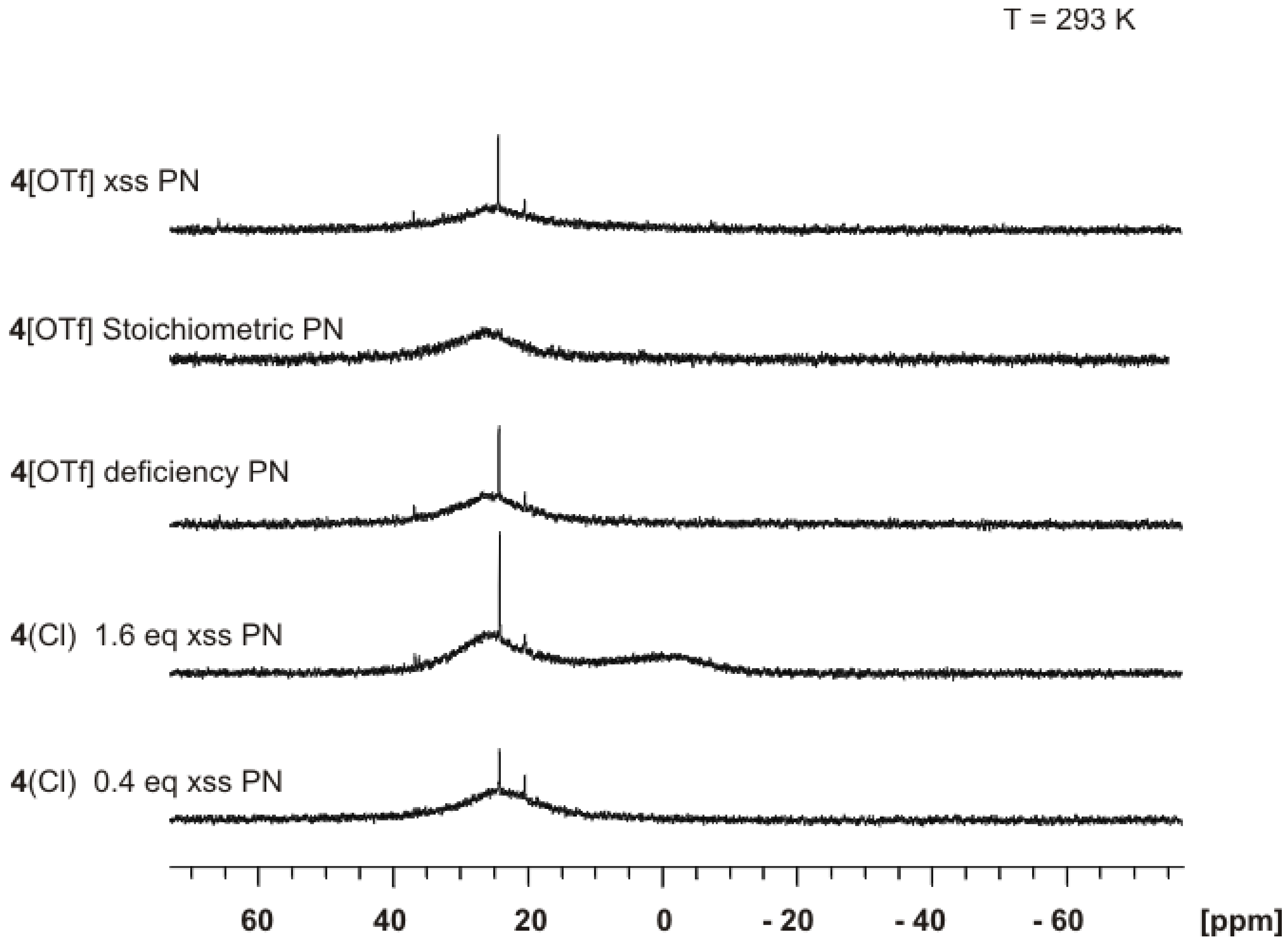

Supplementary Figure 41. Simulations of the variable temperature $^{31}P\{^1H\}$ NMR spectra of **4**(Cl)in CD_2Cl_2:MeOH (1:1), Pd:P = 1: 4.6, together with the Eyring and Arrhenius plots.

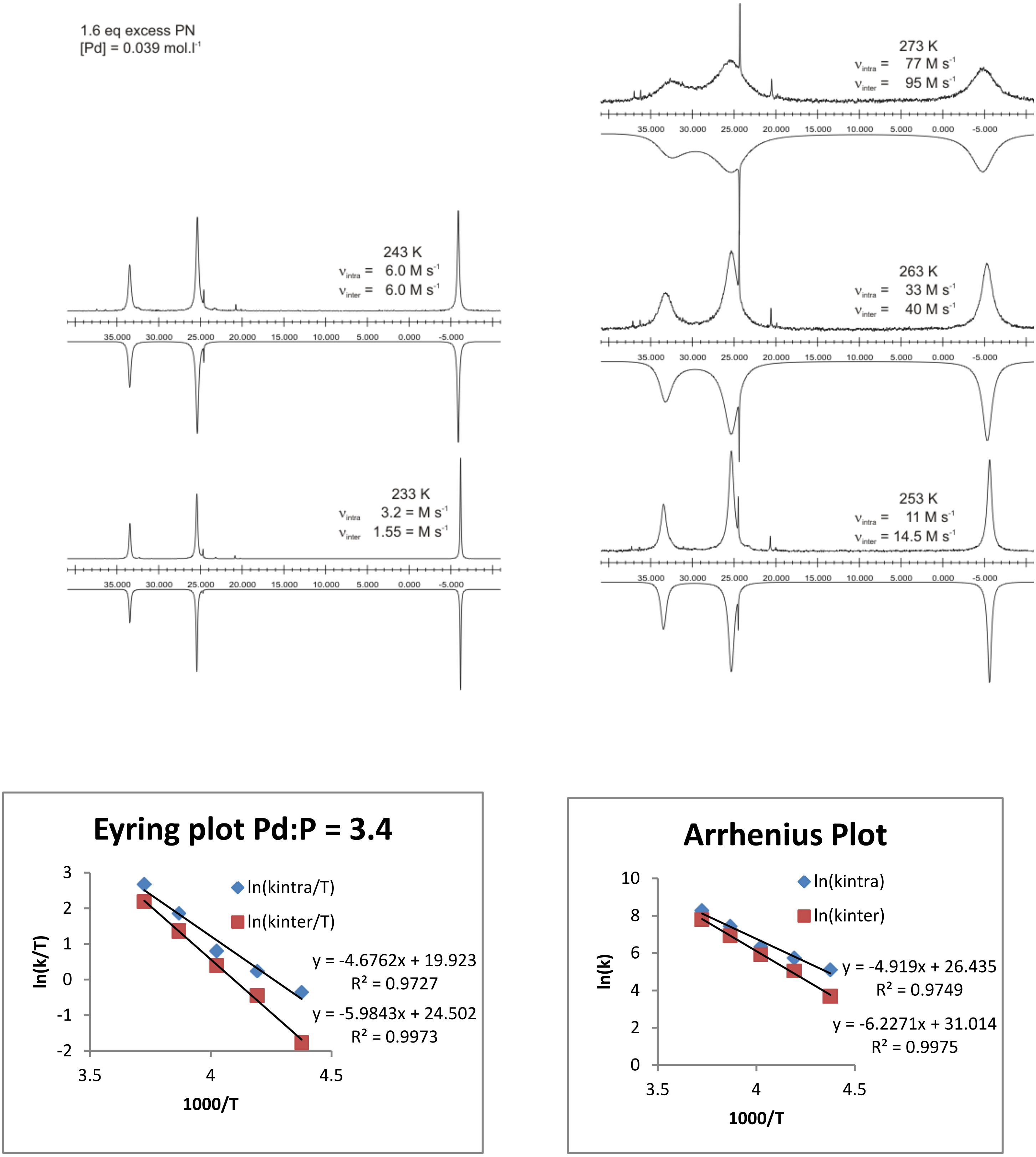

Supplementary Figure 42. Simulations of the variable temperature $^{31}P\{^1H\}$ NMR spectra of **4**(Cl)in CD_2Cl_2:MeOH (1:1), Pd:P = 1: 3.4, together with the Eyring and Arrhenius plots.

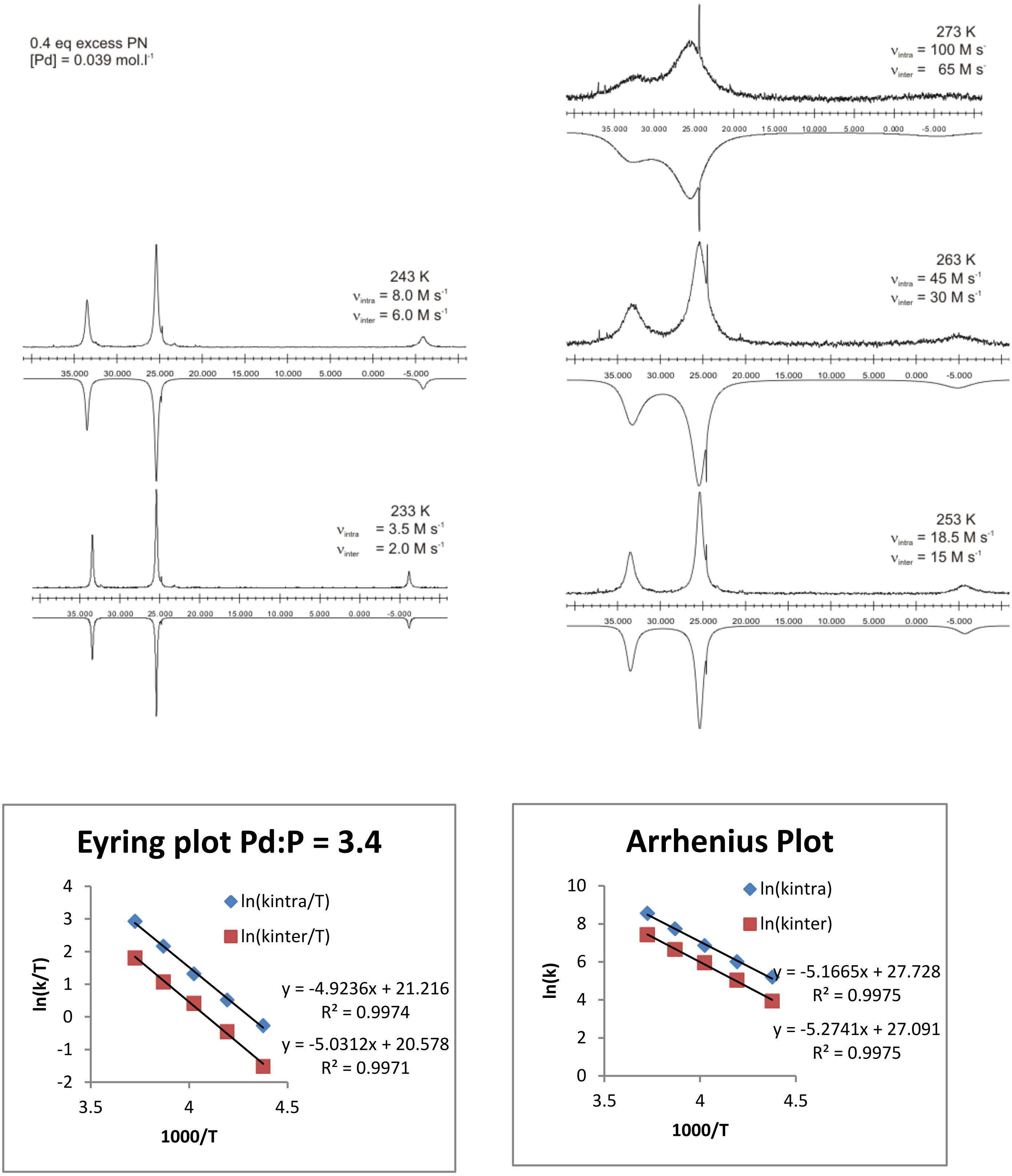

Supplementary Figure 43. Simulations of the variable temperature $^{31}P\{^1H\}$ NMR spectra of **4**(Cl)in CD_2Cl_2:MeOH (1:1), Pd:P = 1: 3.03, together with the Eyring and Arrhenius plots.

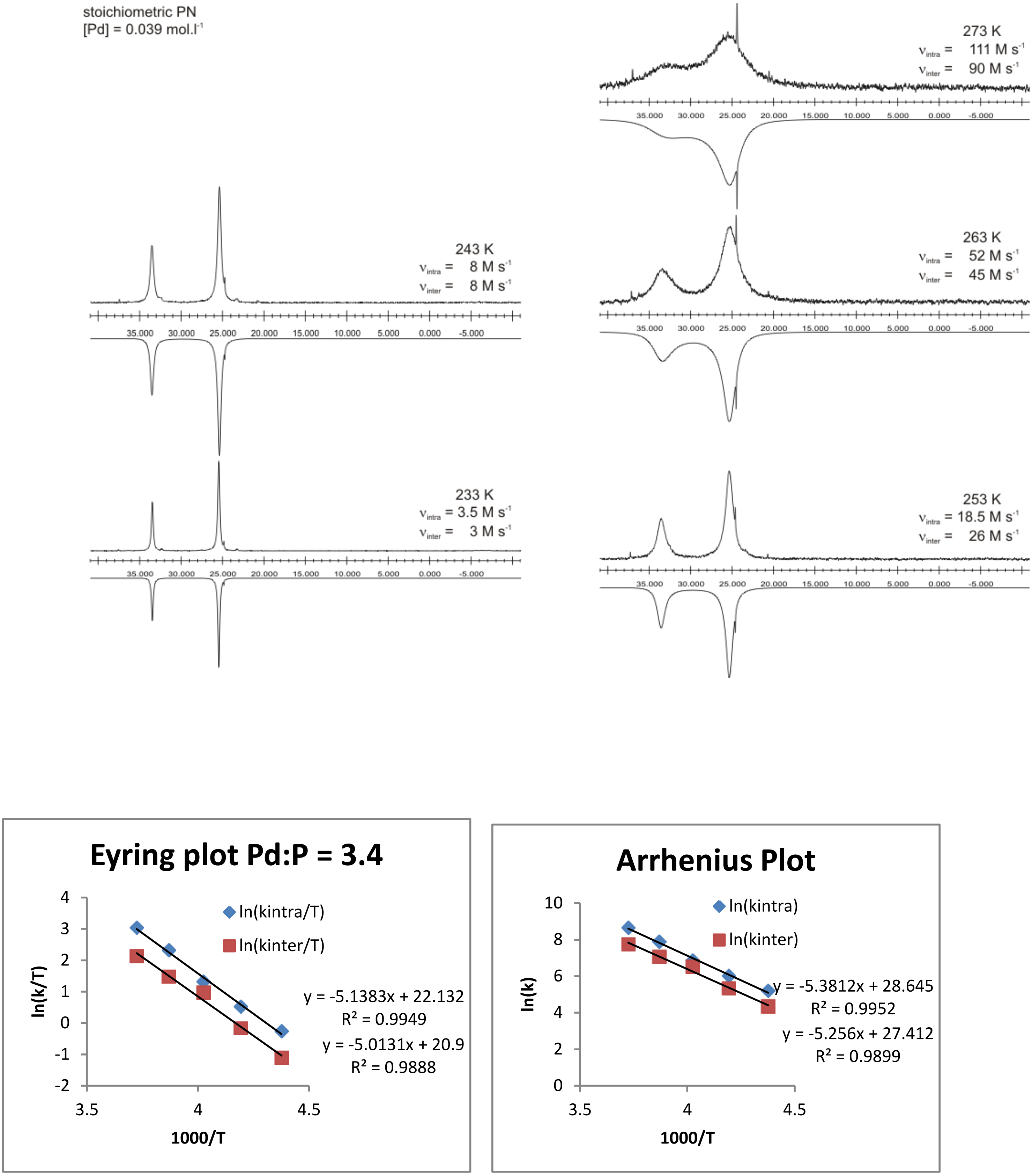

Supplementary Table 1 Kinetic and thermodynamic parameters for the dynamic processes in **4**(Cl) in CD_2Cl_2:MeOH (1:1).

P:Pd	**k_{intra}^{253}**[a] **/ s^{-1}**	**k_{inter}^{253}**[a] **/ s^{-1}**	**$\Delta S_{intra}^{\ddagger}$**[b] **/J mol^{-1} K^{-1}**	**$\Delta S_{inter}^{\ddagger}$**[b] **/J mol^{-1} K^{-1}**	**$\Delta H_{intra}^{\ddagger}$**[c] **/kJ mol^{-1}**	**$\Delta H_{inter}^{\ddagger}$**[c] **/kJ mol^{-1}**	**E_{act}^{intra}**[c] **/kJ mol^{-1}**	**E_{act}^{inter}**[c] **/kJ mol^{-1}**
3.03	950	670	-14	-24	43	42	45	44[c]
3.4	950	385	-21	-26	41	42	43	44[c]
4.6	565	370	-32	6[d]	41	50	41	52

Estimated errors: [a] ~ +/- 10%; [b] ~ +/- 10 J mol^{-1} K^{-1}; [c] $\Delta H^{\ddagger}$ and E_{act} ~ +/- 10%; [d] ~ +/- 20 J mol^{-1} K^{-1}.

X-Ray Crystallography.

Crystallographic data were recorded on a Bruker Smart Apex diffractometer using Mo$_{K\alpha}$-radiation (λ = 0.71073 Å) at T = 100 K. Structures were solved by Direct Methods and refined by full-matrix least squares against F^2 using all data (SHELXTL). All non-H atoms were refined anisotropically with the exception of disordered atoms. H-atoms were fixed in calculated positions at parent C and N atoms, respectively. The pyridyl-N atom in **1** is disordered over two pyridyl rings (N1 and C8). The C/N site occupancies for these two positions refined to 0.5/0.5 (equivalent xyz and adp constraints were applied). The CH_2Cl_2 molecule of **7**.CH_2Cl_2 is disordered over two positions. The disordered atoms were split on two positions and refined using similar distance and similar U restraints. Semi-empirical absorption corrections based upon equivalent and redundant reflections was applied to the data of **2b**.2CH_2Cl_2, **3**[BF_4] and **7**.CH_2Cl_2.

Supplementary Table 2 Crystal data for **2b**.2CH_2Cl_2, **2b'**$(MeSO_3)_2$.2CH_2Cl_2, **3**[BF_4], **4**(Cl).2H_2O and **7**.CH_2Cl_2

	2b.2CH_2Cl_2	**2b'**[$MeSO_3$]$_2$.2CH_2Cl_2	**3**[BF_4]	**4**(Cl).2H_2O	**7**.CH_2Cl_2
chem formula	$C_{36}H_{32}Cl_6N_2P_2Pd$	$C_{38}H_{40}Cl_6N_2O_6P_2PdS_2$	$C_{34}H_{28}BClF_4N_2P_2Pd$	$C_{51}H_{46}Cl_2N_3O_2P_3Pd$	$C_{41}H_{34}Cl_2N_2O_2P_2Pd$
fw	873.68	1065.88	755.18	1003.12	825.94
Crystal system	orthorhombic	Monoclinic	orthorhombic	Monoclinic	Triclinic
space group	*P*bca	*P*2_1/c	*P*bca	*P*2_1/n	*P*-1
a, Å	20.0004(10)	23.972(3)	17.704(2)	11.8634(16)	8.5706(9)
b, Å	7.9187(4)	10.0239(14)	18.156(2)	11.1293(15)	9.5072(10)
c, Å	22.9503(12)	18.270(3)	20.149(3)	35.892(5)	22.614(2)
α, deg	90	90	90	90	85.134(2)
β, deg	90	95.549(3)	90	94.840(2)	80.784(2)
γ, deg	90	90	90	90	78.237(2)
V, $Å^3$	3634.8(3)	4369.6(10)	6476.4(14)	4722.0(11)	1778.1(3)
Z	4	4	8	4	2
ρ_{calc}, g cm^{-1}	1.597	1.620	1.549	1.411	1.543
μ, mm^{-1}	1.070	1.008	0.805	0.651	0.802
Reflections (total)	21122	21748	38516	23535	9230
Reflections (unique)	4310	7680	7687	8280	6163
2θ(max), deg	56.5	50.0	56.5	50.0	50.0
R(*F*) [$I > 2\sigma(I)$]	0.023	0.063	0.024	0.065	0.065
wR2(F^2) (all data)	0.058	0.168	0.064	0.171	0.164

Crystal Structure of *trans*-[Pd(κ^1-Ph_2Ppy)$_2$$Cl_2$] (2b)

Yellow crystals, suitable for an X-ray crystal structure determination were obtained by layering a dichloromethane solution of a mixture of *cis* and *trans* isomers **2a/b** with diethyl ether. Visually, there appeared to be only one type of crystal present. The X-ray determination showed that these crystals contained the *trans* isomer **2b** (Figure 1). Selected bond lengths and angles are given in Table 3.

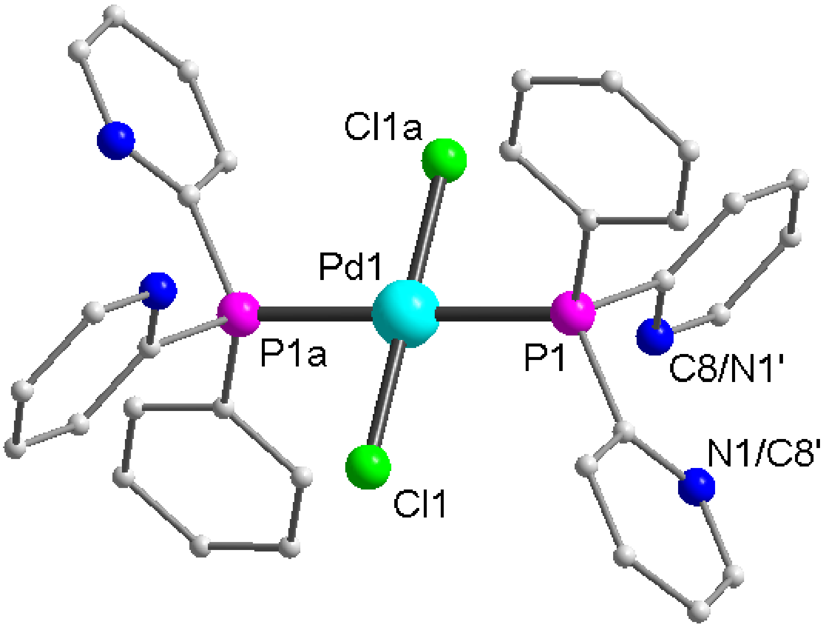

Supplementary Figure 44. Molecular structure of *trans*-[Pd(κ^1-Ph_2Ppy)$_2$$Cl_2$] **2b** with key atoms labelled and H atoms removed for clarity

The coordination about the palladium centre is square planar, with a centre of inversion at the palladium centre. Both Ph_2Ppy ligands are coordinated to palladium through phosphorus and are mutually *trans*, two terminal chloride ligands complete the coordination sphere (Figure 1). The position of nitrogen in one of the Ph_2Ppy ligands was split exactly between two phenyl rings so that each of the two rings were refined with C8 50% occupancy and N1 50% occupancy, no further refinement was attempted. The M-P bond lengths [2.3125(4) Å] are typical for Pd(II) complexes and are comparable to those reported for *trans*-[Pd(κ^1-Ph_2Ppy)$_2$(CO_2CH_3)Cl] [2.3315 Å] [1] and *trans*-[Pd(κ^1-Ph_2Ppy)$_2$($PhC{=}CH_2$)(CF_3CO_2)] [2.340(2) Å].[2] Bond angles between P1-Pd-P2 and Cl1-Pd-Cl2 are 180°, but P-Pd-Cl bond angles deviate slightly from the ideal 90°, Supplementary Table 2.

Supplementary Table 3. Selected bond lengths (Å) and angles (°) for *trans*-[Pd(κ^1-Ph_2Ppy)$_2$$Cl_2$] (**2b**)

Pd-P1	2.3125(4)	Pd-Cl1	2.2973(4)
Pd-P2	2.3125(4)	Pd-Cl2	2.2973(4)
P1-Pd-P1a	180.000	P1-Pd-Cl1	92.988(13)
Cl1-Pd-Cl1a	180.000	P1a-Pd-Cl1a	87.012(13)

Crystal structure of [Pd(κ^1-$Ph_2Ppy)_3Cl$](Cl) (**4**(Cl))

Crystals of **4** suitable for an X-ray crystal structure determination were obtained by slow removal of solvent from a saturated dichloromethane/MeOH solution *in vacuo*. Supplementary Figure 49 shows the molecular structure of **4** and selected bond lengths and angles are given in Supplementary Table 4. The complex is approximately square planar at the palladium centre with three purely monodentate pyridylphosphine ligands bonded through phosphorus and one chloride ligand completing the coordination sphere. The distortion from ideal geometry can be attributed to the steric bulk of the phosphine ligands. The Pd-P bond *trans* to the chloride is significantly shorter, 2.267(5) Å, as compared to the average Pd-P bond length *cis* to the Cl^- ligand, 2.3515(13) Å. The average Cl-Pd-P_{cis} and P_{cis}-Pd-P_{trans} bond angles were found to be 84.44(6)º and 96.65(6)º respectively, whereas the P_{cis}-Pd-P_{cis} bond angle was determined to be 161.50(6)º. Within the monocationic complex the pyridyl and phenyl groups are packed effectively via pi-stacking interactions and CH..N contacts, Supplementary Figure 45.

Supplementary Table 4. Selected bond lengths (Å) and angles (°) for [[Pd(κ^1-$Ph_2Ppy)_3Cl$](Cl).2H_2O (**4**(Cl).2H_2O).

Pd1-P1	2.3515(13)	Pd1-P3	2.2675(14)
Pd1-P2	2.3515(13)	Pd1-Cl1	2.3361(13)
P1-Pd1-P2	161.51(5)	P1-Pd1-Cl1	84.61(5)
P1-Pd1-P3	96.62(5)	P2-Pd1-Cl1	84.30(5)
P2-Pd1-P3	96.65(5)	P3-Pd1-Cl1	171.00(5)

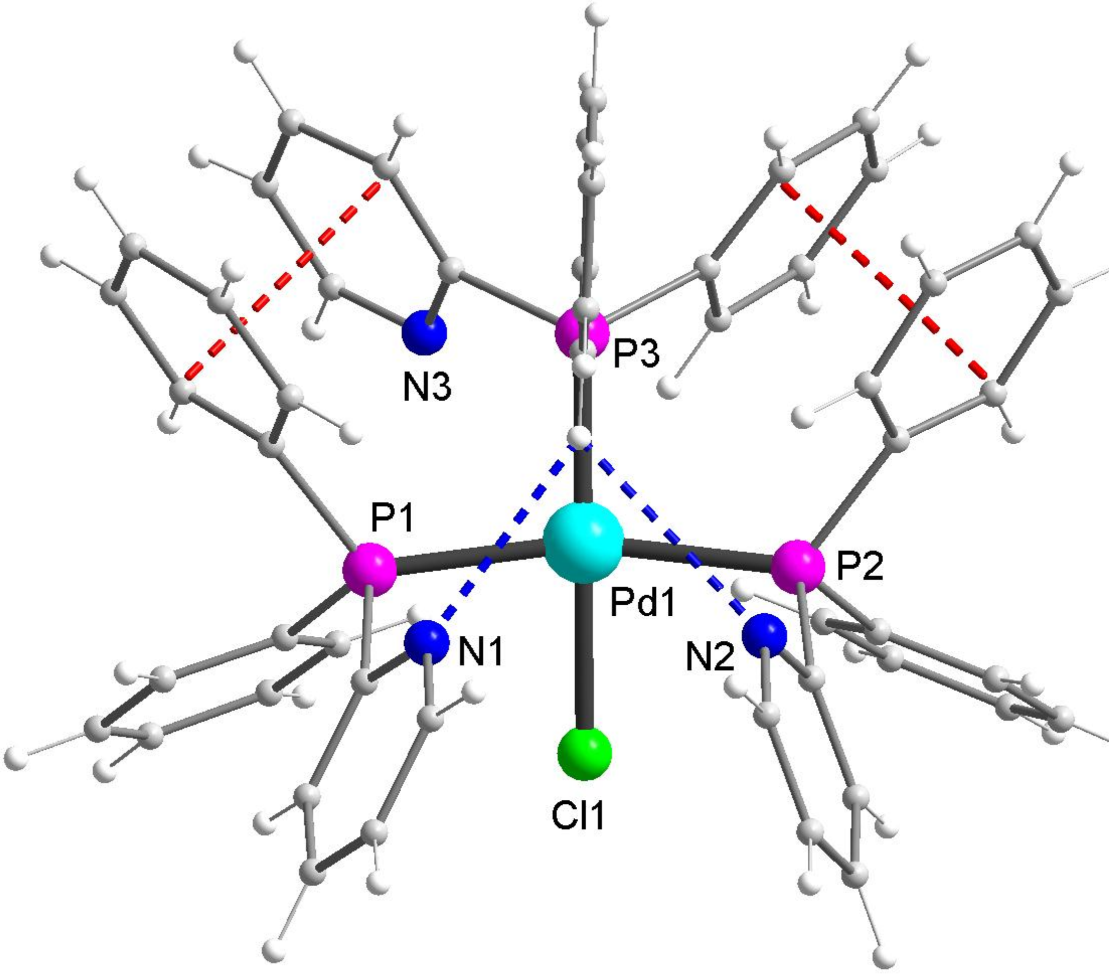

Supplementary Figure 45. Molecular structure of [Pd(κ^1-$Ph_2Ppy)_3Cl$](Cl).$2H_2O$ (**4**(Cl).$2H_2O$) highlighting the CH...N (blue) and π-stacking interactions (red) between the phosphine ligands.

.

References

1. A. Dervisi, P. G. Edwards, P. D. Newman, R. P. Tooze, S. J. Coles and M. B. Hursthouse, *J. Chem. Soc., Dalton Trans.*, 1999, 1113-1120.
2. A. Dervisi, P. G. Edwards, P. D. Newman and R. P. Tooze, *J. Chem. Soc., Dalton Trans.*, 2000, 523-528.
3. D. J. Darensbourg, J. B. Robertson, D. L. Larkins and J. H. Reibenspies, *Inorg. Chem.*, 1999, **38**, 2473-2481.